UNIVERSITY OF CALIFORNIA
RIVERSIDE

Polymer and Polymer/Virus Fibers Fabricated Through Near-Field Electrospinning for Whispering Gallery Mode Sensing and Biosensing

A Dissertation submitted in partial satisfaction
of the requirements for the degree of

Doctor of Philosophy

in

Materials Science and Engineering

by

Stephen T. Hsieh

September 2022

Dissertation Committee:
Dr. Elaine D. Haberer, Chairperson
Dr. Jianlin Liu
Dr. Ming Liu

The Dissertation of Stephen T. Hsieh is approved:

_____

_____

_____

Committee Chairperson

University of California, Riverside

Acknowledgments

A Ph.D. is shaped by the people you surround yourself with, and I have been truly fortunate to have met some fantastic and talented people. Firstly, I would like to thank my advisor Dr. Elaine D. Haberer for her mentorship and guidance. I have enjoyed my time in her lab in part due to the exciting research, I am grateful for the opportunity. I have appreciated the effort spent on developing solid fundamentals for research. I also want to thank Dr. Nosang V. Myung, whose support and collaboration enabled much of the work. I would like to thank Dr. Ming Liu and Dr. Jian Liu for acting as my committee members.

My senior mentor was Joseph E. Cheeney, whom I am grateful to. I learned a lot collaborating with him, both technical and general skills. Our discussion on whispering gallery modes and near field electrospinning was always extremely helpful through my time in the Haberer Lab.

I would like to thank Tam-Triet Ngo-Duc and Joshua Plank for being great colleagues. Spending time trying to answer their many technical questions kept me sharp. More importantly, they have been great friends. I am also grateful to Zaira Alibay, who entered the program around the same time. Knowing someone going through the same struggles made them easier to bear. I am thankful for Haberer group members past and present: Xi Ding, Alexander Graves, Jordyn Watkins, Xiangxi Yin, and Sebastian Wuste for their support and discussion.

I would also like to thank Central Facility for Advanced Microscopy and Microanalysis, Analytical Chemistry Instrumentation Facility and Microscopy and Imaging Core Facilities for their instrumentation and support. Their knowledge and support were always helpful in achieving my research goals.

To my close friends Kevin Lin, Gorby Shih and Tiffany Chou, your support has always been helpful and a relief in stressful times. To my family, especially my grandmother, parents, and sister, thank you for always being there to support me. I appreciated the advice even if I disagreed.

The text of this dissertation, in part, is a reprint of the material as it appears in Nanoscale (J. E. Cheeney, S. T. Hsieh, N. V. Myung, E. D. Haberer, *Nanoscale*. **12**, 9873–9883 (2020). The co-author J.E. Cheeney listed in that publication directed and supervised the research which forms the basis for this dissertation. They fabricated polymer fibers and conducted water-ethanol sensing experiments using methodology developed.

The text of this dissertation, in full, is a reprint of the material as it appears in Sensors and Actuators B: Chemical (. T. Hsieh, J. E. Cheeney, X. Ding, N. V Myung, E. D. Haberer, *Sensors Actuators B Chem.* **367**, 132062 (2022)).

ABSTRACT OF THE DISSERTATION

Polymer and Polymer/Virus Fibers Fabricated Through Near-Field Electrospinning for Whispering Gallery Mode Sensing and Biosensing

by

Stephen T. Hsieh

Doctor of Philosophy, Graduate Program in Materials Science and Engineering
University of California, Riverside, September 2022
Dr. Elaine D. Haberer, Chairperson

The detection of biomolecules, known as biosensing, has profoundly impacted biomedical diagnostics, disease monitoring/prevention, and food/water quality control. Despite the great strides in biosensing technology, there is still a drive to develop new biosensors that can improve current performance or solve emerging biosensing concerns. An emerging approach towards biosensing is using Whispering Gallery Mode (WGM) resonators. These devices are compact, highly sensitive, and require no additional fluorescent or radioactive tag, enabling real-time label-free biosensing. Polymer-based WGM cavities offer reduced material costs, simple processing strategies, and the potential for straightforward incorporation of bioreceptors in a single process step.

Concurrently, filamentous bacteriophages such as the M13 bacteriophage have attracted attention as alternative bioreceptors. The length of the virus is comprised of 2700 copies of the same protein, which can each function as a bioreceptor. Crucially, this

protein coat can be modified to display a wide range of specific binding motifs, creating a dense ordered arrangement of high-affinity peptides with the proper orientation for analyte binding.

In this work I focus on the fabrication of WGM polymer/M13 bacteriophage sensors/biosensing using the near-field electrospinning process (NFES). NFES is a variant of electrospinning combining the high-volume, rapid manufacturing of electrospinning with precise patterning to fabricate microfibers. An advantage of NFES is the polymer-based approach can produce fibers that incorporate dyes and biomolecules such as M13 viruses. These electrospun fibers were first utilized as refractive index sensor in water-ethanol mixtures. The successful demonstration of WGM sensing spurred the fabrication of polymer/M13 biosensor where the M13 functioned as a biorecognition element. The polymer/M13 fibers demonstrated specificity and sensitivity to the target analyte due to M13 on the fiber surface. Surface concentrations of M13 virus were increased during the NFES process by carefully tuning the M13 surface charge and electric field interactions. This work demonstrates the promise of NFES and electrospinning in fabricating WGM biosensors and highlights the use of M13 as a bioreceptor.

Table of Contents

List of Figures

Chapter 1 Introduction

1.1 Motivation

The detection and quantification of biomolecules plays a critical role in modern society. Fast and accurate assessment of analyte concentrations has become important to biomedical diagnostics, food and water quality control and even public health and safety guidelines. A class of analytical devices, biosensors, have risen to tackle this need, combining the sensitivity and specificity of a bio recognition element with a physical or chemical transducer, convert binding events into optical or electronic signal which in turn is processed into a concentration. As a result of their diverse applications, sensor design requirements vary greatly, but are generally evaluated with terms such as sensitivity, specificity and limits of detection (LoD)[1]. Additionally, other factors, such as robustness, manufacturability, and cost, are significant when evaluating sensor technology. Examples of biosensor range from low-cost, low-sensitivity sensors such as a pregnancy test to high-cost high sensitivity sensors such as surface plasmon sensors (SPR).

With the increasing demand and desire for better-performing sensors, new materials and device architecture are required. In recent years, label-free optical biosensors/transducers, which utilize electromagnetic fields to interact with the local environment and detect target analytes have gained steady interest. The optical biosensor exhibits high sensitivity, stability, and low noise conducive to high performance and does not require a label[2,3]. These optical devices can also operate in harsh environments as

they are not vulnerable to electromagnetic interference. This class of sensors includes SPR[4], photonic crystals[5], and whispering gallery modes (WGM). WGM-based biosensors have shown promise due to their compact size, high sensitivity[6], and fast response time (*i.e.*, tens of seconds)[7].

Research has also been done to investigate different bio-recognition elements. Common bio-recognition elements rely on biology, such as antibodies, aptamers[8], enzymes[9], viruses[10] Filamentous bacteriophages such as the M13 have attracted the interest of a handful of researchers as alternative affinity-based biorecognition element [11–15]. These viruses possess a large density of proteins that cover the length of the phage and can be modified with high affinity peptides to serve as biorecognition elements.

An ideal method to fabricate WGM M13 biosensors would be low-cost, scalable, and fast. Electrospinning is a technique to fabricate polymer fibers using an electric field that fits these criterion. It has shown promise in fabricating biosensors [16,17]. Electrospinning variants, such as near-field electrospinning (NFES), have also gained interest due to the deposition control provided [18].

In this dissertation, I investigate WGM / M13 biosensor fabricated using a near field electrospinning process (NFES). Polyvinyl alcohol (PVA) fibers studied as refractive index sensors/ simple transducers in ethanol-water solutions. The process was then modified to include the M13 bacteriophage and the resulting PVA/M13 fibers were used as WGM biosensors to detect streptavidin. Subsequent work focused on the NFES

process, using an electrostatic interaction between the M13 surface charge and electric field from NFES to increase the M13 surface concentration.

1.2 Whispering Gallery Mode (WGM)

1.2.1 Whispering Gallery Mode Theory and Fabrication

Whispering Gallery modes are optical resonances formed by light recirculating along the periphery of a cavity. Light is confined by total internal reflection and recirculates along around the cavity periphery (Figure 1-1a). At specific wavelengths, the recirculating light will only constructively interfere, forming a standing wave. The path traveled and the specific wavelengths are known as the WGM resonance. It typically forms in spherical or circular cavities (Figure 1-1b). Owning to the evanescent wave that arises from the light traveling by total internal reflection, a portion of the WGM resonance extends outside the cavity. Resonance is influenced by the refractive index inside and outside the cavity. As a result, the WGM resonance wavelength depends on the resonator geometry and refractive index of the resonator and the host medium[2].

The simplest description for WGM resonance is:

$$l\lambda = \pi D n_{res} \tag{1-1}$$

where l is a positive integer indicating the azimuthal mode number, λ is the wavelength, D is the resonator diameter, and n_{res} is the refractive index of the resonator. This model is sometimes referred to as the ray-optics model as it assumes the light recirculating along the resonance periphery in a single plane[19] (Figure 1-1a). An approximation that the path length is equivalent to the resonator circumference[19]. A drawback of this model is that it fails to account for both the refractive index of the environment and polarization of

the light, transverse magnetic (TM) or transverse electronic (TE). Additional issues may occur at low *l* as the path length is no longer equivalent to $\pi D n_{res.}$

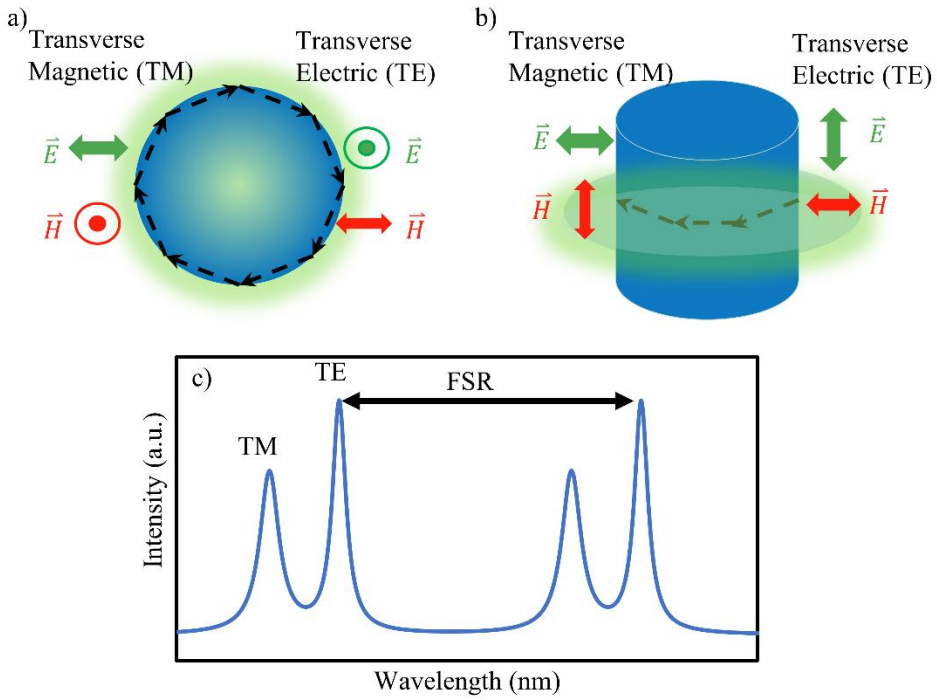

Figure 1-1: a) Schematic representation of WGM assuming the reflections line in a single plane b) WGM resonance and associated polarization for a cylindrical resonator c) Model spectrum from an active WGM resonator

A complete description of the WGM resonance comes from solving maxwell equations for a dielectric sphere, yielding the boundary conditions[20]:

$$\frac{[n_{host}kRh_l(n_{host}kR)]'}{h_l(n_{host}kR)} = N\frac{[n_{res}kRj_l(n_{res}kR)]'}{j_l(n_{res}kR)} \qquad (1\text{-}2)$$

where n_{res} and n_{host} are the refractive index of the resonator and the host medium, $k = 2\pi/\lambda$ where λ is the resonance wavelength. j_l and h_l are the spherical Bessel and Hankel functions of the first kind. N = 1 for TE modes or $(n_{host}/n_{res})^2$ forTM. R is the resonator radius. For a given R, multiple solutions indexed by three mode numbers[21], the radial

(*s*), azimuthal (*l*) and polar (*m*) where *m = -l, -l +1,…, l*. However, this equation has no exact analytical solution, and is solved numerically or using analytical approximations. Such approaches have been calculated using Airy approximations for spheres [22] and cylinders[23]. The approximation for the first radial mode is presented below:

$$\lambda \cong \pi n_{res} D \left[\nu + \frac{\alpha_s \nu^{\frac{1}{3}}}{2^{\frac{1}{3}}} - \frac{P}{(m^2-1)^{\frac{1}{2}}} + \frac{3}{10} \frac{\alpha_s{}^2}{2^{\frac{2}{3}} \nu^{\frac{1}{3}}} - \frac{P\left(m^2 - \frac{2P^2}{3}\right)}{(m^2-1)^{\frac{3}{2}}} \frac{\alpha_s}{2^{\frac{1}{3}} \nu^{\frac{2}{3}}} \right]^{-1} \quad (1\text{-}3)$$

where *D* is the optically measured fiber diameter, *v* is the angular mode number (*l*) plus 0.5, α_s are the roots of the Airy function, and n_{res} is the refractive index of the resonator. The term *m* is the ratio of the refractive index of the resonator to the refractive index of the surrounding medium (n_{res}/n_{host}). P is 1/*m* for TM modes and *m* for TE modes.

As the WGM requirements only require recirculating light undergoing total internal reflection, the material, and geometries for WGM are flexible. Typically the cavity is circular and compact, 10-100s μm in diameter, with geometries such as spheres[24], disks[25], microbubbles[26] and fibers[27] able to support WGM. Material-wise, the refractive index of the resonator only needs to be higher than the outside environment enabling WGM resonators fabricated out of a variety of materials such as silica[28] and polymers[29].

1.2.2 Whispering Gallery Mode Sensors and Biosensors

For most WGM sensors, the evanescent wave formed during resonance is utilized to sense the local environment. Because the wave decays as a Hankel function, in most applications, the wave diminishes close to the surface, interacting only near the resonator

surface. How well confined the light is within the resonator is defined as the quality (Q) factor. The evanescent wave allows the resonator to sample the local environment near the surface and in the case of biosensing, sense binding events to bioreceptors on the surface[30,31]. Typically sensing occurs by detecting changes in the resonance wavelength, but other strategies such as mode broadening[20] and mode splitting[32] have been used. These strategies allow for label-free optical biosensors with compact size, high sensitivity[6], and fast response time (*i.e.*, tens of seconds)[7].

For this work, the focus will be on WGM resonance wavelength shifts as sensors and transducers. Sensitivity (S) can be defined as $\frac{\Delta\lambda}{[C]}$ where $\Delta\lambda$ is the wavelength shift and [C] is the concentration of the analyte. The sensitivity of a WGM is governed by the interaction of evanescent wave with the analyte, with a larger evanescent wave providing a stronger response and thus sensitivity[20]. A measure of how well the electromagnetic field is contained within a resonator can be defined as the quality (Q) factor[33]:

$$Q = \omega \frac{E_{stored}}{P_{diss}} = \frac{\lambda_{Resonance}}{\lambda_{FWHM}} \quad (1\text{-}4)$$

It is well known that the Q-factor decreases with resonator size, indicating an increased evanescent wave. As a result, resonators with smaller radii have larger sensitivity[34]. Another key sensing parameter is the upper and lower limit of detection. For ideal bulk refractive sensing, the lower limit of detection can be defined as $LoD_{lower} = 3\sigma/S$ where σ is the noise of the peak position. Correspondingly, the upper limit of detection is defined as $LoD_{upper} = FSR/S$ where FSR is the free spectral range, or range of wavelengths with no WGM resonances (Figure 1-1c). As the Q-factor increase (i.e.,

resonator size increases), the sharper peaks decrease the σ. For lower LoD, this creates a tradeoff where low Q (smaller resonators) have higher sensitivity and larger noise while high Q (larger resonators) have lower sensitivity but lower noise. Reynolds analyzed the theoretical optimum and found that in general the trend favored larger resonators for lower limits of detection[34]. The lowest limit of detection for WGM sensor reported has been down to single molecule using microtoroids 80-100 μm in diameter with Q-factors ~ 1 x10^5 – 5 x 10^6 [35].

However, higher Q-factor or larger resonators do have drawbacks. They require the equipment to detect the minute shifts in the resonance wavelength. A common strategy is to use a tunable laser traveling through a taped fiber optic cable[36]. The laser is evanescently coupled to the WGM resonance as the laser sweeps through different output frequencies. One disadvantage of this coupled approach is the positioning of the fiber optic and resonator must be controlled with nanometer precision. Larger resonators also more readily support higher order mode resonances, such as higher order radial. These additional modes can complicate the spectrum making it difficult to determine resonance shifts.

In contrast, low Q-factor or smaller resonators do not suffer from these issues. While they can be excited using evanescent coupling[37], far-field coupling becomes possible. Free space optics can focus light onto the resonator and excite an active fluorescence source on or within the cavity. The resulting fluorescence is trapped within the cavity and forms the WGM resonance. Riesen[37] excited 15 μm polystyrene active spheres and demonstrated that while tapered fibers had an increase in Q-factor, free space

excitation was more able to detect peak splitting due to asphericity. Meanwhile Himmelhaus[29] explored how low-Q factors and smaller-sized resonators operate as a biosensor to Bovine serum albumin (BSA). The advantage of this far field approach is there is no need for as precise coupling, reducing the effects of vibrational noise. Additionally, there is no concern of the taped fiber evanescently coupling to the environment, reducing interference from the environment.

1.3 M13 Bacteriophage based bioreceptor

Another critical part of the biosensor is the biorecognition element. Commonly utilized biorecognition elements rely on the interactions developed from biology rather than synthetic chemicals. These include antibodies, aptamers[8], enzymes[9], viruses[10]. These biorecognition elements also called bioreceptors, provide specificity or selectivity to the target and influence sensitivity. Selectivity is defined as the ability of the bioreceptor to bind to the target in a complex medium[1]. The bioreceptor also influences sensitivity by increasing the amount of bound target to the transducer, thereby increasing the transducer response.

They also impact other device properties. Poor chemical or thermal robustness of the biorecognition element, for example antibodies, translates to poor robustness of the sensor overall. Additionally, the biorecognition elements are often unique to their target, requiring new chemistry or methodologies for each new bioreceptor-analyte pairing. For this reason, the M13 and the related fd bacteriophage have been of interest as an alternative affinity-based bio-recognition element[11–15,38]. It possesses programmable

functionality, high density of modifiable coat proteins, robust nature, simple amplification process and thermal/pH robustness[39]. These viruses have a large density of proteins that cover the length of the phage and can be modified with high affinity peptides to serve as biorecognition elements. The wild-type M13 phage is 880 nm long and 6.5 nm in diameter. Approximately 2700 identical copies of the major coat protein (pVIII) are displayed along its length, each serving as a potential bioreceptor. Phage biorecognition elements can also be rapidly and inexpensively manufactured in large quantities through infection of a bacterial host without need for animal immunization. Zhu reported an optofluidic based WGM sensor using M13 as the bioreceptor[14] while Horikawa M13 as bioreceptors for magnetoelastic sensors[40]. Polymer-M13 composite based biosensor working as electrochemical sensors[41] have also been reported, highlighting the versatility of the M13 as bioreceptors.

1.4 Near field electrospinning (NFES) for biosensors

Fabrication also plays an important part in dictating cost and performance of a biosensor. Parallel to the research in WGM transducers and M13 bioreceptors, work by various groups have utilized electrospinning to fabricate biosensors. In this technique, a polymer droplet is induced to form a fiber using a strong electric field. The balancing forces of the polymer resistive forces (surface tension, viscosity) and the attractive force of the electric field induce a Taylor cone and a straight polymer jet begins to deposit. As the jet travels, solvent evaporates, and a solid nanofiber/microfiber is formed. Control of viscosity, surface tension and electric field are all known to control fiber diameter and resulting fibers electrospun[42,43]. In typically electrospinning setups (called far-field

electrospinning), the straight jet formed undergoes instabilities creating a random whipping motion and causing a random mat of fibers to deposit. While this may not be ideal, the ease with which biorecognition elements or other functional materials can be incorporated has spurned the fabrication of various biosensors[16,17,44].

Electrospinning has also been utilized to fabricate optical sensors such as random cavity lasers for vapor sensing[45] or as a fluorescence sensor for free radicals[46]. Ponce-Alcántara, demonstrated that electrospun fibers could act as FTIR sensor[47]. In recent years, electrospun fibers have been demonstrated to support WGM[48,49]. However, the fabrication of an electrospun WGM biosensor has yet to be reported. Such a sensor could combine the attractive qualities of the WGM and M13 bioreceptor with the benefits of electrospinning.

A variant of electrospinning, near-field electrospinning (NFES) may be more useful in this regard. While far field electrospinning typically spins random mat of fibers, with NFES, the use of an X-Y stage and closer tip to collector distance has allowed for the precise patterning of electrospun fibers. NFES has been used to fabricate well-organized fiber meshes[50], and suspend fiber across posts[51]. Furthermore, NFES typically spins microfiber-sized fibers, more suitable for WGM resonators.

1.5 Scope of Research

This dissertation focuses on the NFES fabrication of active WGM in PVA and PVA/M13 fibers for WGM sensing and biosensing (Figure 1-2). Polyvinyl alcohol is a common biocompatible polymer used in various bio-composite applications[52,53]. The PVA

fibers formed a circular cross-section and were used to support WGM resonances in aqueous environments. PVA solutions were mixed with M13 and NFES. The resulting bio-composite fibers retained the functionality/biorecognition of M13. As a model system, the PVA/M13 were used for WGM biosensing. Finally, an electrostatic interaction was developed during the NFES process. The resulting process was used to increase M13 surface concentration to improve the PVA/M13 biosensing response.

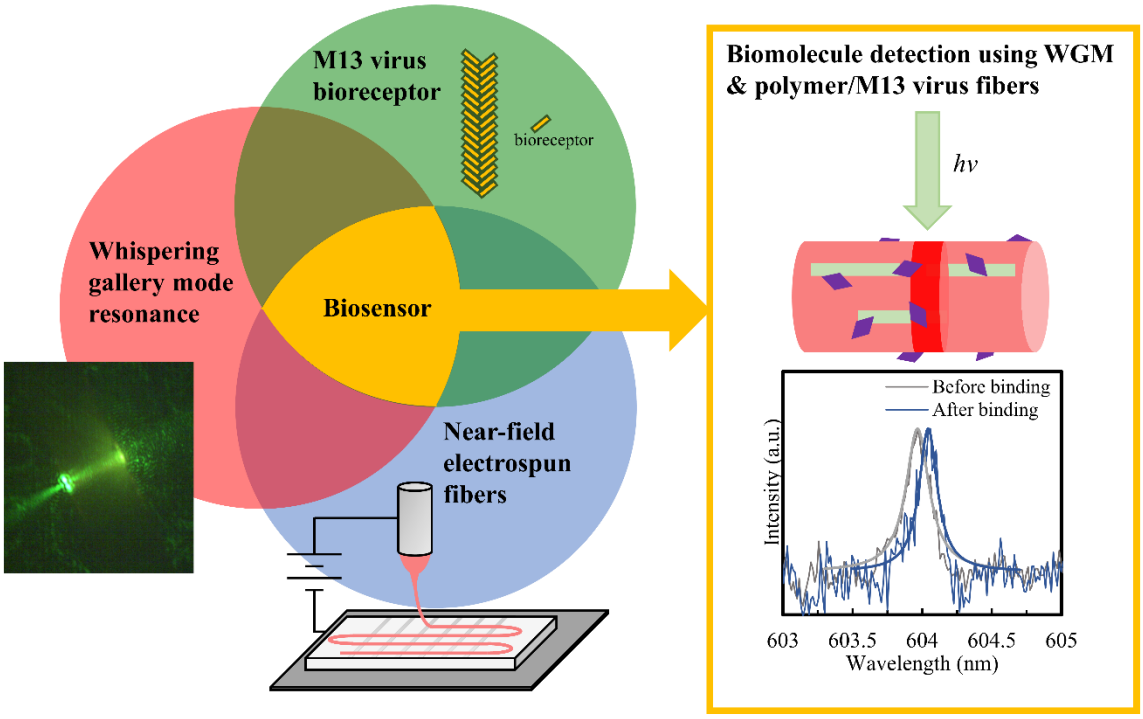

Figure 1-2: Schematic of research approach

Chapter 2 focuses on fabricating a water-stable PVA fiber for aqueous applications. The water-soluble PVA solutions are first electrospun into fibers and then chemically treated to form a crosslinked network. The fibers were assessed for water stability and WGM stability in water. A Mie-theory approximation was developed to determine key WGM parameters. Initial sensing experiments utilized the water-stable PVA fibers as model bulk refractive index WGM sensors (e.g., water-ethanol solutions). The complex hydrogel interaction of PVA and ethanol was further examined using the same Mie-theory approximation.

Chapter 3 focuses on fabricating a PVA/M13 bio composite fiber for WGM biosensing. The PVA/genetically modified-M13 solutions were characterized and electrospun into microfibers. M13 formation and binding activity after electrospinning was assessed. The PVA/M13 fibers were used to detect the presence of streptavidin, demonstrating potential as a WGM biosensor.

Chapter 4 focuses on the interaction of the electric field and M13 during the NFES process. The strong electric field formed during electrospinning is used to migrate M13 towards or away from the fiber surface. Using M13 with different surface charges and different electric field polarities, the electrostatic interaction during electrospinning was explored. The enriched M13 surface and depleted M13 surface were used for WGM biosensing.

Chapter 2 Near-field electrospun PVA fibers for sensing aqueous solutions

2.1 Introduction

Whispering Gallery Mode (WGM) resonators are a class of resonators where light recirculates along the periphery of a cavity. Formed by light undergoing total internal reflection (TIR), only specific wavelengths of light can form standing waves, thereby creating the WGM resonance. Because of TIR, a portion of the WGM electromagnetic field forms an evanescent field, extending into the environment. For sensors, the evanescent wave has been utilized as a transducer to detect small changes in its local environment [30,31]. This has enabled WGM-based biosensor sensitivity down to a single biomolecule[31].

WGM biosensors have been fabricated in different geometries such as spheres[24], disks[24,54], microbubbles[26] and fibers[27] and different materials such as silicon oxide and polymers. Polymer based WGM biosensors are of interest due to their low-cost and ease of manufacturability while still retaining biocompatibility. One emerging technology for the fabrication of polymer fiber based WGM resonators, is electrospinning, a technique that utilizes a strong electric field to produce polymer fibers at large scale. Electrospinning has been demonstrated with bio-compatible polymers and biological agents. A variant of electrospinning, known as near-field electrospinning

(NFES), combines the production scale of electrospinning with direct-write capability using translational stages.

Previous work[55] established a methodology of fabricating polyvinyl alcohol (PVA)/ Rhodamine 6G fibers using NFES. The PVA/R6G fibers were shown to able to support WGM resonances and were utilized for vapor sensing of various solvents. Additionally, PVA is well known for its biocompatibility and water solubility, able to easily incorporate biological bioreceptors into its polymer matrix without need for complex solvents which might alter the electrospinning process.

However, for aqueous applications, PVA and Rhodamine 6G water solubility presents a difficulty. The high surface-to-volume ratio of the fibers means the fibers dissolve rapidly in aqueous environments, rendering them unusable as aqueous sensors. Due to the popularity of PVA in different applications, several strategies have been devised to prevent water solubility. Typically, the methods can be separated into either a physical crosslinking approach or a chemical crosslinking approach. Physical crosslinking has been achieved using freeze-thaw, radiation[56], or a physical crystallization using a chemical agent such as methanol or ethanol [57–60]. In contrast, chemical crosslinking relies on forming chemical bonds between different polymer chains through linker molecules. As the hydroxyl group of PVA is readily available, a number of different crosslinking agents have been explored [61–63]. We chose to use glutaraldehyde (GA) as the crosslinking agent due to the number of different biocompatible/bio-composite reports[64–66], including with M13 [67]. Additionally, several groups reported successful crosslinking of electrospun PVA-GA fiber[65,68,69].

The crosslinking reaction between GA and PVA involves a reaction of the PVA's hydroxyl groups with the GA aldehyde to form acetal bond[69]. While the reaction is thought to be more complicated for protein interactions[70], the assumption of the formation of acetal bonds formation will only be considered for PVA/GA reactions. These reactions have 3 potential outcomes, a partial acetal bond on one side of the GA molecule, and intramolecular bond and intermolecular bonding[69]. Critical for aqueous PVA applications is the formation of intermolecular bonding or crosslinking between different PVA chains. This may indicate an optimum crosslinking condition to promote intermolecular bonding. Different groups have utilized both GA vapor and aqueous GA to form crosslinked PVA membranes usually with an HCl catalysis.[69,71,72]. It is also important to note that for WGM aqueous applications, the GA treated PVA fibers needed to be water stable, smooth and able to support its own circular cross-section without sagging.

For this work, electrospun PVA and PVA/R6G fibers were treated with GA to develop a crosslinking procedure that would result in water stable fibers. Using a combination of liquid and vapor treatments, crosslinked fibers were shown to have minimal water swelling under optical microscopy and no observable R6G dye release. Under far-field excitation, the crosslinked fibers were still able to support WGM in aqueous solutions despite the lowered refractive index contrast. The fibers were further shown to be stable in solution over time agreeing with both optical microscopy and R6G dye release experiments. As a model system, fibers were placed in water-ethanol mixtures and the concentration was increased incrementally. Theoretical spectra were

compared to empirical results to investigate sensing mechanisms by estimating the changes in fiber diameter and optical mode effective refractive index associated with the observed wavelength shifts. Due to the hydrogel nature of crosslinked PVA, individual contributions of fiber shrinking and refractive index changing was determined. These results demonstrate the potential for a NFES crosslinked PVA fiber to function as a sensitive transducer for sensor and biosensing applications.

2.2 Experimental methods

2.2.1 Fabrication and characterization of electrospun polymer fibers

Fibers were fabricated according to previous work[55]. Briefly, PVA (M_W: 13,000-23,000 g mol^{-1}, 98% hydrolyzed, Sigma Aldrich) was dissolved in deionized water and mixed with a magnetic stir bar in a hot water bath at 80°C for 2 h to obtain a homogeneous 25 wt% solution. The mixture was cooled for 1 h under ambient conditions. For active emitter applications, Rhodamine 6G (R6G, Sigma Aldrich) was also dissolved in deionized water to obtain a 0.0035 g PVA/g R6G solution. The dye-doped polymer solution was loaded into a 1 mL syringe and pumped through a 27-gauge blunt-tip needle at a rate of 10 µL h^{-1} using a syringe pump (NE-1010, New Era). A high voltage source (NO3.5HP8.5, Acopian) was used to apply a 2 kV to the needle tip. A glass substrate of dimensions 15 x 15 x 1 mm was used as the collector and was placed on top of an X-Y stage (A-LSQ300D, Zaber) programmed to move in a parallel-line pattern. The substrate was scribed with lines perpendicular to the intended fiber deposition direction to allow fibers to be suspended. Approximately 1 cm long fibers

were written 200 μm apart from each other. The needle tip-to-collector (T-t-C) distance was fixed at 1.25 mm, at a stage speed of 0.5 mm s^{-1}. Electrospinning occurred under ambient temperature, pressure, and humidity. Electrospun fiber diameters were characterized using a digital optical microscope (KH-7700, Hirox) with a 35x objective and built-in measurement software. Confocal fluorescence microscopy (SP5, Leica Microsystems) was used to image the dye-doped fibers and fiber surface roughness was measured using tapping mode atomic force microscopy (AFM, Dimension Edge, Bruker) and a silicon tip.

2.2.2 Crosslinking fibers and water stability characterization

The water-soluble PVA fibers were chemically crosslinked with glutaraldehyde (GA) to make them water stable. Different vapor and liquid treatments, derived from previous reports ,were developed to crosslink the PVA fibers while still maintaining the ability to support WGMs.[69,73]. For different treatment conditions, 1-step GA vapor treatment, 2-step GA vapor treatment, and 3-step GA vapor-vapor-liquid treatments were utilized. For all treatments, fiber ends were glued to the substrate, placed in a closed chamber. Volumes of GA to HCl during vapor treatments were 1:1. During the 1-step GA vapor treatments, fibers were simultaneously exposed to vapor from 50% GA solution and different concentration HCl solution (1M-5M) for 24 hours. For 2-step treatments, fibers underwent 2 sequential 24 hour vapor treatments. Fibers were exposed to 50% GA and 1M HCl vapor for 24 hours then another 50% GA and 3M HCl vapor for another 24 hours. A 3-step process (2 vapor, 1 liquid) was also developed. Fibers were exposed to

vapor from 50% GA solution and 1M HCl for 24 hours, then 50% GA and 5M HCl for another 24 hours. For the last step, the fibers were submerged in a 50% GA for 24 hours, rinsed thoroughly with water, and allowed to dry under vacuum. Fiber diameters (*D*) over time in water were measured using a digital optical microscope (KH-7700, Hirox) and used to calculate swelling ratios ($D_{meaured}/D_{intial}$). Dye release experiments were carried by submerging the fibers in 10 ml water bath for 7 days. Undiluted aliquots of the bath solution were taken and measured using ultraviolet–visible (UV-Vis) spectroscopy (ThermoFisher, Evolution 60) at 2 and 7 days.

2.2.3 Optical WGM measurement and sensing

WGMs were excited in the crosslinked PVA/R6G fibers using a far-field laser confocal system (LabRam, Horiba Scientific)[74]. Briefly, a 532 nm continuous wave (CW) laser (Ventus, Laser Quantum) was focused through a 50x objective (NA = 0.75), resulting in a spot size of approximately 3 μm and an incident laser power of 6 μW. Emission was collected using the same objective, directed through a long pass filter (>532 nm) into a spectrometer with an 1800 lines/mm diffraction grating and a charge-coupled device (CCD) detector. For aqueous applications, the fibers were first submerged into a water bath. Emission was recorded at 3 min intervals to prevent photothermal effects and minimize bleaching. Laser light was blocked in between measurements.

To determine important WGM parameters and azimuthal mode numbers, theoretical spectra were obtained by using a Mie-theory derived approximation[22,23]

$$\lambda \cong \pi n_{res} D \left[\nu + \frac{\alpha_s \nu^{\frac{1}{3}}}{2^{\frac{1}{3}}} - \frac{P}{(m^2-1)^{\frac{1}{2}}} + \frac{3}{10} \frac{{\alpha_s}^2}{2^{\frac{2}{3}} \nu^{\frac{1}{3}}} - \frac{P\left(m^2 - \frac{2P^2}{3}\right)}{(m^2-1)^{\frac{3}{2}}} \frac{\alpha_s}{2^{\frac{1}{3}} \nu^{\frac{2}{3}}} \right]^{-1} \quad (1\text{-}3)$$

where D is the optically measured fiber diameter, v is the angular mode number (l) plus 0.5, α_s are the roots of the Airy function, and n_{res} is the refractive index of the resonator. The term m is the ratio of the refractive index of the resonator to the refractive index of the surrounding medium (n_{res}/n_{host}). P is $1/m$ for TM modes and m for TE modes, respectively. The refractive index of the surrounding medium (n_{host}) was taken as either 1.333 for fibers in water or was based on literature measurements for ethanol-water concentrations[75] with values ranging from 1.3325 to 1.3494. Equation (2-1) was evaluated by incrementally varying D, n_{res} and azimuthal mode number. Solutions were compared to fluorescence spectra obtained from the WGM fibers, and the least mean residual squared was taken as the best fit using MATLAB code written. The range of input D and n_{res} values used to determine best fit corresponded to optical images and ellipsometry measurements, respectively. For sensing of ethanol-water mixtures, measurements made within 5 min of ethanol addition were disregarded due to transient behavior and the mode number was constrained despite changing ethanol-water concentrations.

2.3 Results and Discussion

2.3.1 Fabricating and crosslinking of PVA fibers

Fibers were electrospun using a stage speed of 0.5 mm/s with a tip-to-collector distance of 1250 μm. Under an applied voltage of 2kV, PVA and PVA/R6G solutions were fabricated onto to prepared glass substrates. A 542 nm laser was used to excite the R6G, and the resulting fluorescence was measured. As shown in Figure 2-1a, the distribution of

R6G fluoresced uniformly within the fibers. Surface roughness was evaluated using AFM. Fiber measured a root-mean-squared roughness of 2.4 nm (Figure 2-1b). The fibers were assessed to be adequate for WGM excitation. However, the water-soluble PVA presented an issue for aqueous applications, dissolving too quickly for practical applications. For aqueous WGM applications, the PVA fiber needed to be water-stable while still retaining the smooth fiber surfaces and fiber geometry with no R6G dye leakage.

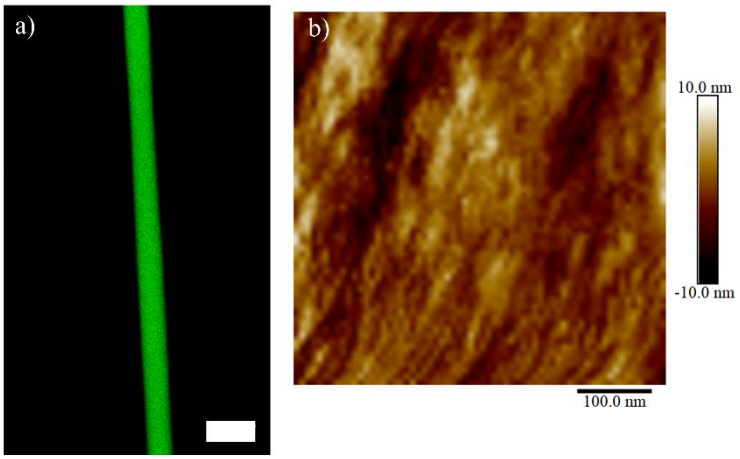

Figure 2-1: a) Fluorescent emission b) AFM image of the surface of a dye-doped PVA fiber electrospun with a stage speed of 0.5 mm s^{-1} and a R6G/PVA mass ratio of 0.0035. The measured root-mean-squared roughness was 2.4 nm.

Based on reports of electrospun PVA fibers treated with GA[69,73], a vapor treatment was thought to be gentle enough to preserve fiber geometry and surface roughness. Using a similar setup as reported by Shaikh[73], electrospun fibers were placed above containers of GA and differing concentrations of HCl as an acid catalyst inside a vacuum chamber. Ambient temperature and pressure caused the GA and HCl to reach equilibrium vapor pressure and react with the PVA fibers. Initial experiments utilized 50% GA vapor and differing amounts of HCl 1M – 6M for 24 h. In all cases, the fibers were not water stable, dissolving quickly when placed in water. This was attributed due to the inadequate crosslinking between GA despite, in some cases, the high HCl catalyst concentration. Additionally, at 50% GA and 6M HCl vapor, the GA began to self-polymerize, forming a light brown substance, preventing the use of a harsher catalytic environment.

Instead, a 2-step vapor treatment of 50% GA and1M HCl vapor followed by 50% GA and 3M HCl vapor treatment for another 24 hours was developed. The resulting fibers were water-stable, but these fibers displayed a significant relative swelling ratio of 1.26 ± 0.21 (Figure 2-2). Interesting, in one run, the fiber diameters did not plateau indicating potential instability or reliability with this treatment. Further experiments with GA treatment using 1M and then 5M HCl vapor led to fibers still swelling significantly. While these initial results were promising, for use as bulk refractive index sensing, swelling introduces a non refractive index based mechanism for WGM shift. Unfortunately, due to the high concentration of HCl catalyst used in the 2nd vapor step, a stronger vapor treatment was not possible. To further crosslink the fibers and prevent

water-swelling, the fibers were fully submerged in 50% GA. Due to the fibers already being water-stable after the 2-step treatment, it was assumed that the additional liquid GA would not significantly impact the fiber geometry and cross-section. As shown in Figure 2-2, PVA fibers treated with this 3-step process [50% GA + 1M HCl (vapor), 50% GA + 5M HCl (vapor), 50% GA (liquid)] were shown to have minimal relative swelling (1.00 ± 0.00) with a fast plateau. When the fibers were placed in a water bath, no significant R6G absorbance was detected in the bath solution for at least 7 days (Figure 2-3), indicating the crosslinking conditions were adequate to retain the active emitter. The 3-step process demonstrated the best and least complicated water stability, ideal for initial aqueous WGM detection. The fiber diameters of both uncrosslinked and crosslinked fibers were measured using optical microscopy (Figure 2-4). Crosslinked fibers were noted to increase in average diameter, 14.3± 5.3 μm, compared to uncrosslinked fibers 12.4± 3.7 μm. It should be noted that during the GA treatment process, the crosslinked fibers were rinsed to remove excess GA prior to optical measurements. While they were vacuumed before diameter measurements, absorbed water within the PVA fibers may partially account for the fiber diameter increase measured rather than purely due to the GA crosslinking process. Nonetheless, the long-term stability in water and minimal fiber diameter swelling over time made the 3-step GA treatment ideal for subsequent aqueous WGM detection and water-ethanol sensing experiments.

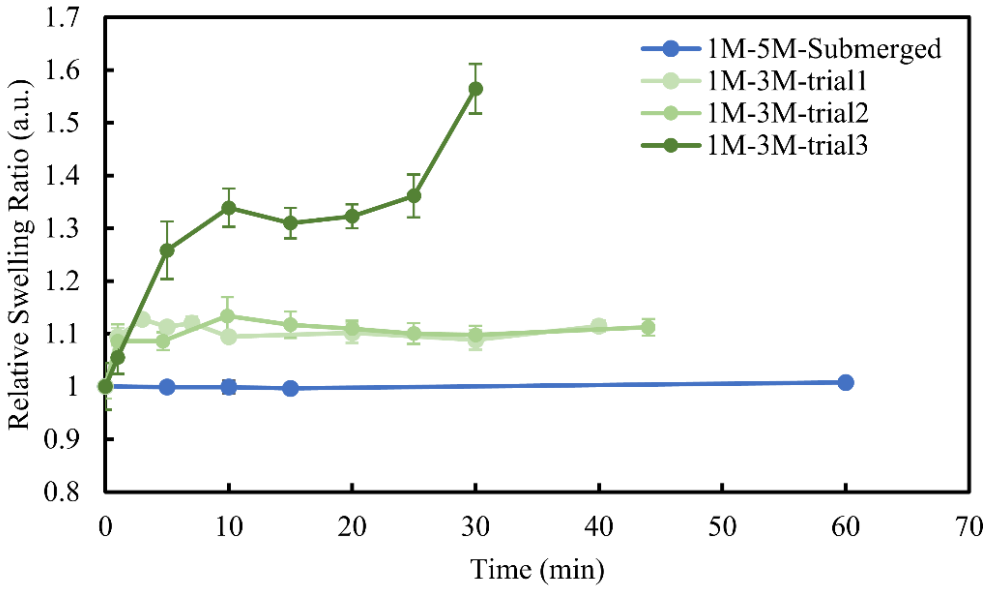

Figure 2-2: Relative swelling ratio of GA treated fibers immediately after submerging in water. Conditions shown: [50% GA + 1M HCl (vapor), 50% GA + 3M HCl (vapor)] & [50% GA + 1M HCl(vapor), 50% GA + 5M HCl(vapor), 50% GA (liquid)]

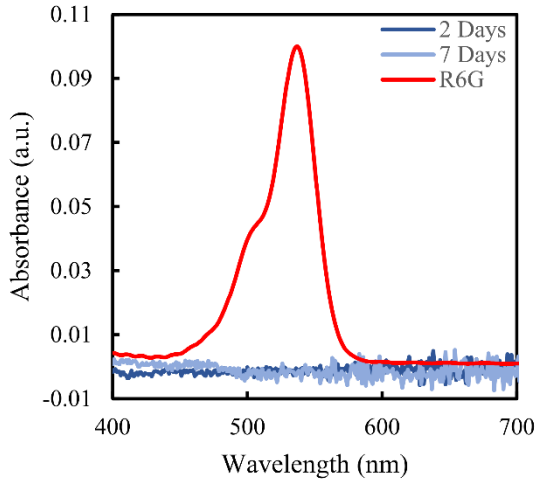

Figure 2-3: UV-vis after soaking crosslinked PVA/R6G fibers in water for different days. R6G absorbance is shown as reference

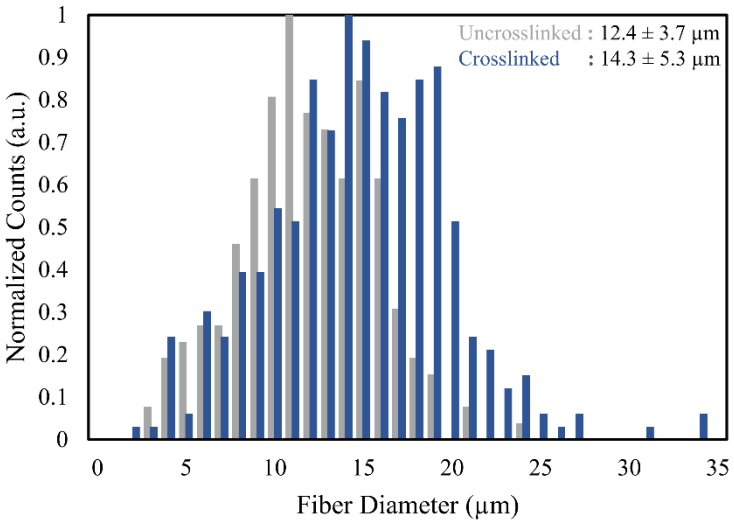

Figure 2-4: Fiber diameters of uncrosslinked and crosslinked PVA fibers measure using optical microscopy

2.3.2 Supporting WGM resonance in aqueous environments

Crosslinked PVA fibers were evaluated to determine if they could support WGM resonance in aqueous environments. The stability of the WGM resonance was also measured, and theoretical modeling was used to identify the resonance modes and extract WGM parameters. PVA/R6G fibers were crosslinked using the 3-step GA treatment. The broad fluorescence of R6G was used as an active emitter within the PVA fibers. The dye-doped electrospun fibers were placed in a water bath. A microscope objective focused a 532 nm continuous wave (CW) laser with 6 μW of power onto the fibers and excited the R6G. Emission from the fibers was collected through the same objective and analyzed with a monochromator. Figure 2-5 shows a representative fluorescence spectrum from a crosslinked PVA/R6G fiber with a 21.1 μm diameter, as measured optically. The broad R6G fluorescence background was decorated with pairs of peaks that repeated throughout the wavelength measured. The shorter wavelength in the pair was attributed to transverse magnetic (TM) WGM resonance, while the longer wavelength peak was assigned as transverse electric (TE) modes based on previous experiments[74]. The peaks were fitted using a Lorentzian and were observed to have a free spectral range (FSR) of 3.614 nm. From the Lorentzian fits, the quality factor of the peaks measured was calculated according to the equation:

$$Q = \frac{\lambda_{Resonance}}{\lambda_{FWHM}} \tag{2-2}$$

with an average Q-factor of 5828 ± 1450.

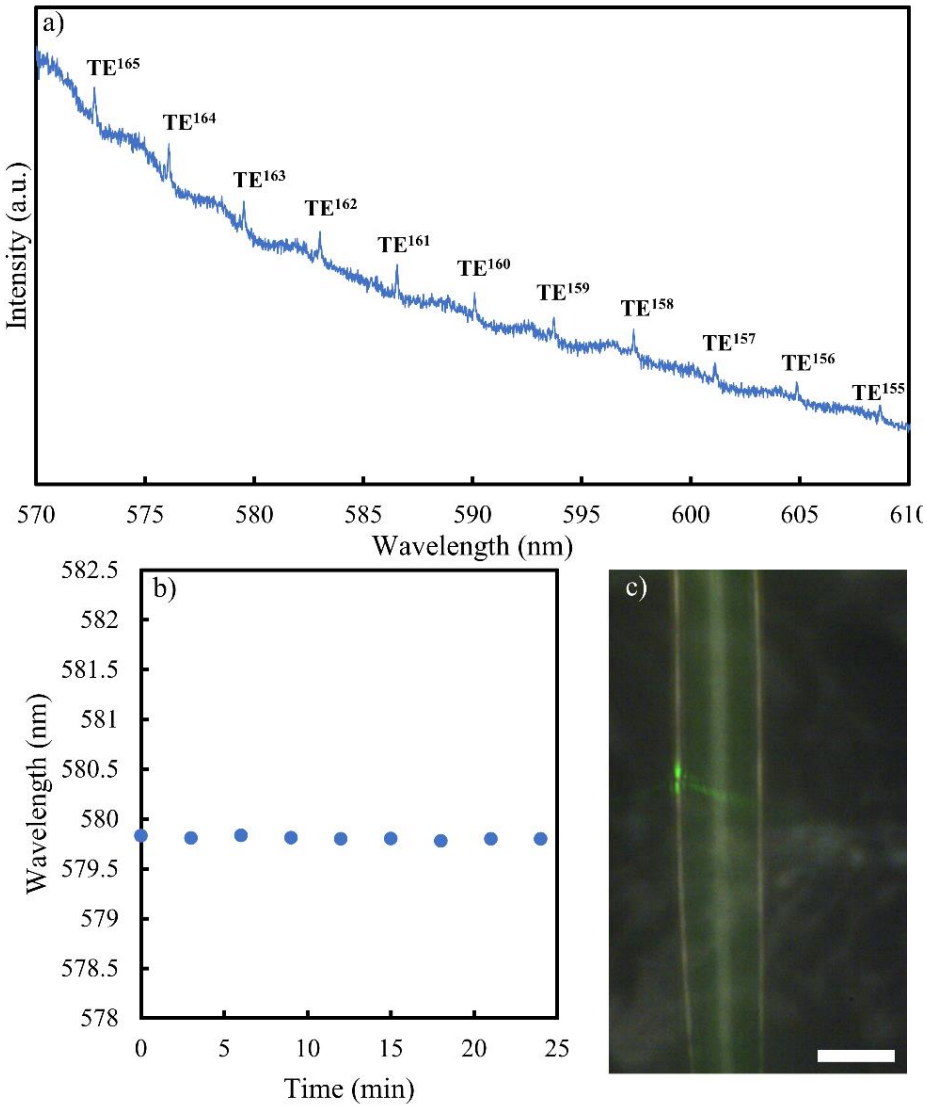

Figure 2-5: a) Representative fluorescence spectrum of a crosslinked R6G-PVA fiber in water. The spectrum was taken with a 50x long working distance objective under 532 nm CW illumination, using conditions similar to ethanol-water chemical sensing. The shutter was closed between measurements. b) The peak wavelength as a function of measurement time for mode near 580 nm. WGM resonance wavelength remains stable over time. c) An optical image of a 21.1 μm diameter electrospun fiber WGM resonator in water under laser illumination. Scale Bar: 20 μm

To confirm these were WGM and calculate the WGM parameters (radius, mode number, refractive of resonator and host) for this experiment and future experiments, a fitting approach based on a Mie-theory derived approximation (Equation 2-1) was developed[22]. For this spectrum, due to the low Q of the TM modes, only the TE modes were fitted. Resonances were assumed to be first-order radial WGMs, as these are typically the lowest loss modes. To determine which WGM parameters best described this spectrum, empirical peak positions were compared to the theoretical peak computed for all defined parameters space. Potential parameters varied include the resonator's diameter, azimuthal mode number, refractive index of the resonator, and host medium. A MATLAB program computed all possible solutions to the Mie-theory approximation, and the goodness of the solution was determined through the least sum of the residuals squared, similar to other reports[76]. An example calculation to fit measured peak 572.679 nm assuming azimuthal mode number = 165 and a water refractive index of 1.333 with the plotted residuals squared is shown in Figure 2-6a. Due to the large number of possible solutions with poor fitting, a filter function was included to remove non-relevant solutions (filter = 0.05 nm) to reduce memory space and increase computation speed (Figure 2-6b). This removed any solution with a theoretical peak position greater than 0.05nm compared to the measured peak position. To solve for the parameters that best fit the entire spectrum, solutions to equation 2-1 were computed sequentially for all peaks in the spectrum. As each peak is assumed to be related by an increment of azimuthal mode number, the shortest wavelength peak was solved first, and the parameter and solution were stored. Using the same parameters except for deducting the azimuthal

mode number by 1, the next longer wavelength peak in the sequence was solved. This continued until all peaks were solved for. The filter function was used at each step to remove non-viable solutions. Careful care was taken to choose increment sizes that would fully sweep each parameter space. For Figure 2-5 the refractive index of water was assumed to be 1.333, and the initial assumption of fiber diameter, $n_{res\ were}$ based on optical and ellipsometry measurements, respectively. Mode assignments in Figure 2-5a correspond to a diameter of 21.8 μm and n_{res} of 1.441 (TE), in agreement with the optically measured fiber diameter. Under repeated measurements, the 572.679 nm peak demonstrated peak position noise, σ = 0.016nm, with no significant trends. The lack of trend supported optical microscopy evidence that the crosslinked PVA fibers were water stable while also demonstrating that heating or bleaching effects were minimal during WGM measurements. Given the higher Q factor and higher intensity, TE modes were utilized for aqueous sensing.

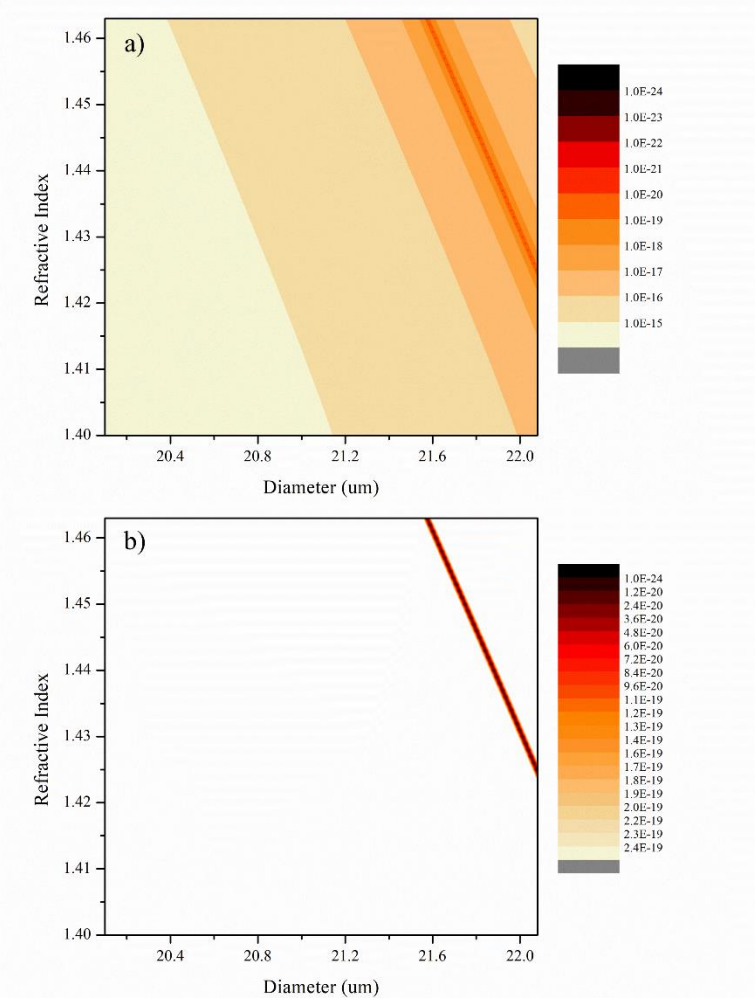

Figure 2-6: Residuals squared for the data spectrum in Figure 2-3. l was assumed to be 165. the radius step size was 1nm and the refractive index step size was 0.001

2.3.3 Ethanol-water sensing

WGM resonators have shown great utility as chemical and biological sensors.[77–79] Electrospun R6G-PVA micro-fibers were assessed as chemical sensors using ethanol in water as a model system. A crosslinked WGM fiber resonator was placed in a water bath, as in Figure 2-7a, and optical spectra were collected. For ethanol-water sensing, the ethanol concentration was increased in 10% (v/v) increments. Figure 2-7b shows that a corresponding redshift in WGMs resonant wavelength, associated with increasing ethanol concentration. The resonant wavelength of the mode initially observed at 613.5 nm was plotted as a function of time in Figure 2-7c. Immediately after each addition of ethanol, the resonant wavelength rapidly increased and then plateaued, consistent with a refractive index increase with increasing water-ethanol concentration. Figure 2-7d depicts the resonance wavelength of the same peak versus ethanol concentration. The spectral response of the resonator was linear within the range of ethanol concentrations measured, resulting in a sensitivity of 0.1133 nm/%.

As demonstrated in Figure, 2-8a, the sensitivity of the cavity to ethanol concentration was wavelength dependent, due to decreased light confinement at longer wavelengths. Using the relationship between refractive index and ethanol concentration found in previous reports[75], the measured sensitivities were comparable to those of other polymer-based WGM resonators. As an example, dye-doped PMMA/epoxy resin fibers[77] had a sensitivity of approximately 0.1391 nm/%. Similarly, hollow PMMA fibers embedded with a dye-doped micro rings[80] demonstrated sensitivities near 0.1245 nm/%.

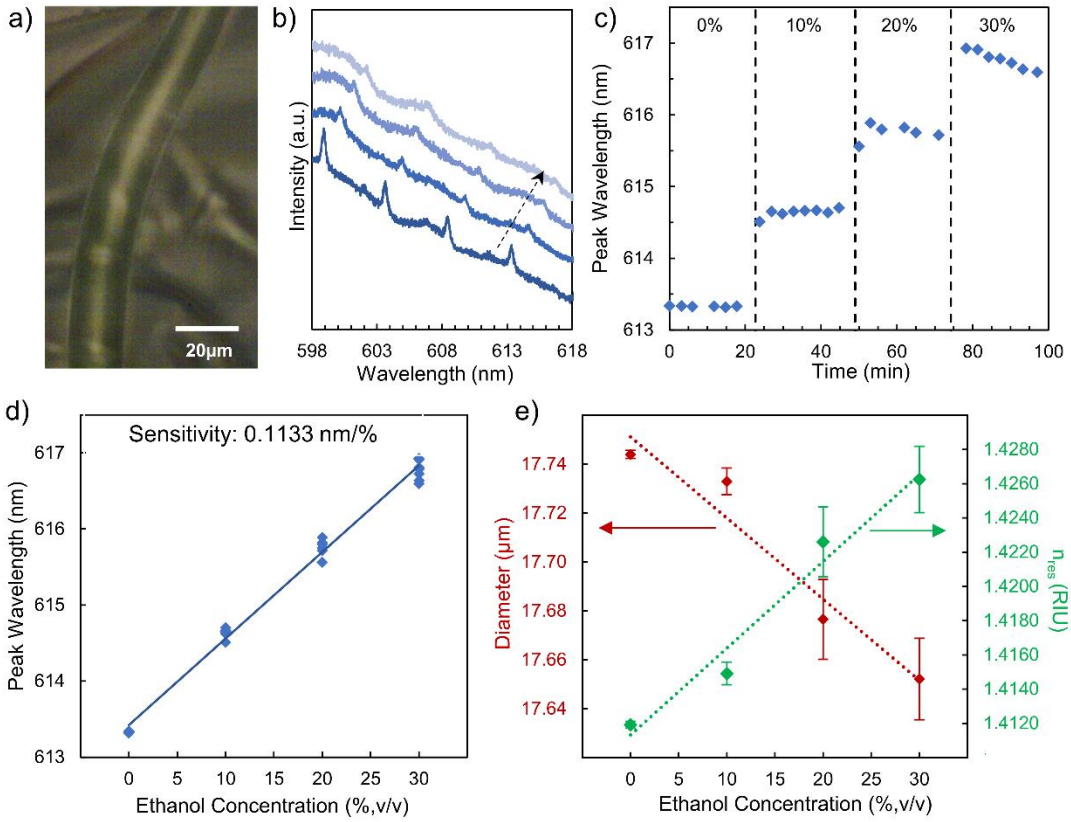

Figure 2-7: a) A 15.9 µm diameter WGM fiber sensor submerged in a water bath. b) Fluorescence spectra of fiber resonator in 0%, 10%, 20%, and 30% (v/v) ethanol-water solution. Arrow indicates increasing ethanol concentration. Emission intensities are offset for clarity. c) Peak emission wavelength of the mode initially observed at 613.5 nm as a function of time. A red-shift in WGM resonance was observed for each increase in ethanol concentration (as denoted by dashed, vertical lines). d) Peak emission wavelength as a function of ethanol concentration. The calculated sensitivity within this linear performance region was 0.1133 nm/%. e) Calculated resonator diameters and effective refractive indices with increasing ethanol concentration; fiber diameters shrunk slightly, while n_{eff} increased. Each data point represents the average fitted diameter or n_{eff} obtained. *Data was obtained in collaboration with Dr. Joseph Cheeney.*

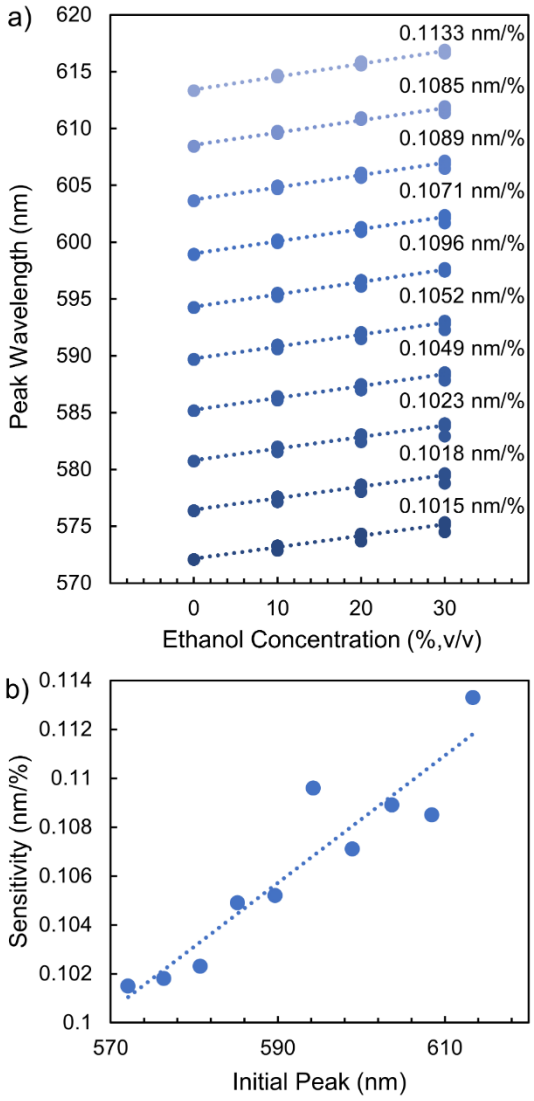

Figure 2-8: a) Peak emission wavelength as a function of ethanol concentration for the same 15.9 µm fiber shown in Figure 2-7a. b) Plot of sensitivity versus wavelength for each resonance peak. Sensor sensitivity increases for longer wavelength. *Data was obtained in collaboration with Dr. Joseph Cheeney.*

Both volumetric and effective refractive index changes can contribute to WGM wavelength shifts and sensor performance. The relationship between resonance shift and these mechanisms can be expressed by

$$\frac{\Delta\lambda}{\lambda} = \frac{\Delta n_{eff}}{n_{eff}} + \frac{\Delta D}{D} \quad (2\text{-}3)$$

Due to the evanescent field associated with WGMs, the effective refractive index (n_{eff}) depends on both n_{res} and n_{host}. Unlike inorganic optical resonators, the addition of solute can cause changes in the n_{res} of polymer cavities through solute uptake, as well as n_{host}. Furthermore, solute uptake can be accompanied by resonator dimensional changes. Indeed, other WGM polymer-based cavities have demonstrated the combined influence of environmental refractive index, solvent uptake, and/or cavity expansion or contraction on sensor response[45,76,81–83]. When exposed to alcohol vapors, both swelling and vapor uptake caused redshifts in resonances of random optical networks of poly(methyl methacrylate) (PMMA) fibers[45]. Similarly, interaction of volatile organic compounds with PDMS-coated SiO_x quasi-toroidal ring resonators resulted in a redshift which could be parsed in to contributions from polymer swelling and an increase in n_{res}[83]. Additionally, solvent penetration and swelling were observed for WGMs in polystyrene microbeads immersed in alcohol solutions, although changes in n_{host} dominated sensor performance[76].

To understand the transduction mechanisms associated with the crosslinked, dye-doped PVA WGM fibers, the sensing spectra were examined using, using the same Mie theory-based asymptotic formula (Equation (2-1)) iterative solving approach. The

approach was used to extract best fit values for D, n_{res} and azimuthal mode number. n_{host} at different water-ethanol concentrations were determined from literature [75]. Similar Mie theory approaches have been used to account for dimensional and refractive index changes associated with humidity, or adsorbed polyelectrolyte and biomolecule layers[19,29,82]. The average best fit diameters and n_{res} for all sensing spectra as a function of ethanol concentration are shown in Fig. 2-7e. As the ethanol concentration increased from 0 to 30%, the calculated D shrank approximately 90 nm or just 0.5%. The reduction in diameter is consistent with reports of highly crosslinked PVA hydrogels with a large degree of hydrolysis in ethanol-water solvent mixtures[84–86]. Conversely, n_{res} increased with ethanol concentration. As the refractive index of ethanol is larger than water and could be attributed to slight uptake of ethanol displacing water within the fiber. The resonance peak is expected to blue-shift as fiber diameter shrinks and red-shift as n_{eff} increases. As a net redshift was observed with increasing ethanol concentration, the sensing performance of the WGM fiber was dominated by an effective refractive index change rather than dimensional change. Further studies are required to understand the relative contribution of the change in n_{res} or n_{host}

2.4 Conclusion

To conclude, NFES was used to fabricate PVA/R6G fibers. Utilizing chemical crosslinking with glutaraldehyde, the PVA fibers were shown to be water stable. The fibers were still able to host WGM resonances when submerged in solvent, despite the lowered refractive index contrasts. These fibers were further confirmed to be water-stable

through optical microscopy, dye release, and WGM spectra monitoring. Despite emission spectrum complexity, chemical sensing of the ethanol-water system exhibited a sensitivity of 0.1133 nm/%. NFES of dye-doped polymer microfiber WGM resonators has proven promising as a straightforward, inexpensive fabrication approach. Given the biocompatibility of PVA, the ease in fabricating water-stable PVA WGM resonators a polymer-based WGM biosensor with incorporated bioreceptors is within reach.

Chapter 3 PVA/Phage fibers for label free biosensing

3.1 Introduction

The rapid and affordable detection of biomolecules has become a critical part of modern infrastructure. Development of sensitive and effective biosensors for biomarkers, viruses, and bacteria enables routine biomedical diagnostics, environmental monitoring, and food/water quality control. One interesting class of devices, label-free optical biosensors, targets chemical and biological agents without the need for additional fluorescent or radioactive tags, thus offering on-site and real-time detection of analytes[79]. These optical devices can also operate in harsh environments as they are not vulnerable to electromagnetic interference. In recent years, whispering gallery mode- (WGM-) based biosensors, a type of label-free optical biosensor, have shown promise due to their compact size, high sensitivity[6], and fast response time (*i.e.*, tens of seconds)[7]. Light is confined by total internal reflection at the periphery of these curved boundary high quality (Q) factor resonators and recirculates, acting as an optical probe capable of detecting minute concentrations of biomolecules. This promising technology has led to development of WGM sensors able to detect cancer biomarkers[87], bacteria[88], pesticides[89] and water contaminants[90].

Silica glass or other silicon-based compounds (*e.g.* silicon, silica, silicon nitride)[54,79,91–97] and polymers[78,98–100] are the most widely used materials for WGM optical biosensors. Because these materials lack specificity, resonators must be

functionalized to recognize target analytes[14,87,101–104]. Device performance and manufacturability depend on the selection of both an effective biocapture agent and immobilization strategy. Bioreceptor efficacy is determined by surface density, orientation, and stability, among other factors. Antibodies, enzymes, and oligonucleotides are common biorecognition elements[1,9]. Unfortunately, these fragile biomolecules are vulnerable to extreme environments, and often have limited binding sites that require specific orientation to ensure functionality. Moreover, they can be expensive to produce and use, requiring mammalian cell lines, sophisticated purification techniques, and/or repeated functionalization steps to achieve high receptor density.

In recent years, filamentous bacteriophages such as the M13 have attracted the interest of a handful of researchers as alternative affinity-based[11–14] bioreceptors. These viruses have a large density of proteins that cover the length of the phage and can be modified with high affinity peptides to serve as biorecognition elements. The wild-type M13 phage is 880 nm long and 6.5 nm in diameter. Approximately 2700 identical copies of the major coat protein (pVIII) are displayed along its length, each serving as a potential bioreceptor. Compared to individual covalently-linked or affinity bound capture agents, the viral scaffold ensures a dense, ordered arrangement of high affinity peptides with the proper orientation for analyte binding. Known as a combinatorial phage display workhorse, these viruses are also advantageous in that they can be used to construct random libraries from which peptides or proteins with affinity for a specific analyte can be selected and used without avidity concerns. Moreover, unlike other frequently used biorecognition elements, phage are chemically and thermally robust, tolerating both

acidic and basic pH and temperatures up to 70°C[39]. Phage biorecognition elements can also be rapidly and inexpensively manufactured in large quantities through infection of a bacterial host without need for animal immunization.

Complex, multi-step processes are typically required for immobilization of biocapture agents on the sensor surface. For example, for silicon-based resonators, amino-terminated silanes are paired with an appropriate crosslinking chemistry to achieve covalent linkage of bioreceptors[105–108]. This process requires several steps including surface hydroxylation via acid dip or oxygen plasma treatment, vapor or liquid deposition of a silane layer, copious rinsing to remove unreacted silane molecules, and finally, attachment of biocapture agents using carbodiimide chemistry or other bifunctional crosslinking molecule[106,107,109]. Regrettably, these additional steps, beyond cavity formation, add to device fabrication costs and complexity. One simple approach to functionalization that has been used for ampere- and potentio- metric biosensors[17,110], but not yet for WGM optical biosensors, is blend electrospinning. This rapid, low-cost manufacturing method combines biorecognition elements with a polymer solution, and then uses a strong applied electric field to draw the fluid into fibers. Biosensors are fabricated and functionalized in a single step. No post-processing is required. While electrospun electrochemical biosensors have primarily used fibers a few hundred nanometers in diameter or smaller, the fabrication technique is also capable of producing larger diameter fibers on the order of tens of microns. Indeed, recent studies have demonstrated electrospun fibers capable of supporting WGM resonances[49,74], presenting an opportunity for a one-step approach to the fabrication and functionalization

of WGM optical biosensors. This study examined near-field electrospun (NFES) polyvinyl alcohol (PVA) WGM optical biosensors with incorporated M13 bacteriophage bioreceptors (Figure 3-1). Streptavidin-binding phage and rhodamine 6G were used, respectively, as a model virus-based biocapture agent and a source of high yield fluorescence. Blend electrospinning of polymer, emitter, and bioreceptor was used to achieve active cavity formation and functionalization in one step. The elimination of subsequent immobilization processes reduced fabrication complexity. Suspended, featureless fibers with circular cross-sections and an average diameter of approximately 14 μm were written over trenches on pre-patterned substrates and highly crosslinked to ensure stability in aqueous solutions and prevent swelling. Despite uniform surface appearance, confocal microscopy of fluorescently labeled phage revealed large, elongated bundles of bioreceptors aligned to the fiber axis. These large assemblies were attributed to the reduction of M13 depletion volume caused by the PVA polymer matrix. X-ray photoelectron spectroscopy (XPS) and incubation with streptavidin-coated Au nanoparticles determined that the streptavidin-binding bacteriophage were present on the fiber surface and retained affinity. This was an important finding as the specificity of a biosensor for its target analyte depends on both the availability and functionality of biocapture agents. Emission from these optically active resonators submerged in buffer was composed of a broad fluorescent background decorated with pairs of sharp peaks with moderate Q values. Using both free spectral range and a Mie-theory derived asymptotic approximation, the peaks were identified as TE and TM whispering gallery modes supported within the electrospun fiber cross-section. Electrospun PVA/M13 fibers

were employed as label-free optical biosensors for streptavidin. WGMs exhibited a red-shift in the presence of streptavidin that was not observed without the incorporation of streptavidin-binding M13 bacteriophage, indicating that the viral capture agents conferred specificity to the resonators. The theoretical lower limit of detection (LoD) was estimated to be 3 nM and a maximum streptavidin surface coverage near 21 ± 5% was calculated. The success of blend electrospinning, a potentially low-cost, large-scale manufacturing technique, in simultaneously generating and functionalizing micron-sized fibers that support WGMs and are highly sensitive to a protein analyte is an important step toward the scalable production of affordable label-free optical biosensors. This outcome is further supported by the concomitant use of the M13 filamentous virus, a combinatorial phage display workhorse and robust, inexpensive biocapture agent.

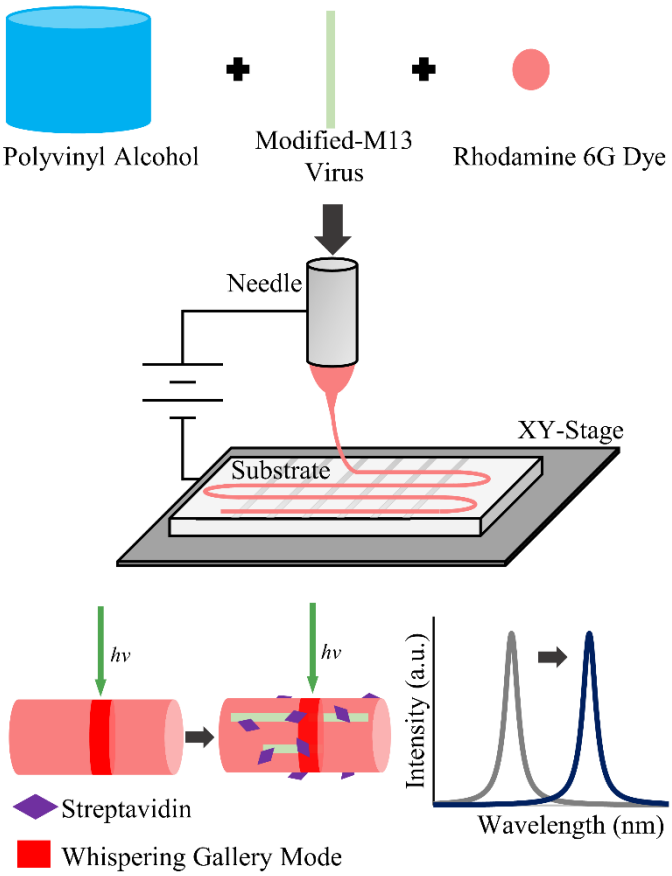

Figure 3-1: Schematic of near-field electrospinning (NFES) apparatus used to form whispering gallery mode (WGM) fiber biosensors. Polyvinyl alcohol (PVA), M13 filamentous virus bioreceptors, and rhodamine 6G (R6G) are combined in solution and electrospun under an applied voltage onto a scribed substrate to form suspended fibers. Under laser excitation, fluorescence from R6G is modulated by WGMs circulating at the fiber perimeter. The binding of a target analyte to M13 bioreceptors shifts the resonance of the WGMs.

3.2 Experimental Methods

3.2.1 Modification and amplification of M13 filamentous virus bioreceptors

Using a previously reported protocol[12,111,112], a M13 bacteriophage was genetically modified for use as a bioreceptor in electrospun WGM optical biosensors. This virus-based biorecognition element displayed a streptavidin-binding peptide motif (VPEGAFSS)[12] on the N-terminus of each major coat protein along its length. The modified phage was amplified and purified as previously described[112]. The final stock solution was suspended in 0.1X phosphate buffer saline (PBS, 13.7 mM NaCl, 0.27 mM KCl, 1 mM Na_2HPO_4, 0.18 mM KH_2PO_4) at 1 mg/ml and stored at 4°C.

3.2.2 Preparation of PVA/M13 electrospinning solutions

Polymer electrospinning solutions (27% w/w) were prepared by mixing polyvinyl alcohol (PVA, 13,000-23,000 g/mol, 98% hydrolyzed, Sigma Aldrich) and deionized water. Each solution was stirred for 2 h at 80°C until the PVA was fully dissolved. After cooling for 30 min, a volume of streptavidin-binding M13 bacteriophage suspended in 0.1X PBS was added to create a PVA/M13 solution of 25% w/w PVA and 0.1 mg/ml virus. For direct comparison, a solution of 25% w/w PVA was also made by adding 0.1X PBS alone. Prior to electrospinning, ultraviolet–visible (UV-Vis) spectroscopy (ThermoFisher, Evolution 60) was used to evaluate the turbidity of the PVA/M13 and PVA solutions. A fluorescent dye, rhodamine 6G (R6G, Sigma Aldrich), was incorporated into polymer solutions at a concentration of 0.0117 mg/ml to serve as an optical emitter for active resonant biosensors.

3.2.3 NFES and glutaraldehyde crosslinking of PVA/M13 fibers

Square glass substrates, 15 x 15 x 1 mm, with several parallel trenches scribed in them were used for near-field electrospinning (NFES). Prior to electrospinning, the substrates were sequentially immersed and sonicated (FS20 Ultrasonic Cleaner, Fisher Scientific) in acetone, isopropanol, and deionized water for 30 min to clean the surface. The substrates were then placed on a programmable X-Y stage (A-LSQ300D, Zaber). A point-plate NFES configuration (Figure 3-1) with a separation of 1.25 mm between the needle tip and substrate was used to fabricate micron-scale fibers from the prepared dye-doped PVA/M13 and PVA solutions. Each polymer solution was loaded into a syringe with an attached stainless steel 27-gauge blunt-tip needle (Fisnar). A syringe pump (NE 300 US, New Era Syringe Pump) was used to flow electrospinning solution at a rate of 10 µL/h. Electrospinning was initiated by applying a 2-kV voltage between the needle and stage. As the solution was electrospun, the computer programmed X-Y stage moved 0.5 mm/s in a parallel-line pattern to produce fibers approximately 1 cm long, spaced 200 µm apart. Fibers were written perpendicular to the trenches scribed into the glass substrate to allow them to be suspended. To prevent electrospun PVA/M13 and PVA fibers from dissolving in the aqueous sensing environment, they were crosslinked using glutaraldehyde (GA, Fisher Scientific) with hydrogen chloride (HCl) as a catalyst[74]. Fibers were placed in a closed chamber and exposed to vapor from a 50% w/w GA solution and 1 M HCl for 24 h, followed by a second vapor treatment step with 50% w/w GA solution and 5 M HCl for 24 h. In the final crosslinking step, the fibers were soaked in 50% w/w GA solution

for 24 h, rinsed with deionized water to remove excess GA, and dried in a vacuum desiccator for further use.

3.2.4 Characterization of NFES PVA/M13 fibers

Composite PVA/M13 fiber diameters were measured post-crosslinking using a digital optical microscope (KH-7700, Hirox) and associated measurement software. Fiber morphology was imaged using scanning electron microscopy (SEM; Vega3, Tescan) with an accelerating voltage of 5 kV. X-ray photoelectron spectroscopy (XPS; AXIS ULTRA^{DLD}, Kratos Analytical) was used to detect the presence of the streptavidin-binding filamentous virus bioreceptors near the fiber surface. Using an Al Kα X-ray-source, survey and high-resolution spectra were collected using pass energies of 80 and 20 eV, respectively. The functionality of the streptavidin-binding phage on the fiber surface was evaluated using streptavidin-conjugated Au nanoparticles. Streptavidin-coated Au nanoparticles (50 nm dia., Cytodiagnostics; 0.175 nM) were incubated with crosslinked PVA/M13 fibers for 3 h. The fibers were then rinsed three times with water, dried 24 h, and imaged with SEM. The areal density of bound Au nanoparticles was determined by counting the number of particles on the fiber surface and dividing by the area. The experiment was repeated three times for both PVA/M13 and PVA fibers.

Confocal fluorescence microscopy (Lecia SP5) was used to characterize the distribution of filamentous virus bioreceptors within the polymer/virus fibers. For these studies, prior to incorporation in PVA/M13 fibers, streptavidin-binding M13 bacteriophage were tagged with a fluorescent dye using an NHS-amine reactive process

(DyLight™ 550 NHS Ester, Thermo Scientific). The fibers containing M13 bacteriophage bioreceptors were imaged under 543 nm laser excitation. Dye fluorescence indicated the location of the M13 virus bioreceptors. Images were analyzed using image processing software (ImageJ). The length, width, and directionality of the M13 aggregates were measured on three fibers from three separate experiments.

3.2.5 Excitation of WGMs and real time detection of streptavidin

WGMs were excited in the PVA/M13 and PVA fibers with a far-field laser confocal system (LabRam, Horiba Scientific), as described in a previous report[74]. A 532 nm continuous wave (CW) laser (Ventus, Laser Quantum) was focused through a 50x objective (NA = 0.75), resulting in a spot size of approximately 3 μm and an incident laser power of 6 μW. The same objective was used to collect R6G fluorescence. The collected light was directed through a long pass filter (>532 nm) into a spectrometer with an 1800 lines/mm diffraction grating and a charge-coupled device (CCD) detector. A fluorescence spectrum with spectral resolution of 0.014 nm was obtained. In all experiments, the fibers were first submerged in a 1X PBS (137 mM NaCl, 2.7 mM KCl, 10 mM Na_2HPO_4, 1.8 mM KH_2PO_4) bath for at least 24 h to eliminate any signal attributable to swelling, then transferred to a fresh 1X PBS bath to obtain spectra. Emission was recorded at 3 min intervals. To prevent photothermal effects and minimize bleaching, optical devices were not illuminated with laser light between measurements.

For analysis, the broad fluorescence background was subtracted, and resonance modes were fit with Lorentzian functions to determine peak position and width.

Theoretical WGM peak positions were calculated using a Mie-theory approximation[22,23]:

$$\lambda \cong \pi n_{res} D \left[\nu + \frac{\alpha_s \nu^{\frac{1}{3}}}{2^{\frac{1}{3}}} - \frac{P}{(m^2-1)^{\frac{1}{2}}} + \frac{3}{10} \frac{{\alpha_s}^2}{2^{\frac{2}{3}} \nu^{\frac{1}{3}}} - \frac{P\left(m^2 - \frac{2P^2}{3}\right)}{(m^2-1)^{\frac{3}{2}}} \frac{\alpha_s}{2^{\frac{1}{3}} \nu^{\frac{2}{3}}} \right]^{-1} \quad (3\text{-}1)$$

where *D* is the optically measured fiber diameter, *v* is the angular mode number (*l*) plus 0.5, α_s are the roots of the Airy function, and n_{res} is the refractive index of the resonator. The term *m* is the ratio of the refractive index of the resonator to the refractive index of the surrounding medium (n_{res}/n_{host}). P is 1/*m* for TM modes and *m* for TE modes. Here, modes with the electric field vector perpendicular to the resonator surface are transverse magnetic (TM) and modes with the electric field vector parallel to the length of the fiber are transverse electric (TE). Computed solutions were compared to fluorescence spectra obtained from the electrospun fibers, and the least mean residual squared was taken as the best fit.

To assess the effectiveness of PVA/M13 electrospun fibers as label-free optical biosensors, the devices were placed in 1X PBS and allowed to equilibrate. Bovine serum albumin (BSA, 1 mg/mL) was added to the PBS solution as a blocking agent. Subsequently, the fibers were exposed to solutions of streptavidin (36, 218, 582, 1310 nM). Biosensing device response was measured for three PVA/M13 and three PVA electrospun fiber resonators. Spectra taken within 30 min of the addition of BSA, and 10

min of streptavidin addition were excluded from device analysis to avoid transients associated with surface binding.

3.3 Results and Discussion

3.3.1 Fabrication and characterization of electrospun PVA/M13 fibers

PVA fibers with incorporated M13 bacteriophage bioreceptors were fabricated using NFES. Electrospinning of water-soluble polymers such as PVA is well-suited for including large biological elements because it does not require the high temperatures, nor the harsh solvents sometimes associated with other fiber processing techniques[113,114]. In addition, the shape and form of electrospun fibers are complementary to the high aspect ratio geometry of this filamentous virus biocapture agent. By reducing the tip-to-collector distance, NFES avoids the jet instabilities and whipping associated with far-field electrospinning, resulting in a precise and controlled direct-write process. To form a composite polymer/virus solution for spinning, genetically modified M13 filamentous viruses with an affinity for streptavidin were added in low concentration (0.1 mg/mL) to an aqueous solution of moderate molecular weight PVA (13,000-23,000 g/ml). While PVA solutions were initially transparent, they became cloudy with the addition of the virus. As shown in Figure 3-2, the transmission of PVA/M13 solution was uniformly reduced throughout the entire visible range (400-900 nm), falling from 100% to 71% at 600 nm. It is important to note that the M13 bacteriophage does not absorb light at these wavelengths. The transition from optically transparent to translucent was attributed to the scattering of visible light by M13 aggregates and will be discussed later.

The polymer/virus mixture was pumped through a needle, and a droplet was generated[74]. Under an applied voltage, the droplet formed a Taylor cone, and parallel PVA/M13 fibers were deposited on a glass substrate using direct-write near-field electrospinning. Critically, the substrate was scribed with trenches prior to writing. In this way, fibers were suspended and isolated from the underlying glass, precluding optical coupling. A previously developed glutaraldehyde crosslinking process[74] was used to treat the PVA/M13 fibers and render them insoluble in aqueous solution. Glutaraldehyde formed chemical bonds between PVA polymer chains resulting in fibers that were water-stable for a minimum of 24 h[74]. As shown in Figure 3-3a, the near-field electrospinning process created a broad size distribution of PVA/M13 microfibers with an average diameter of 14.3 ± 5.3 μm. A representative SEM image of a crosslinked suspended composite polymer/virus fiber is also shown in Figure 3-3b. The surface of the suspended fibers was featureless, and no sagging was observed over scribed trenches. For comparison, using the same electrospinning conditions, microfibers were also fabricated using PVA solution without the addition of M13 bacteriophage bioreceptors (Figure 3-4). Despite the disparity in solution optical properties, no significant difference was observed in appearance or size of the PVA/M13 and PVA fibers.

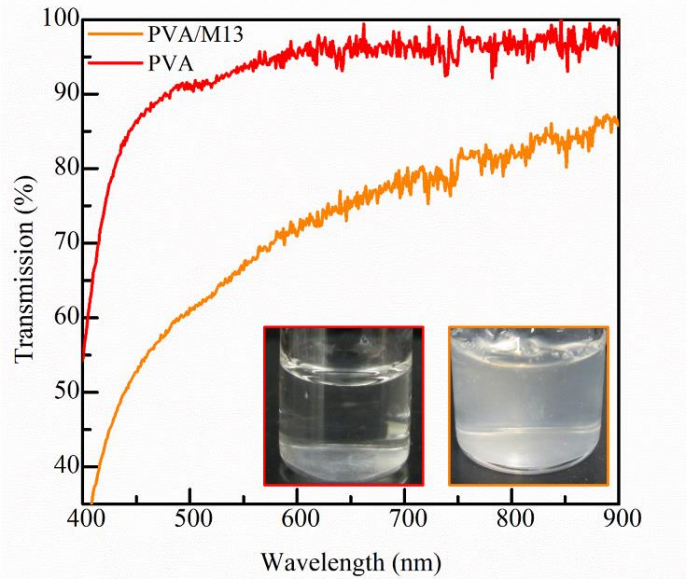

Figure 3-2: Transmission spectra of PVA/M13 and PVA electrospinning solutions. Inset: Optical images of the PVA (left) and PVA/M13 (right) solutions.

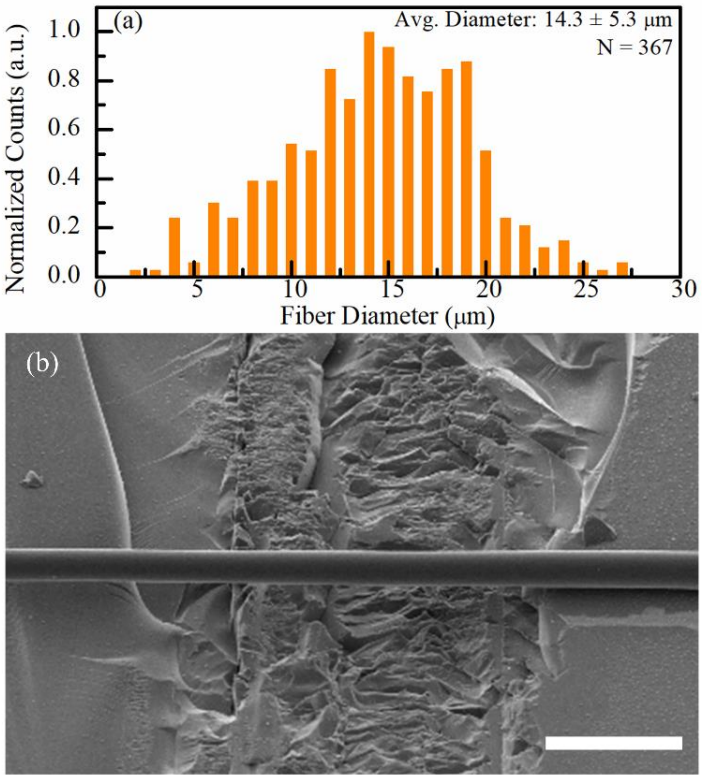

Figure 3-3: a) Histogram of PVA/M13 near-field electrospun (NFES) fiber diameter. (b) Scanning electron microscopy (SEM) image of a PVA/M13 fiber suspended over a trench that has been scribed in the underlying glass substrate. Scale bar: 50 µm

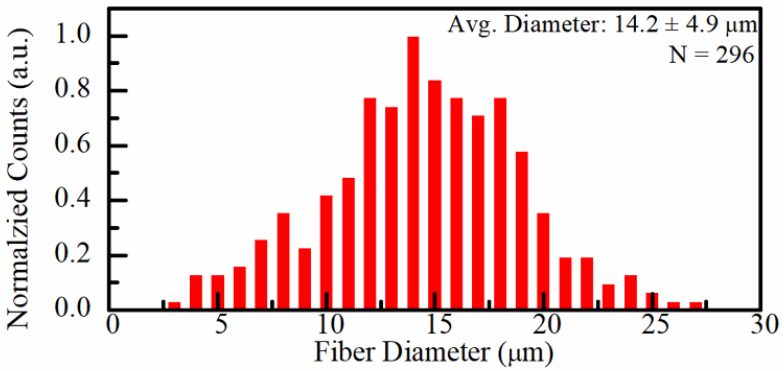

Figure 3-4: Histogram of PVA near-field electrospun (NFES) fiber diameter.

The homogeneity of phage-based bioreceptors within the near-field electrospun fibers was investigated using confocal fluorescence microscopy. This was of particular interest given the scattering of visible light observed when M13 phage was added to the PVA electrospinning solution. M13 biorecognition elements were fluorescently labeled (*i.e.*, Dylight 550) prior to mixing with PVA solution, then electrospun. A sample bright field microscopy image with overlaid confocal fluorescence emission is shown in Figure 3-5. As shown in the figure, the fluorescence of these PVA/M13 fibers was non-uniform. The tagged M13 bacteriophage formed large oblong bundles or aggregates with an average size of 5.2 x 3.2 µm. Interactions between the virus and PVA likely produced these aggregates. Based on a report by Li *et al.*, when mixed with the polymer methylcellulose, rod-like viruses such as M13 and tobacco mosaic virus (TMV) generate large assemblies[115]. The degree of ordering within these assemblies is controlled by competing mechanisms: free volume entropy and depletion volume. In concentrated polymer solutions that have not been optimized for dispersion, the drive to reduce depletion volume can cause M13 to bundle. Of course, with respect to device reliability

and repeatability, a uniform distribution of bioreceptors on the sensor surface is more desirable than randomly positioned assemblies. More studies are needed to tune attractive and repulsive forces through polymer concentration, phage concentration, and ionic strength to minimize M13 aggregation. The phage aggregates were oriented with a directionality of 1.0° with respect to the fiber axis (Figure 3-5). In contrast, phage aggregates formed in dropcast films showed no directionality (Figure 3-6). The alignment of biological materials within electrospun polymers has been previously observed for high aspect, rod-like particles including TMV, M13, and *E. coli*. [60,113,116]. The sink-like flow in the Taylor cone causes mechanical stresses that orient the biological elements[116]. With further development, it may be possible to control both the packing density and alignment of the M13. Long-range ordering and high surface coverage of bioreceptors would be an asset for electrospun fiber biosensor design.

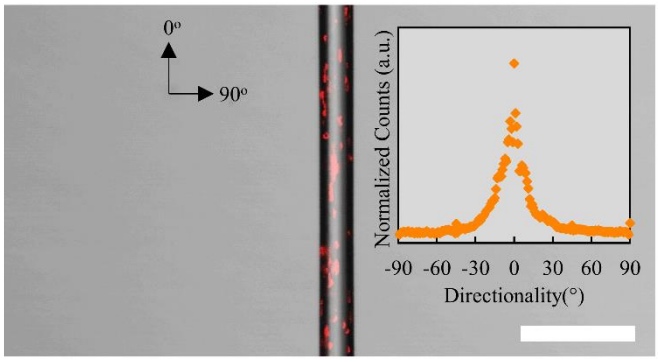

Figure 3-5: A bright field image of a PVA/M13 near-field electrospun fiber with overlaid confocal fluorescence emission. The M13 bacteriophage within the fiber have been tagged with a fluorescent dye. Inset: Phage directionality that has been measured with respect to the fiber axis. Scale bar: 50 μm

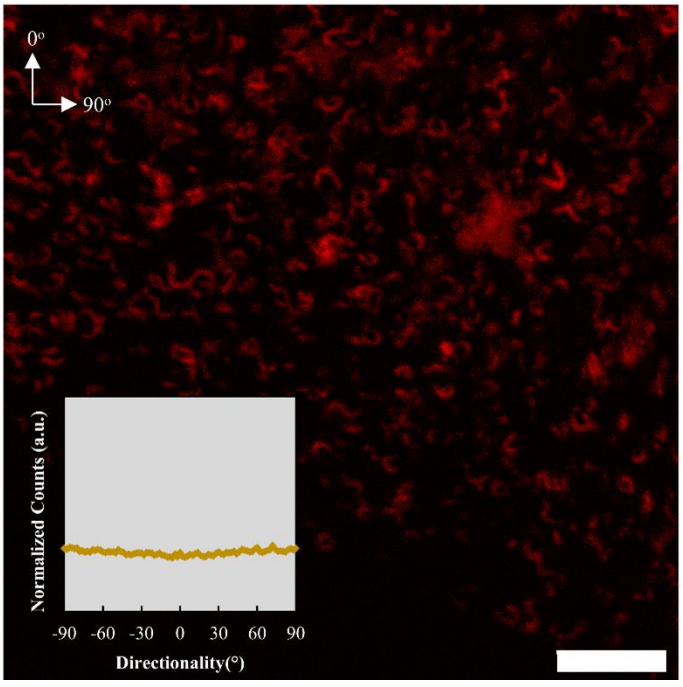

Figure 3-6: Confocal fluorescence microscopy image of a PVA/M13 dropcast film with dye-tagged M13 bacteriophage. Inset: Directionality of the M13 agglomerates with respect to the axes defined on image. Scale bar: 25 μm

For a biorecognition element to impart specificity to a sensor, it must be both accessible and functional. Only biorecognition elements on the fiber surface contribute to analyte binding and detection. The presence of bioreceptors on the surface of the composite PVA/M13 fibers was assessed using XPS. While the DNA and proteins that comprise M13 bacteriophage contain nitrogen, PVA does not. This compositional difference was exploited to identify exposed biorecognition elements. Similar strategies have been used to identify core-shell electrospun fibers, as well as the presence of proteins or polyelectrolytes on the surface of electrospun fibers[117–119].

As shown in Figure 3-7, peaks with binding energies of 400 and 404 eV were observed and attributed to nitrogen. In contrast, electrospun PVA fibers had no discernable peaks at these energies. The observation of nitrogen indicated that a measurable amount of M13 added to the electrospinning solution was located on the PVA/M13 fiber surface. Nanoparticle conjugates were used to study the streptavidin binding activity of the bioreceptors on the fiber exterior. Following crosslinking, PVA/M13 fibers were incubated with a low concentration of streptavidin-coated Au nanoparticles, thoroughly rinsed, and imaged. Electrospun PVA fibers were also prepared and imaged in the same manner.

A representative electron microscopy image of a PVA/M13 fiber with bound Au nanoparticles is shown in Figure 3-8. The surface density of Au nanoparticles was tallied for each type of fiber and displayed in Figure 3-8. The addition of streptavidin-binding phage increased the conjugated particle density by approximately 22% over PVA fibers alone. The up-tick in binding phage signaled retention of bioreceptor functionality

throughout the fiber fabrication process, including both electrospinning and crosslinking steps.

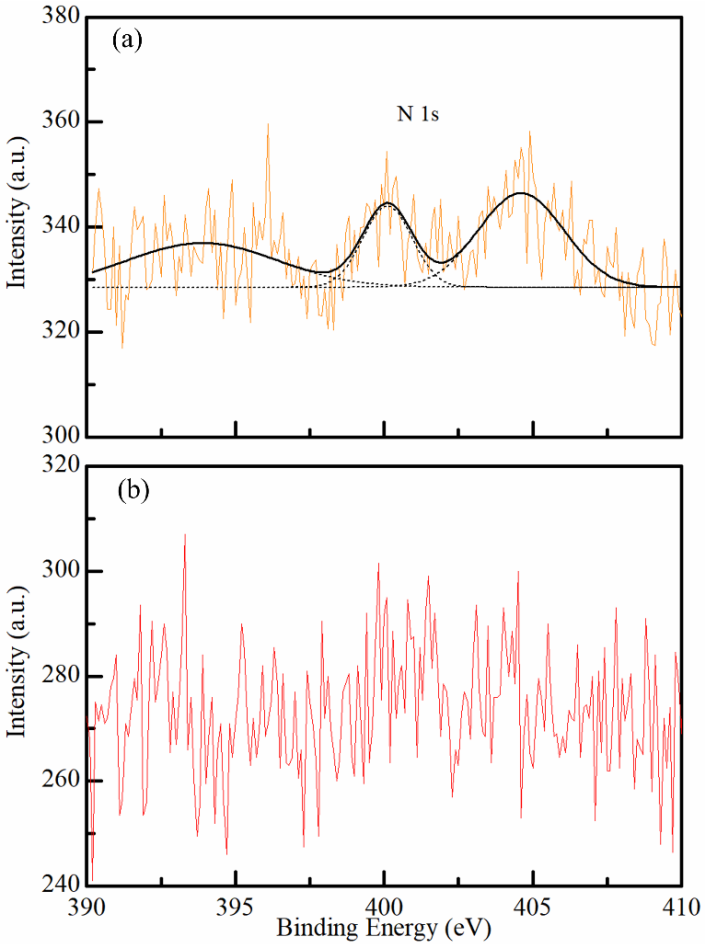

Figure 3-7: X-ray photoelectron spectroscopy (XPS) spectra of the N-region of near-field electrospun (a) PVA/M13 and (b) PVA fibers with deconvolution of the N peaks.

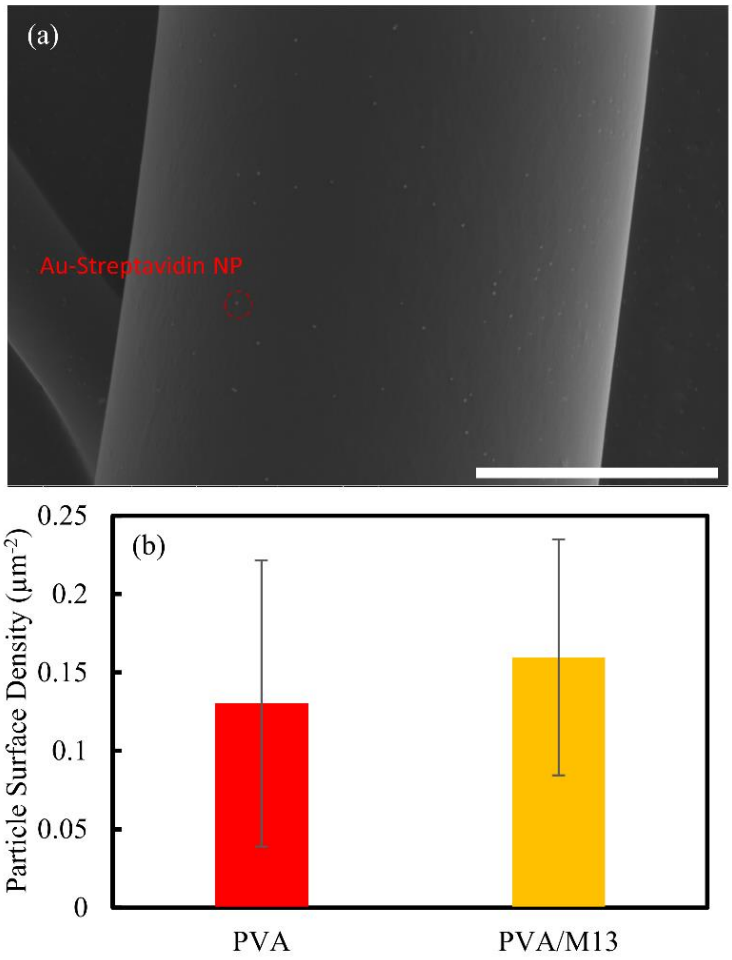

Figure 3-8*:* a) A representative SEM image of streptavidin-coated Au nanoparticles bound to the surface of a near-field electrospun PVA/M13 fiber. b) gold nanoparticle surface density after incubation with PVA and PVA/M13 fibers (N = 3). Scale bar: 5 μm

3.3.2 Excitation of WGM resonance in PVA/M13 fibers

The optical performance of the electrospun polymer/virus WGM fiber resonators was evaluated. A broad-spectrum emitter, R6G, was added to the electrospinning solution during the mixing process, transforming the fiber into an active resonator. Embedded emitters allowed the use of free-space optics for excitation and collection of WGMs. The dye-doped electrospun fiber resonators were placed in 1X PBS[19]. Because this isotonic buffer has an ionic strength and osmolarity comparable to the human body, it is commonly used in biological research, including biosensor experiments. A 532 nm continuous wave (CW) laser with 6 μW of power was focused through a microscope objective and used to excite the resonators. Emission was collected through the same objective and spectrally analyzed. In contrast to near-field optical coupling approaches such as fibers or prisms, free-space coupling spatially separates measurement optics from the analyte, preventing unwanted interactions. Furthermore, free-space optics can reduce mechanical noise because they are less susceptible to positional changes during measurement and increase portability because they are compatible with light emitting diode excitation [104,120] and on-chip microfluidic integration [121,122]. Figure 3-9a shows a representative spectrum from a dye doped, crosslinked PVA/M13 fiber with an 18.7 μm diameter, as measured optically. The broad emitter fluorescence background of the active electrospun fiber cavity was subtracted to highlight the resonant modes.

The sharp, regularly spaced peaks were ascribed to WGMs supported by the circular cross-section of the fiber and dictated by the resonance condition

$$l\lambda = \pi D n_{res} \quad (3\text{-}2)$$

where l is a positive integer indicating the angular mode number, λ is the wavelength, D is the resonator diameter, and n_{res} is the refractive index of the resonator. Resonant peaks appeared in pairs with a free spectral range (FSR) or spacing between consecutive mode pairs of 4.382 nm. Notably, each peak had a high-energy shoulder attributable to the spiral or conical modes that often develop in cylindrical WGM resonators. These modes exist due to higher-order axial modes with similar angular mode numbers that are non-degenerate due to the non-spheroidal cavity geometry[123–127]. Although the shoulder could represent a convolution of innumerable closely spaced modes, a simple two Lorentzian fit was used to analyze the asymmetric peaks as shown in Figure 3-9. As an example, a central wavelength of 598.035 nm and Q value of 2367 were found for this high-quality WGM resonance. Empirical WGM peak positions were compared to those computed using a Mie-theory derived approximation[22,23]. The observed high-quality peaks were identified as first-order radial WGMs. Mode assignments, shown in Figure 3-9, correspond to a fiber diameter of 18.4 μm and n_{res} of 1.464[74] and are consistent with previously measured values[74]. The shorter wavelength peak within a pair was a TM mode, whereas the longer wavelength peak was a TE mode. Notably, the TE modes were

consistently higher in Q and intensity. For this reason, they were selected for use in biosensing studies.

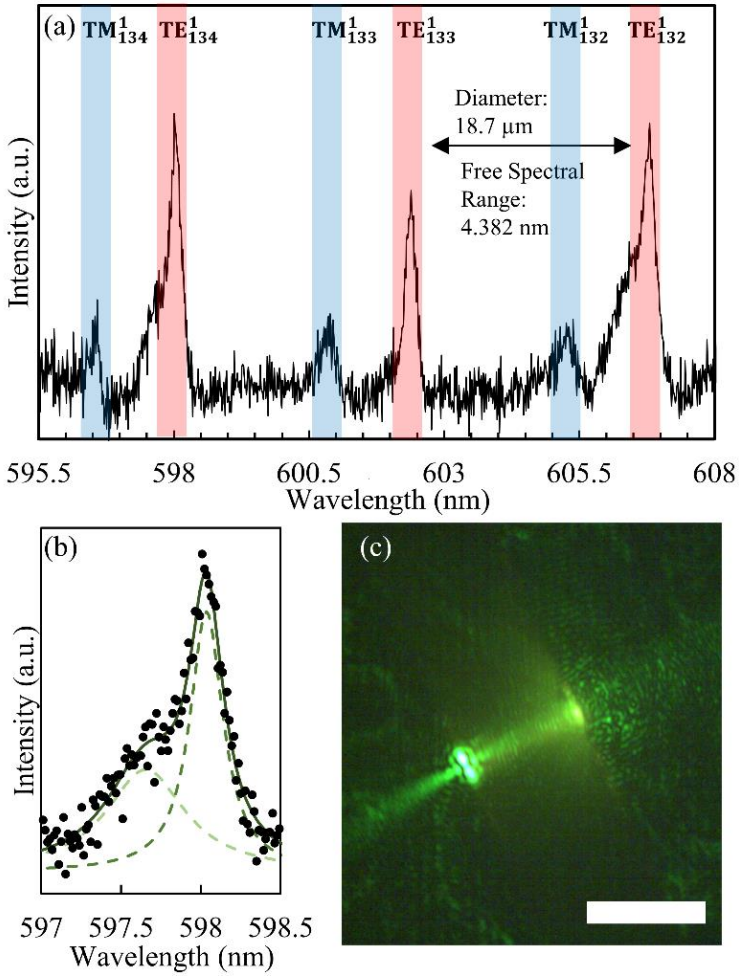

Figure 3-9: (a) Photoluminescence spectrum of an 18.7 µm diameter electrospun PVA/M13 fiber measured in PBS. The broad fluorescence background was decorated by WGMs. Mie theory was used to assign radial and angular mode numbers, as well as mode polarization. (b) An individual TE mode with a two Lorentzian curve fit. A Q-factor of 2367 was obtained for the 598.035 nm peak. (c) An optical image of a 22 µm diameter electrospun fiber WGM resonator in PBS under laser illumination. Scale bar: 20 µm

3.3.3 Label-free detection of streptavidin

Blend electrospun PVA/M13 fibers had both functional virus bioreceptors with an affinity for streptavidin on their surface and supported WGM resonances within their cross-section. These readily manufacturable, polymer-based resonators were assessed as label-free optical biosensors for streptavidin. The sensitivity of a WGM sensor is tied to the magnitude of the evanescent field at the resonator surface, and can vary with resonator size and quality [34,128]. For optical mode uniformity, polymer/virus fiber resonators with diameters between 17 and 22 μm, and Q values between 1350 and 4000 were selected for measurement. In addition, PVA fiber resonators with the same specifications were also chosen to aid in evaluation of M13 bioreceptor performance. The resonance of each fiber-based device was recorded in PBS for a minimum of 50 min prior to biosensing experiments. No trends were observed in spectral peak position during this time (Figure 3-10), thus indicating a mechanically unchanging PVA/M13 fiber and stable M13 bioreceptor surface density. Following this initial stabilization period, BSA was added to the PBS solution to limit non-specific binding contributions. BSA is regularly used as a blocking agent for a variety of biosensors and is compatible with phage-based bioreceptors and WGM optical resonators[13,14,87,129]. A spectral line shift was observed with the addition of BSA and, again, the system was allowed to achieve equilibrium (Figure 3-10). The average resonance wavelength in BSA was used as the reference point for spectral shifts associated with streptavidin binding. The spectral resolution of the system was found using the standard deviation of the resonance peak in BSA, $\sigma = 0.008$ nm.

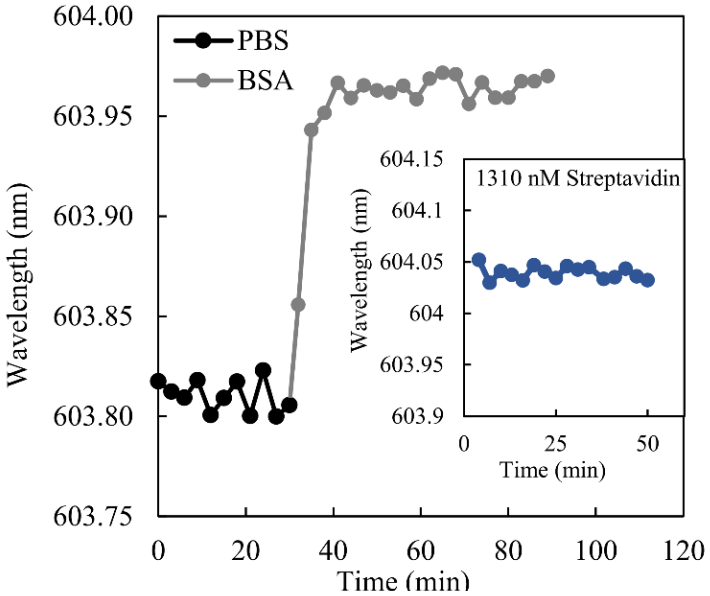

Figure 3-11: Representative resonance peak wavelength over time for PVA/M13 biosensor in PBS and BSA solutions. No trends were observed in spectral peak position during this time, thus indicating a mechanically unchanging PVA/M13 fiber and stable M13 bioreceptor surface density. Inset: Representative peak position over time after the addition of the highest concentration of streptavidin. As when the fiber resonator was immersed in PBS and BSA solutions, no trends were observed with time.

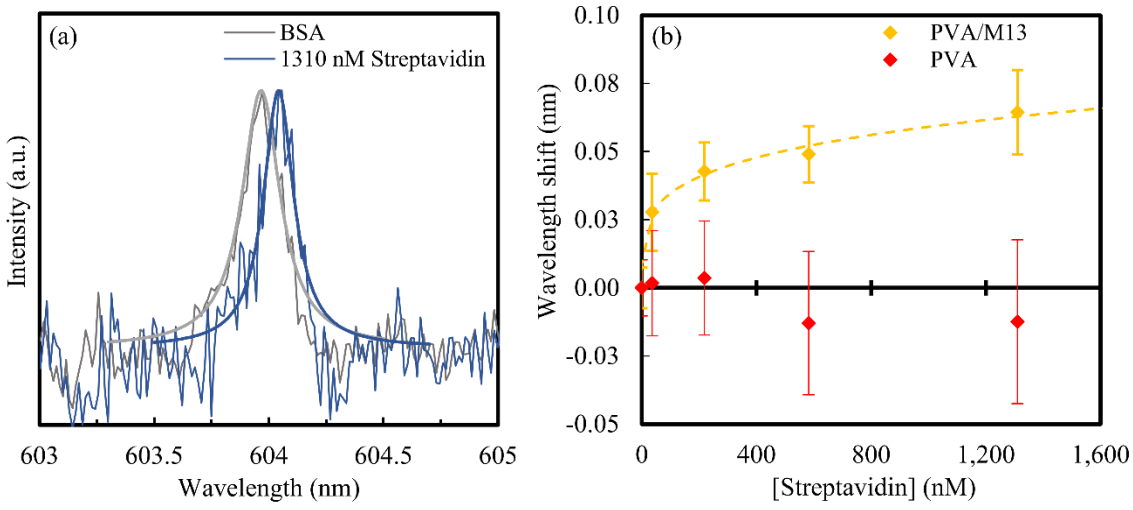

Figure 3-10: (a) A WGM resonance peak of a PVA/M13 fiber submerged in BSA solution, as well as the same mode in a 1310 nM streptavidin solution. The resonance red shifted due to the specific binding of streptavidin to the resonator surface. (b) The resonant wavelength shift compared to BSA due to the addition of a range of streptavidin concentrations. The device response was collected from three PVA/M13 and three PVA devices. The data are fitted using the Hill model (R^2 = 0.941).

The blocked electrospun fiber biosensors were exposed to streptavidin concentrations ranging from 36 to 1310 nM. A representative spectral shift observed for a PVA/M13 electrospun fiber device at the highest streptavidin concentration is shown in Figure 3-11a. With the addition of 1310 nM streptavidin, an average red-shift of 0.063 ± 0.016 nm was observed. Biomolecules, such as streptavidin, typically have a higher polarizability than the surrounding medium. Upon binding to the cavity surface, interactions with the WGM evanescent field cause an increase in resonance wavelength. Markedly, a comparable spectral shift was not observed for PVA fibers indicating that the M13 virus bioreceptors promoted streptavidin-specific binding on the cavity surface. In Figure 3-11b, the average spectral responses of the electrospun resonators are shown as a function of streptavidin concentration for both PVA/M13 and PVA electrospun WGM resonators. Differences in PVA/M13 electrospun resonator diameter and non-uniform bioreceptor distribution likely contributed to variation in spectral response. The relationship between the resonant peak of the polymer/virus fibers and streptavidin concentration was fit using the Hill model (R^2 = 0.914). The sensitivity (S) of the linear region (0 to 36 nM) was 0.008 nm/nM. The theoretical limit of detection (LoD) or the smallest resolvable response was estimated as $LoD = 3\sigma/S$ = 3 nM. For comparison, dye-doped poly-methyl methacrylate microdisk lasers and polystyrene microsphere lasers have achieved theoretical detection limits of 104 ng/ml (2 nM) for streptavidin[121] and 4 nM for neutravidin[130], respectively, using the interaction with biotin as a model high-affinity system. While these polymer-based active WGM resonators had similar limits of detection, unlike the electrospun fiber WGM biosensor, they required additional

functionalization steps following cavity formation. Notably, despite the usefulness of biotin as a model bioreceptor, biotin exhibits quite a bit of promiscuity, binding indiscriminately with the majority of avidin-like molecules. In contrast, through the combinatorial phage display process, the M13 phage-based bioreceptor has the potential to discriminate among streptavidin, avidin, and neutravidin[12] .

The surface density of streptavidin bound to composite PVA/M13 fiber biosensors can be estimated using the response of the WGM resonator. Assuming a single layer of randomly bound biomolecules and summing over the entire surface of the resonator leads to the equation[30,33]

$$\frac{\Delta\lambda}{\lambda} = \frac{\alpha_{ex}\sigma_p}{\epsilon_0(n_{res}{}^2 - n_{surr}{}^2)R} \tag{3-3}$$

Where α_{ex} is the excess polarizability of streptavidin ($4\pi\varepsilon_0 \cdot 3.85 \times 10^{-21}$) cm^3[30], R is the radius of the resonator, n_{res} is the index of refraction of the PVA fiber (1.464)[74], and n_{host} is the index of refraction of the surrounding PBS (1.3338), and σ_p is the surface density of the bound streptavidin. Assuming streptavidin is a 5 nm sphere and a square close-packed monolayer, the maximal surface density of streptavidin is 4×10^{12} streptavidin/cm^2 [131]. For the PVA/M13 devices in 1310 nM of streptavidin, we determined a surface density of $8.5 \times 10^{11} \pm 2.1 \times 10^{11}$ streptavidin/cm^2 which is equivalent to 21 ± 5% coverage of the PVA/M13 fiber surface (Figure 3-12). Assuming the streptavidin surface coverage approximately corresponds to that of the streptavidin-binding phage, the percentage of surface area covered with bioreceptors is comparable to

that observed for other M13-based optical resonator biosensors[14]. Nonetheless, the relatively low coverage indicates a possible avenue of sensor improvement. Future studies will focus on raising the sensitivity and lowering the detection limit of electrospun WGM biosensors by increasing the density and uniformity of M13 filamentous virus bioreceptors on the fiber surface.

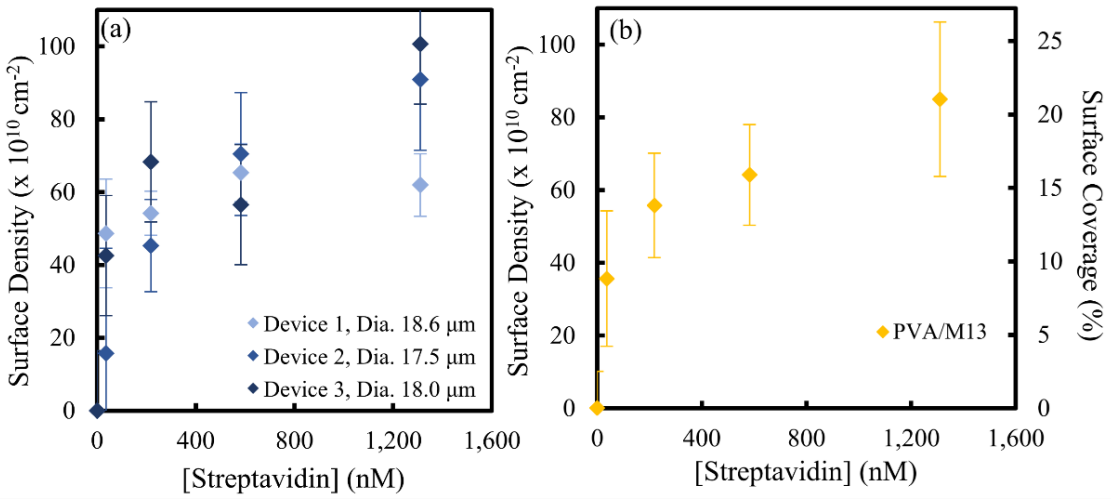

Figure 3-12: Calculated surface density and percent surface coverage of streptavidin on electrospun PVA/M13 fiber WGM resonator surfaces shown (a) for three individual devices, as well as (b) in composite.

3.4 Conclusion

Blend NFES of PVA and M13 filamentous bacteriophage is a simple strategy for immobilization of biocapture agents on WGM optical cavities. In a single step, both optical cavity formation and functionalization were achieved. Resonant wavelength shifts were tracked with the addition of a protein analyte. Specific binding of streptavidin to the resonator was observed with a sensitivity of 0.008 nm/nM and a LoD of 3 nM. Despite bioreceptor aggregation and relatively low analyte surface coverage (21%), sensor performance was comparable to reports[121,130] for other polymer-based active WGM optical biosensors that used more complex, multi-step immobilization processes and less robust biocapture agents. These results warrant further investigation of this scalable, low-cost sensing platform with emphasis on tuning bioreceptor dispersion and surface coverage. The wedding of the M13, a combinatorial phage display mainstay, with a rapid, inexpensive optical cavity manufacturing approach presents a versatile sensing platform with the potential to detect a broad range of analytes.

Chapter 4 Control of M13 distribution during electrospinning for functional applications

4.1 Introduction

The growing body of research on electrospinning polymer fibers has enabled the rapid production of nano/micro-sized fibers. Owing to the high surface-to-volume ratio and variety of biocompatible polymers, a large number of electrospun hybrid polymer/biomaterials fibers for different applications such as sensing[110,132], bio-scaffolding[133–135], drug/protein encapsulation and release[136–138] have been explored. These devices, utilize the structural and material properties of the host polymer with the bio functionality of the biological additive. These additives bind to biomolecules for biosensing applications, promote cellular growth for bio scaffolding, or slowly release drugs into the environment. Because the polymer is typically inert, the device performance generally lies with the concentration/availability of the biomaterial. For devices such as sensors or bio scaffolds, a high surface concentration of the biomaterial can be critical for device performance while for drug/protein release, control of the distribution within the fiber interior is critical.

The electrospinning approaches to fabricating polymer/biomaterial fibers can be divided into pre-processing or post-processing electrospinning[16]. For post-processing approaches, the polymer fiber is first electrospun and then the surface is functionalized with the desired biomaterial[139]. Complex, multi-step processes are typically required for immobilization to the surface.

Alternatively, pre-process electrospinning has also emerged to fabricate polymer/biomaterials. These bio composite fibers are typically fabricated through co-axial, emulsion or blend electrospinning. Blend electrospinning is the most direct method, electrospinning a polymer/biomaterial solution or mixture into a fiber. For coaxial electrospinning, two nested needles to spin two different solutions simultaneously. Various shell and core solutions can be used to fabricate a range of different core-shell fibers[140,141]. Emulsion electrospinning instead works by using two immiscible solutions during the electrospinning process[142,143]. As the solution electrospins, it phase separates, forming core-shell fibers.

In these approaches, , the concentration at a given interface is dictated by the loading of the electrospinning solution in the case or pre-processing or the amount of biomaterial able to be surface functionalized in the case of post processing . For example, Fizzel reported during emulsion electrospinning, that they were only able to achieve a maximal protein loading of 20% in their aqueous phase of 20% before electrospinning was affected[143], highlighting an upper limit of protein loading. Regardless of pre or post processing electrospinning, these methods rely on using a high concentration of biomaterial for higher loading concentration which can be cost prohibitive for biomaterials such as antibodies. Furthermore, techniques such as co-axial electrospinning, emulsion electrospinning, and surface functionalization are also more complex, requiring additional chemical or solution parameters to be optimized. An underexplored approach is to utilize the strong electric field formed during electrospinning to control biomaterial migration within the fiber. As charged and

polarizable biomaterials, DNA, proteins, and viruses can all show strong preferential migration due to a strong electric field. The dominant forces considered are either dielectrophoretic forces[144,145] or electrostatic interactions. These forces need to overcome the viscus drag that act as a resistive force. In the electrostatic interaction, charged molecules are Columbic attracted or repelled from the polymer jet surface. As the fiber solidifies, the migration can increase surface concentrations or change the biomaterial distribution within the fiber. The electrostatic interaction has been shown to control drug release dynamics [146] and induce phase separation to form core-shell fibers[147]. Additionally, the electrostatic interaction has also been shown to affect mechanical properties[148], surface energies[149], and influence crystallinity phases[150]. An unexplored application is the electrostatic migration of larger biomaterials such as viruses.

This study, examined how the electrostatic interactions influence the migration of virus surface concentration during blend electrospinning. The fibers were then assessed for whispering gallery mode biosensing. Streptavidin-binding phage was used as model biomaterial/bioreceptor. Blend near field electrospinning (NFES) with polyvinyl alcohol and M13 bioreceptor was used to fabricate polymer the whispering gallery mode cavity and functionalize the surface. Fibers were spun under four different four combinations of M13 surface charge (-, +) and polarity (-, +) as shown in Figure 4-1. The surface charge of M13 was first modified by adjusting the pH within PVA/M13 solutions. Solutions changed transmission from translucent to clear solutions with a decrease in pH. To measure the surface charge, zeta potential of M13 at different pH was measured. Based

on the zeta potential, pH 6 and pH 1.5 were chosen to represent negatively and positively charged M13. PVA/M13 at the two different pH and polarities were electrospun resulting in suspended, featureless fibers. Average fiber diameter measurements revealed a significant change in fiber diameter with pH. Fibers spun at pH 6 measured an average fiber diameter that was larger than pH 1.5. In contrast there was no significant change with polarity. Under confocal fluorescence characterization, fluorescently labeled M13 within the fibers revealed large, elongated bundles at pH 6 but smaller agglomerates at pH 1.5. The difference in agglomerate size was attributed to a change in the depletion force interaction at the different pHs. The amount of M13 migration to the fiber surface was evaluated using Au-streptavidin binding studies. A strong dependence on polarity was measured, demonstrating a strong electrostatic interaction. The results were further explained using COMSOL simulation to describe the forces acting on M13 during the electrospinning process. Using crosslinked pH 1.5 fibers, water-stable fibers were then utilized for preliminary whispering gallery mode label-free biosensing. The pH 1.5, + fibers demonstrated an increase in biosensing response compared to the opposite polarity. These results demonstrate the potential for electrostatic interactions to increase surface concentration without requiring complex multi-step functionalization or complex electrospinning setups.

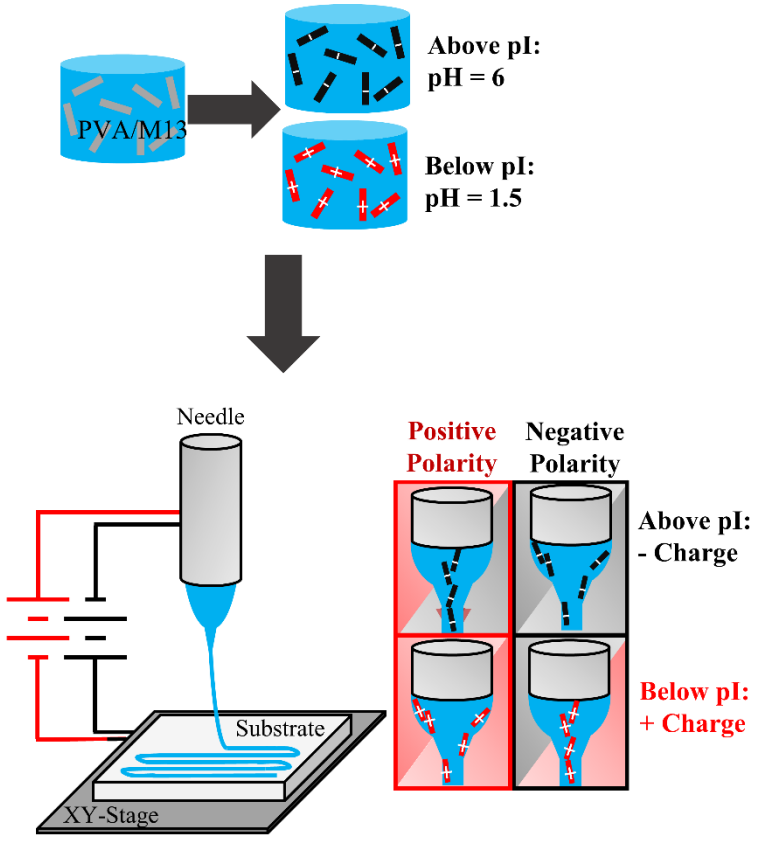

Figure 4-1: Schematic of NFES of PVA/M13 fibers. pH was chosen to correspond to negatively and positively charged phage. The different pH PVA/M13 solutions were electrospun under 2 different polarities resulting in 4 possible electrospinning parameters.

4.2 Experimental Methods

4.2.1 Modification and amplification of M13 filamentous virus bioreceptors

M13 bacteriophage was genetically modified following previous reported procedures to bind to streptavidin[12,111,112]. The pVIII protein, located along the length of the virus, was modified to display a streptavidin-binding peptide motif (VPEGAFSS)[12]near the solution facing N-terminus. Phage was amplified and purified as previously described [112] with the final phage solution suspended in 0.1X phosphate buffer saline (PBS, 13.7 mM NaCl, 0.27 mM KCl, 1 mM Na_2HPO_4, 0.18 mM KH_2PO_4) at 1 mg/ml and stored at 4°C until use.

4.2.2 *Preparation of PVA/M13 electrospinning solutions*

Electrospinning solutions were prepared by first mixing polyvinyl alcohol (PVA, 13,000-23,000 g/mol, 98% hydrolyzed, Sigma Aldrich) and deionized water at 27% w/w. The solutions were stirred for 2 h at 80°C until the PVA was fully dissolved, before the solution was allowed to cool for 30 mins. Afterward an aliquot of the M13 bacteriophages in 0.1X PBS was added to the solution to reach the desired 25% w/w PVA with 0.1 mg/ml virus loading. The solutions were allowed to stir at room temperature for another 30 min before use. 0.1X PBS was added instead of M13 aliquots as a control.

M13 and PVA/M13 solution pH were adjusted by the addition of 5M HCl under constant stirring. A pH meter was used to monitor the pH until the desired pH was obtained. Afterward, the solutions were used in electrospinning. For WGM resonance

applications, a fluorescent dye, rhodamine 6G (R6G, Sigma Aldrich), was incorporated into polymer solutions at a concentration of 0.0117 mg/ml to serve as an optical emitter.

4.2.3 NFES and glutaraldehyde crosslinking of PVA/M13 fibers

Prior to electrospinning, glass substrates (14x14x1 mm) were prepared by scribing them with parallel trenches[74]. The substrates were sequentially immersed and sonicated (FS20 Ultrasonic Cleaner, Fisher Scientific) in acetone, isopropanol, and deionized water for 30 min to clean the surface. A programmable X-Y stage (A-LSQ300D, Zaber) held the substrates while a point-plate NFES configuration with a separation of 1.25 mm between the needle tip and substrate was used to fabricate micron-scale PVA/M13 fibers. Polymer solution was loaded into a syringe with an attached stainless steel 27-gauge blunt-tip needle (Fisnar). Using a syringe pump (NE 300 US, New Era Syringe Pump), electrospinning solution flowed at a rate of 10 μL/h.

To achieve electrospun fibers from the polymer solution, a positive & negative power supplies (P03.5HA8.5/ N03.5HA8.5, Acopian Technical Company) was used.. When the positive power supply was attached to the needle, and the negative power supply was attached to the stage, this was considered the positive applied voltage or positive polarity condition. Vice versa resulted in a negative applied voltage/polarity condition. In either case, a |1.9 kV| was applied to the tip and |0.1 kV| applied to the stage to maintain the same 2.0 kV across the same tip-to-collector distance of 1250 μm. The X-Y stage was programmed to move 0.5 mm/s in a parallel-line pattern to produce fibers approximately 10 mm long, spaced 200 μm apart. Fibers were written perpendicular to

the trenches scribed into the glass substrate to allow them to be suspend and optically isolate different sections of the fibers for later whispering gallery mode measurements.

For aqueous experiments, the PVA/M13 and PVA fibers were crosslinked using glutaraldehyde (GA, Fisher Scientific) with hydrogen chloride (HCl) as a catalyst[34]. Fibers were placed in a closed chamber and exposed to vapor from a 50% w/w GA solution and 1 M HCl for 24 h, followed by a second vapor treatment step with 50% w/w GA solution and 5 M HCl for 24 h. Finally, the fibers were soaked in 50% w/w GA solution for 24 h, rinsed with deionized water to remove excess GA, and dried in a vacuum desiccator for further use.

4.2.4 Characterization of M13 and PVA/M13 solutions at different pH

Ultraviolet–visible (UV-Vis) spectroscopy (ThermoFisher, Evolution 60) was used to evaluate the transmission of the PVA/M13 and PVA solutions at different pH range using a PBS blank cuvette. For stability experiments, solutions were stored for up to 14 hours and the transmission spectra recorded at 2, 4 and 14 h intervals. Zeta potential measurements were conducted on aliquots of M13 with similar buffer and weight loading as the PVA/M13 solutions. Theoretical calculation of M13 surface charge was done using ExPASy.

4.2.5 Characterization of M13 within and on the surface of the different electrospun PVA/M13 fibers

Fiber diameters under all conditions were measured using an optical microscope setup (LabRam, Horiba Scientific) and associated camera and measurement software. Confocal

fluorescence microscopy (Lecia SP5) was also used to characterize the distribution and size of the M13 within the polymer/virus fibers. For these experiments only, the streptavidin-binding M13 bacteriophage were tagged with a fluorescent dye using an NHS-amine reactive process (DyLight™ 550 NHS Ester, Thermo Scientific) and electrospun. The fibers containing M13 bacteriophage were imaged under 543 nm laser excitation. Emitted dye fluorescence indicated the location of the M13 virus. Images were analyzed using image processing software (ImageJ). For each condition electrospun, the length, width, and directionality of the M13 aggregates was measured on 3 different fibers. The nearest neighbor distance (NND) was calculated using ImageJ, with the sample size being 3 sections of different fibers.

The amount of M13 on the fiber surface was evaluated using streptavidin-conjugated Au nanoparticles (50 nm dia., Cytodiagnostics; 0.5mg/ml). The fibers were first incubated with bovine serum albumin (BSA, 1mg/ml) solution for 30 min before rinsing ten times with water and left to dry in vacuum. Afterwards, the streptavidin-coated Au nanoparticles were incubated with the crosslinked PVA/M13 fibers for 3 h. The fibers were then rinsed ten times with water, dried 24 h, and imaged with SEM. Areal densities of bound Au nanoparticles were determined by counting the number of particles (ImageJ) and dividing by the fiber surface area. Experiments were repeated three times for all electrospun conditions.

4.2.6 Simulations of electric fields during NFES

To verify experimental results, we performed finite-element simulations of the NFES system using COMSOL Multiphysics. A 2D model was used to represent the near-field electrospinning system and polymer jet formed during electrospinning. The direction of electrostatic forces acting on M13 was calculated according to electrostatic Coulomb force ($F_{es)}$ equation:

$$F_{es} = Q * \vec{E} \quad (4\text{-}2)$$

where Q is the total particle surface charge and E is the external electric field strength. Optical measurements of droplet size and Taylor cone formation were used to simulate physical dimensions to match the NFES setup. Calculated forces were used to support the experimental results.

4.2.7 Excitation of WGMs and real time detection of streptavidin

A far-field laser confocal system (LabRam, Horiba Scientific) was used to excite WGM in R6G PVA and PVA/M13 fibers, similar to a previous report[34]. A 532 nm continuous wave (CW) laser light (Ventus, Laser Quantum) was focused using a 50x objective (NA = 0.75), resulting in a spot size of approximately 3 μm and an incident laser power of 6 μW to excite R6G inside the fibers. The emitted fluorescence was collected using the same objective and the light was directed into a spectrometer with an 1800 lines/mm diffraction grating and a charge-coupled device (CCD) detector. The resulting spectrum

had a spectral resolution of 0.014 nm. In all experiments, the fibers were soaked in 1X PBS (137 mM NaCl, 2.7 mM KCl, 10 mM Na_2HPO_4, 1.8 mM KH_2PO_4) bath for at least 24 h to eliminate any signal attributable to swelling or diffusion. Before WGM excitation or sensing, the fibers were transferred to a fresh 1X PBS bath. WGM spectra was recorded repeatedly at 3 min intervals. The sample was not illuminated between measurements to prevent photothermal effects and minimize bleaching.

To analyze the WGMs, the R6G fluorescence was subtracted, and the resonance modes were fit with Lorentzian functions to determine peak position and width. Theoretical WGM parameters and peak positions were determined using a Mie-theory approximation [37,38]:

$$\lambda \cong \pi n_{res} D \left[\nu + \frac{\alpha_s \nu^{\frac{1}{3}}}{2^{\frac{1}{3}}} - \frac{P}{(m^2-1)^{\frac{1}{2}}} + \frac{3}{10} \frac{{\alpha_s}^2}{2^{\frac{2}{3}} \nu^{\frac{1}{3}}} - \frac{P\left(m^2 - \frac{2P^2}{3}\right)}{(m^2-1)^{\frac{3}{2}}} \frac{\alpha_s}{2^{\frac{1}{3}} \nu^{\frac{2}{3}}} \right]^{-1} \quad (4\text{-}1)$$

where D is the optically measured fiber diameter, ν is the angular mode number (l) plus 0.5, α_s are the roots of the Airy function, and n_{res} is the refractive index of the resonator. The term m is the ratio of the refractive index of the resonator to the refractive index of the surrounding medium (n_{res}/n_{host}) while P is $1/m$ for transverse magnetic(TM) modes and m for transverse electric (TE) modes. TM modes are defined with electric field vector perpendicular to the resonator surface while TE modes are modes with the electric field vector parallel to fiber axis. The best computed solutions were evaluated as the least mean residual squared.

For PVA/M13 fiber experiments as WGM biosensor, the devices were placed in 1X PBS bath. A blocking agent, BSA was added to the PBS bath to reach a concentration of 1 mg/mL and the fibers were incubated for 24 hours. Fibers were then excited, and the resulting spectrum recorded for at least 1 hour. Subsequently, the fibers were exposed to streptavidin (1310 nM). The change in WGM spectra was recorded over time for at least 1 h. To calculate the immediate shift, peak positions ten mins before and after the addition of streptavidin were only considered.

4.3 Results and Discussion

4.3.1 PVA/M13 solutions at different pH

To explore how the surface charge of M13 and the polarity of the electric field during electrospinning influence the NFES process, PVA/M13 solutions with different M13 surface charges were prepared. The net charge of a protein depends on the amino acid sequence, ionizable amino acids, and solution ionic strength. For the M13 virus, the pVIII protein along the virus length is considered to dominate the surface charge due to the large number of copies (> 2700). Additionally, because some amino acids are embedded near the virus's core, typically only sections of the pVIII coat that face the outside environment are considered available. Passeratti demonstrated that theoretical zeta potential measurements of M13 could closely match empirical data by accounting for the amino acid exposure of M13 [151]. PVA/M13 and PVA solutions were prepared with an initial pH of ~ 6.0. As the pI of PVA is greater than 6.0, PVA is not expected to

change the sign of its surface charge [119,152]. The initial PVA/M13 solutions formed a cloudy solution with decreased transmission compared to pure PVA (Figure. 4-2a). The lowered transmission is attributed to the formation of M13 agglomerates which scatter light[153] as M13 does not absorb in this region. Agglomeration was previously observed and verified in chapter 3 and is attributed to a depletion force acting on M13 due to the high concentration of PVA (25% (w/w)) used in these experiments. Li observed similar agglomeration in M13/methylcellulose (MC) & tobacco mosaic virus/MC solutions [154].

As the pH decreased, solution transmission stayed constant until at pH 2.75 a sharp increase in solution transmission was observed. Afterwards, no noticeable change was observed even with further decreases in pH. Additionally, the transmission at the lower pH (<2.75) matched the transmission of a pure PVA solution, indicating no more scattering. As shown in Fig 4-2b, solutions went from 56% (pH =6) to 79% (pH = 1.6) transmission at 600 nm, comparable to the 80% transmission measured for PVA. The increase in transmission of PVA/M13 solutions is assumed to be caused by a change in the M13 agglomerates and will be verified later.

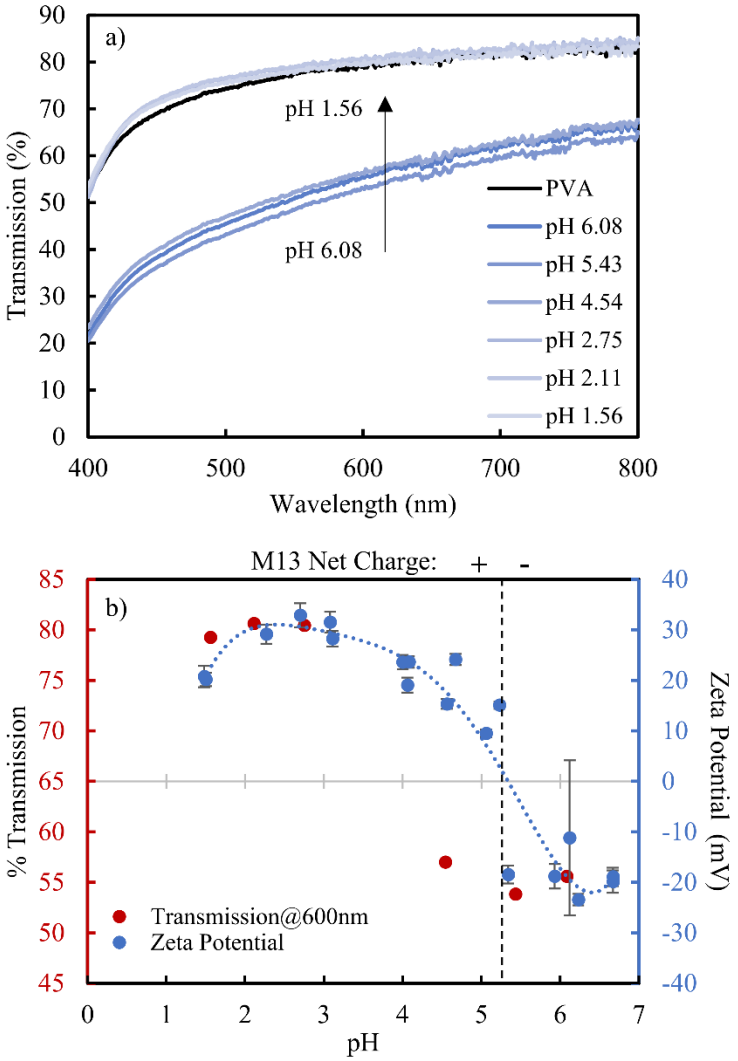

Figure 4-2: a) Optical transmission spectra of PVA/M13 electrospinning solutions for a range of pH values. A transmission spectrum of a PVA electrospinning solution without phage is shown for comparison. b) Optical transmission of PVA/M13 electrospinning solutions at 600 nm plotted with zeta potential as a function of pH. Streptavidin-binding M13 bacteriophage were dispersed in PBS for zeta potential measurements. The large decrease in PVA/M13 solution transmission corresponded to a change in M13 surface charge.

To measure the stability of the PVA/M13 solutions, UV-Vis spectrums were taken of the solutions over 14 hours (Figure 4-3a). The solutions chosen were pH 6.1 and 1.6. Regardless of the pH, the PVA/M13 solutions with positively charged M13 (pH = 1.6) and negatively charged M13 (pH = 6.1) were observed to be invariant transmission (Figure 4-3b). This indicated stable solutions suitable for electrospinning.

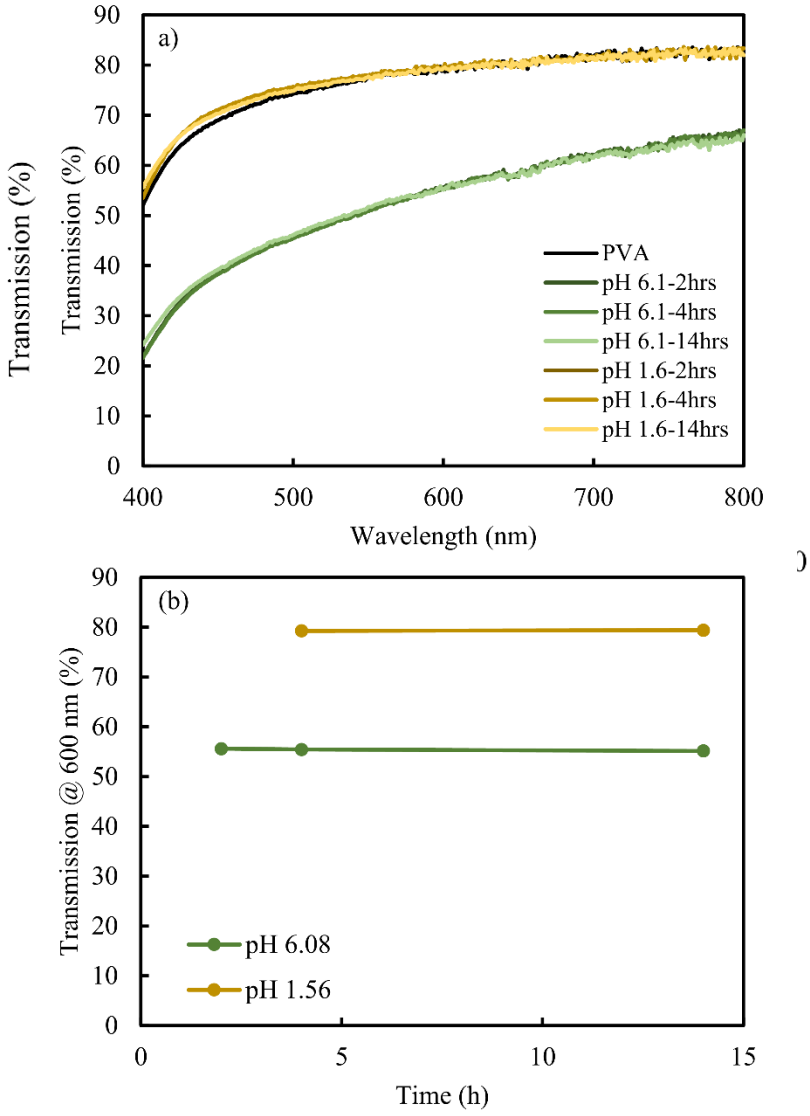

Figure 4-3: a) Optical transmission spectra of PVA/M13 electrospinning solutions for pH 6.1 and 1.6 measured up to 14 hours. b) Transmission at 600 nm plotted for 14 h

Additional M13 solutions were prepared and diluted to the same concentration as in the PVA/M13 solutions, and zeta potential measurements were made (Figure 4-2b). In all cases, the transparent solution indicated well-dispersed, non-agglomerated phage. As the pH decreased, the sign of the zeta potential when from negative to positive indicative of the pH crossing the isoelectric point (pI) of the M13. Following a report by Passaretti[151], a fifth order polynomial was used to fit the data and pI was determined to be 5.3[151], significantly different from the theoretical calculation of 4.00. It should be noted that this calculation does not consider the difference in exposure levels of individual amino acids or tyrosine residues within the pVIII coat protein. In that same report, the authors reported wildtype M13 pI = 4.05, much lower than the pI measured in this work. However, given the difference in the pVIII coat protein of wildtype M13 (A**EGD**) compared to the M13 variant used in this study (A**VPEGAFSS**), the change in pI is expected.

Interestingly the sharp change in the transmission of the PVA/M13 solutions is at a pH lower than the isoelectric point, not consistent with a change in surface charge of M13. Reasons for this discrepancy might be that the zeta potential was measured without PVA, while the transmission curves was measured with the high concentration PVA/M13 solutions. This might have lowered the zeta potential of M13, as noted by Khosrowshahi for PVA/kaolinite soi particle mixtures [155]. Additionally, the M13 agglomerates formed in the PVA/M13 solutions may possess different zeta potential curves, resulting in a different pI for M13 in PVA solutions. Another plausible reason for the transmission change could be the change in zeta potential magnitude. Across the pH range of 6.2 to

5.3, the average zeta potential across that pH range was -18.1± 4.5 mV, while at pH (4.7-4.6) the average zeta potential was 19.7±1.1 mV. Both ranges displayed low transmission curves at pH 6.1, 5.4, 4.6, respectively. In contrast, across the pH range (3.1-1.5), the average zeta potential was 27.1±1.9 mV, coincident with clear solutions at pH 2.8, 2.1, 1.6. Further comparison of the effects will be discussed later.

4.3.2 Fabrication and characterization of electrospun PVA/M13 fibers under different pH and electric field polarities

To investigate the columbic interactions from the NFES electric field and the M13 surface charge, electrospinning was done at two different electric field polarities with two differently charged M13. PVA/M13 solutions at pH=1.5 & pH = 6.0 were utilized for near-field electrospinning following previous reported PVA/M13 electrospinning procedures[153] and the polarity was changed by switching the leads on a positive and negative power supply. By changing which power supply was attached to the needle or collector, the direction of polarity could be switched. For this work, a positive terminus on the needle will be described as (pH, +) and the negative (pH,-). Shown schematically in Figure 4-1 this resulted in 4 combinations of electric field polarities and M13 surface charge electrospinning conditions, corresponding to (pH 6, -), (pH 6.0, +), (pH 1.5, -), (pH 1.5, +). Despite the difference in solution pH and electric field polarities, PVA fibers with the incorporated M13 bacteriophage were readily electrospun in all cases. As shown in Figure 4-4 ab, average fiber diameters for fiber electrospun at pH 6 were measured to be 13.1 ± 3.6 (pH 6, -) and 12.4 ± 3.7 (pH 6, +), demonstrating a small change with

polarity. For fibers electrospun at pH 1.5, average fiber diameters were measured to be 10.5 ± 3.1 (pH 1.5, -) and 10.3 ± 2.9 (pH 1.5, +), demonstrating no significant polarity affect. This is surprising as previous reports noted fiber diameter changes with polarity. Ura reported a smaller diameter for PMMA spun with positive polarity, attributing this to stronger charge build-up in the polymer jet. [148]. A similar report with PVA also demonstrated smaller fibers with positive polarity, caused by the PVA being more polarizable under positive polarities[156]. Further reports using needless spinning also demonstrated smaller fibers with positive polarity[157]. While these reports agree with pH 6 results, the lack of significant decrease in fiber diameter for pH 1.5 could be due to the large variance of fiber diameters electrospun.

With pH, however, an apparent decrease in fiber diameter was observed. From pH 6 to pH 1.5, there was a decrease 3.0-2.6 μm in average fiber diameter. Compared to other reports of PVA fiber, this was opposite of other reports of far-field electrospun PVA fibers. Son observed that 7% PVA solutions electrospun at pH =2 exhibited beaded fiber behavior[152]. Bang instead measured an increase in average fiber diameter[158] for PVA/ multi-walled carbon nanotubes. The decrease in fiber diameters may be due to an increase in solution conductivity caused by the addition of Cl^- ions from the HCl used to lower the pH[152]. This increase in salt concentration increases charge density and conductivity, which in turn increases the elongation forces from the electric field on the polymer jet. The result is an overall decrease in fiber diameter.

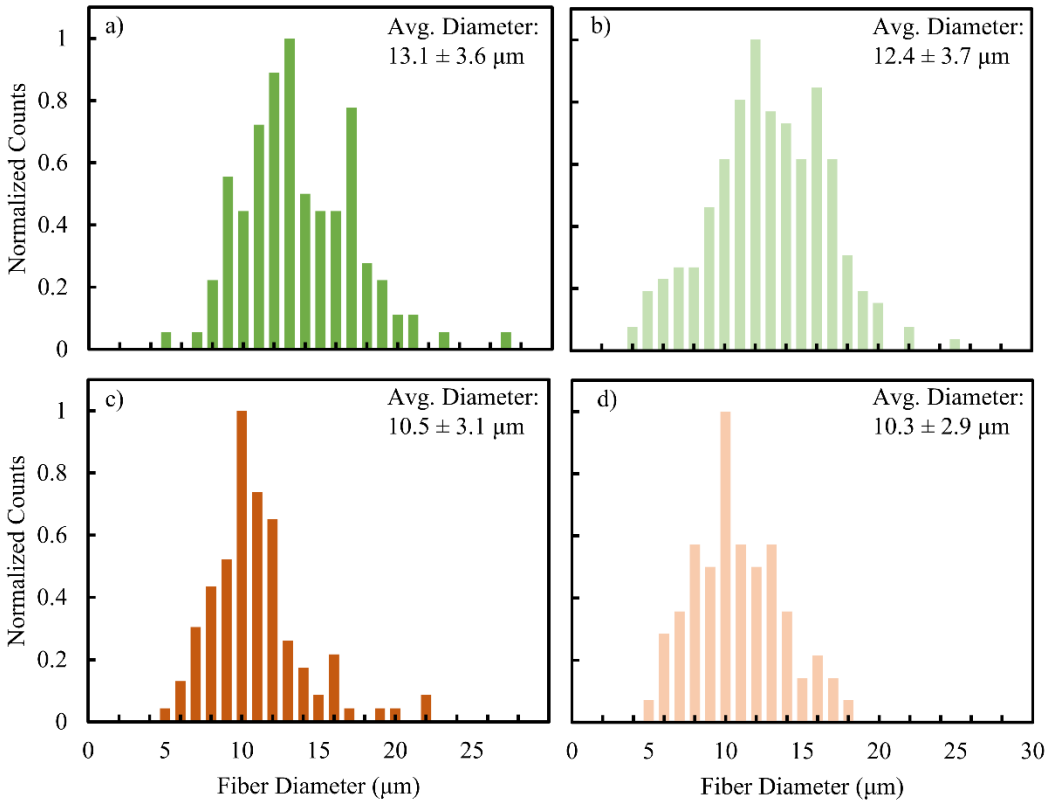

Figure 4-4: Histogram of electrospun PVA/M13 fibers electrospun at different pH & polarity conditions. a) pH 6, - b) pH 6, + c) pH 1.5, - d) pH 1.5, +. Each condition corresponds to different combination of M13 net charge and electrospinning polarity (e.g., different surface charge and applied electric field and/or same surface charge and same applied electric field)

Further studies of the M13 and M13 agglomerates within the electrospun PVA/M13 solutions were desired to correlate the UV-Vis data of the PVA/M13 solutions. The PVA/M13 fibers were characterized using confocal fluorescence microscopy and fluorescently labeled M13. A representative bright field microscopy image of the fibers overlaid with confocal fluorescence emission for (pH 6, -) and (pH 1.5, -) fibers is shown in Figure 4-5ab. The respective confocal fluorescence is shown in Figure 4-5cd. Similar representative bright field microscopy and confocal fluorescence images for pH (pH 6, +) and (pH 1.5, +) are shown in Figure 4-6 respectively. As expected from the previous report in Chapter 3[153], the fluorescence from the M13 demonstrate the M13 was aggregating. This is represented as into bright spots within the fiber, consistent with the formation of large oblong bundles or M13 agglomerates. The measured length of these agglomerates was determined to be 4.9 ± 3.1 μm (pH6, -), 4.9 ± 2.9 μm (pH 6, +) (Figure 4-5e). Regardless of the polarity applied during electrospinning, the agglomerate size showed no difference. For pH 1.5 fibers, the agglomerate length was measured to be 2.7 ± 1.4 μm (pH 1.5, -) and 3.2 ±1.4 μm (pH 1.5, -). Polarity was also shown to not affect the agglomerate length. Significant changes in agglomerate length with pH were observed between pH 6 and pH 1.5. In both cases, the agglomerate length is too long to represent an individual M13 of ~1 μm. This indicates that despite the clear solutions at pH 1.5, agglomeration is present at both pHs. The results also confirm that the transmission change observed, is due to the pH causing a change in M13 agglomerates, which in turn scatter light less.

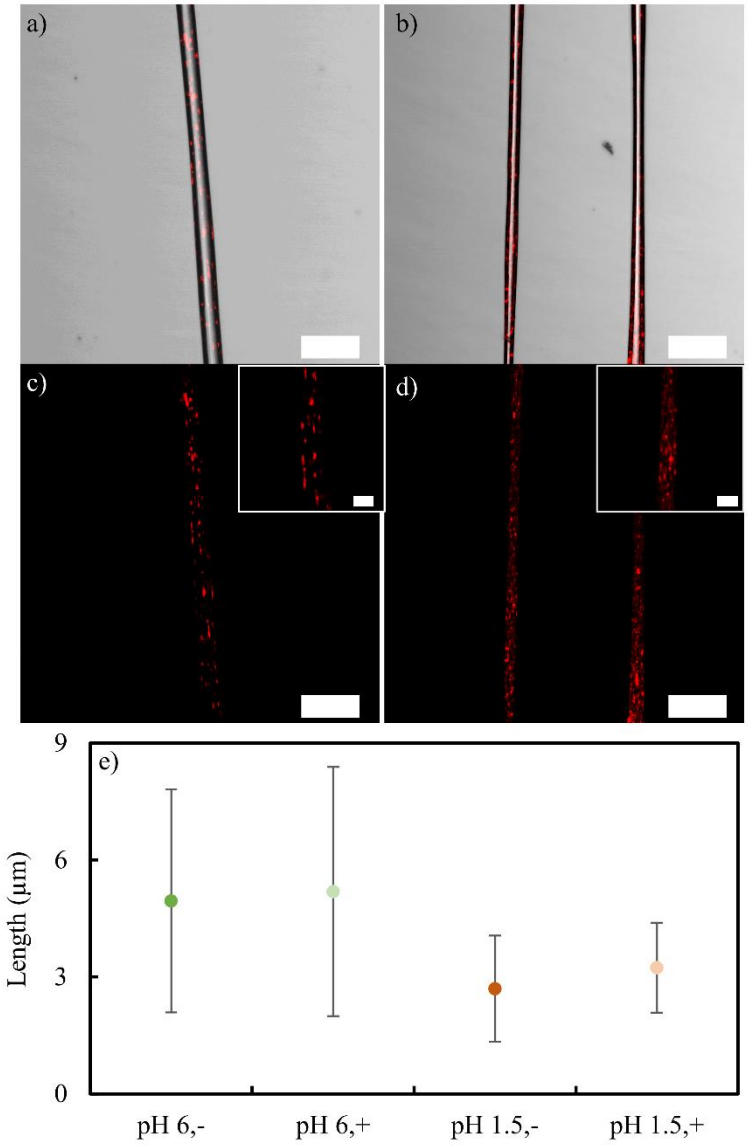

Figure 4-5: Confocal optical microscopy using dye-tagged phage to spatial characterize M13 within the electrospun fibers. Representative bright field images overlayed with the emitted fluorescence for a) pH 6, - & b) pH 1.5, -. Confocal fluorescence corresponding to M13 c) pH 6, - & d) pH 1.5, - demonstrate the presence of M13 agglomerates. e) Summary of the agglomerate length for all M13 agglomerates for pH 6, -/+ & pH 1.5, -/+. Scale bar: 50 µm, inset: 10

As mentioned previously, the driving force for M13 agglomeration in PVA is attributed to the depletion force interaction between PVA and M13. Depletion force arises from larger colloidal particles (M13 virus) and non-absorbing smaller particles (PVA). As the surface of the large particles approach each other, the smaller particles are excluded from the region between the particles[115,159]. This imbalance in polymer particle concentration creates an attractive force between the particles from the osmotic pressure. As a counterbalancing force, particles will electrostatically repel each other. Therefore, the change in agglomerate size with depletion force can be affected by the electrostatic repulsion between larger particles and changes in the osmotic pressure. Xing

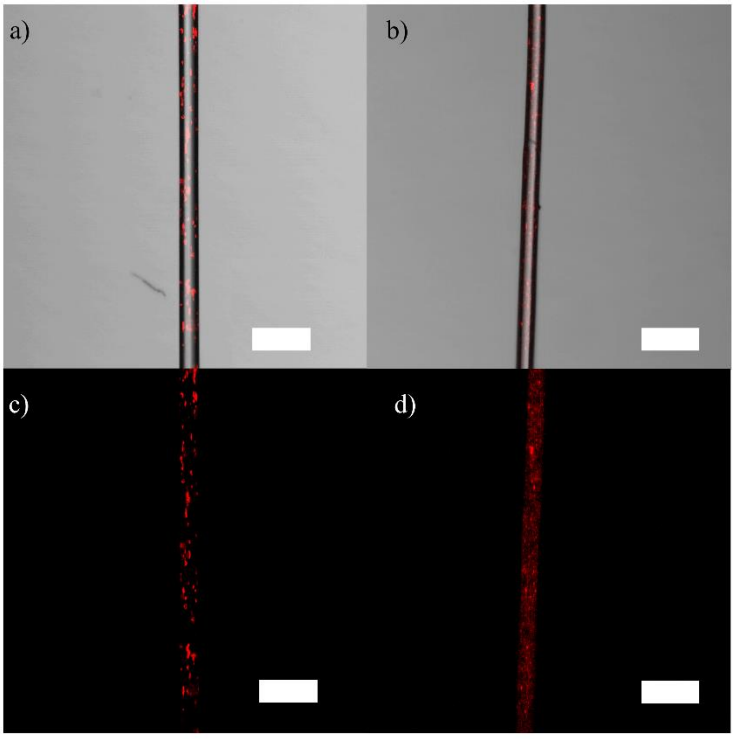

Figure 4-6: Confocal optical microscopy using dye-tagged phage to spatial characterize M13 within the electrospun fibers. Representative bright field images overlayed with the emitted fluorescence for a) pH 6, + & b) pH 1.5, +. Confocal fluorescence corresponding to M13 c) pH 6, + & d) pH 1.5, + demonstrate the presence of M13 agglomerates. Scale bar: 50 μm, confocal fluorescence contrast was increased for pH 1.5 images

previously reported a disappearance of the depletion force acting on polystyrene particles in microgel dispersion from pH 9.5 to pH 4.6[159]. They attributed this partially to a decrease in the microgel size from pH 9.5 to pH 4.6.

From the zeta potential measurements of M13, there could be two different possibilities. Firstly, the sign of the M13 changes from pH 6 and pH 1.5. As PVA is considered a neutral or slightly positively charged polymer at pH 1.5 [119,152], the shift from negative to positive M13 should increase the repulsion of PVA polymer, (due to positive-positive repulsion) or have no effect. Another possibility is the zeta potential change in magnitude at the different pH. Yadav, found that for silica nanoparticles in BSA, a change from pH 9 to pH 5 caused a decrease in the amount of BSA to cause silica nanoparticles to agglomerate[160]. This was attributed to a decrease in zeta potential from pH 9 to pH 5, which lowered the overall electrostatic repulsion between all the components. As a result, the depletion force increased, resulting in a reduced concentration of BSA required to agglomerate the silica nanoparticles. Further studies are needed to better control the depletion force interactions and fully disperse the M13 as single phage.

As shown in the confocal images (4-5cd, 4-6cd) pH 6 and pH 1.5 agglomerates also appear differently distributed. Quantification of how well-distributed agglomerates can be problematic. Different strategies have been developed such as a nearest neighbor or free space pathing[161]. For this work, a nearest neighbor distance (NND) was chosen as it was the simplest to calculate. pH 6 fibers exhibited larger spacing with pH 6, - having a NND of 5.0 ± 3.8 μm while pH 6, + had an NND of 6.3 ± 2.3 μm. In contrast, the pH 1.5

fibers demonstrated smaller NND, 2.4 ± 1.7 μm (pH 1.5, -); 2.3 ± 2.5 μm (pH 1.5, +). The difference is caused by the smaller agglomerates in pH 1.5. As the concentration of M13 remained constant for all conditions, the more well-dispersed agglomerates agree with the smaller agglomerate size. Further studies are required to fully control the depletion force to form single phages well distributed within the electrospun PVA. Nonetheless, for device reliability and repeatability, the more uniform distribution of M13 within the fiber should translate to a more uniform M13 surface concentration. As a result, the pH 1.5, - and pH 1.5, + fiber may be more suitable of PVA/M13 device applications.

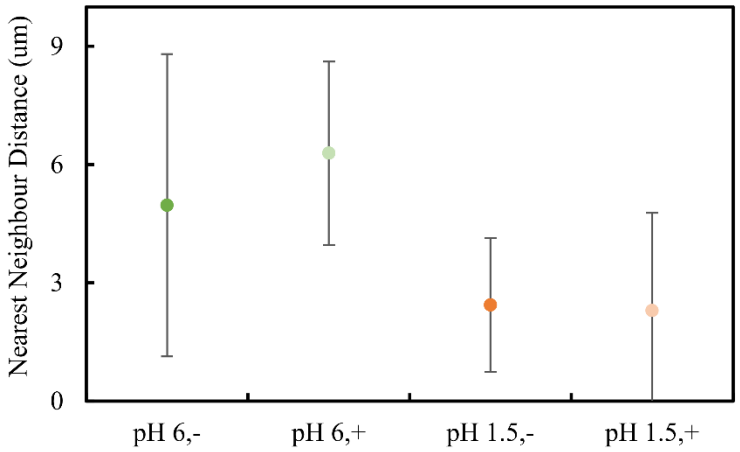

Figure 4-7: Nearest Neighbor Distance was determined using confocal fluorescence images and dye-tagged M13

Further analysis of the agglomerates was conducted using ImageJ. As shown in Figure 4-8 the agglomerates in all four sets of fibers demonstrated good directionality with respect to the fiber axis. Despite the change in agglomerate length and agglomerate distribution, both pH 6 and pH 1.5 experienced no significant difference in alignment. This is consistent with the alignment due to mechanical forces that arise from flowing polymer. This alignment has previously observed for high aspect, rod-like particles including TMV, M13, and *E. coli*. [60,113,116] and is attributed to the sink-like flow in the Taylor cone causing mechanical stresses that orient the biological elements[116].

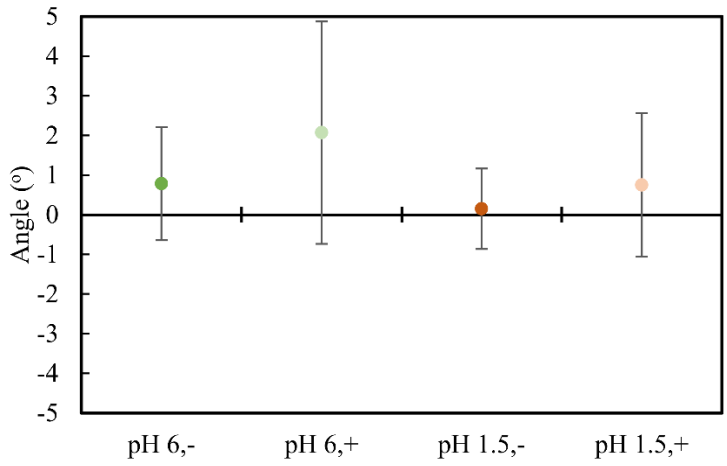

Figure 4-8: Directionality of M13 agglomerates was determined using confocal fluorescence images and dye-tagged M13.

4.3.3 Measurement of surface concentration from electrostatic interactions

The effect of M13 surface charge and electric field polarity was evaluated using SEM and streptavidin-Au NP. Due to the modified M13 affinity for streptavidin, the presence of the bound Au-streptavidin nanoparticles was utilized to evaluate the surface concentration of M13. Similar approaches have been used to assess the surface concentration of BSA for PVA/BSA electrospun fibers[119]. A representative SEM image demonstrating the number of bound nanoparticles is shown in Figure 4-9a. The

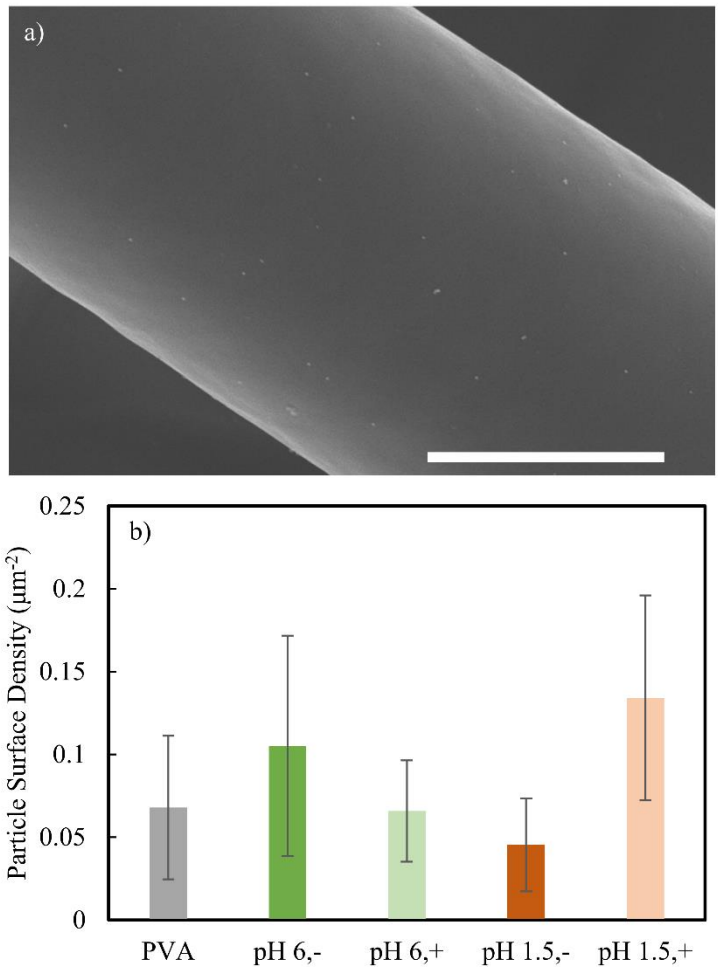

Figure 4-9: a) Representative SEM images of gold-binding to PVA/M13 surface (1.5,+.) b) Determination of bound streptavidin-Au nanoparticles to the surface of crosslinked PVA/M13 & PVA fibers. Conditions were examined were PVA, PVA/M13 (6, -); (6, +); (1.5, -); (1.5, +); Scale bar: 5 μm

average surface density of bound nanoparticles is shown in Figure 4-9b. The results demonstrate interesting trends with respect to pH and electric field polarity. At pH 6, electrospun pH 6, - were measured to have more bound nanoparticle density on the fiber surface compared to pH 6, +, indicating an increase M13 surface concentration. In contrast, pH 1.5, + exhibited higher nanoparticle binding density binding when compared to pH 1.5, - indicating the pH 1.5+ fibers had a higher M13 surface concentration. Using PVA/M13, pH 6, + the same condition as in Chapter 3, as a baseline, pH 6, - exhibited a 60% increase. Meanwhile, pH 1.5, + exhibited the largest increase of 196% while pH 1.5, - demonstrated a decrease in bound nanoparticles of 31%. While the difference in pH and M13 agglomerate size previously discussed could account for some of the difference, the electric field polarity is influencing the M13 surface concentration regardless of pH and agglomerate size. Two known forces could influence M13 migration towards the surface of the PVA fiber during electrospinning[119]. These force importantly must also be strong enough to overcome the viscus drag forces formed due to hydrodynamic friction. The first is the dielectrophoretic force, that causes biomolecules to migrate due to a non-uniform electric fields[119,145]. Within the non-uniform field, biomolecules will polarize and form a dipole. The dipole then migrates towards regions of strongest or weakest field intensity depending on the surrounding medium. Another mechanism is the electrostatic interactions between the electric field and charged biomolecule. Columbic attraction and repulsion could cause biomolecules to migrate towards or away from the surface. Tang reported an in-depth investigation of PVA and BSA electrospun systems. They electrospun BSA above and below and at the pI of BSA under positive and negative

polarity[119]. From their resulting fibers, they observed an insignificant change of BSA surface concentration with polarity and instead noticed a strong change when electrospinning at the pI. As a result, they concluded dielectrophoretic forces dominate their electrospinning. Similar results were observed with pH for wheat protein/polyethylene oxide (PEO) fibers. Using XPS they determined that PEO was preferentially drawn to the surface of the fiber away from the wheat protein's pI. This was again attributed to a dielectrophoretic force. Alternatively, Li reported an electrostatic interaction in Naproxen/Cellulose Acetate nanofibers[146]. They observed a slower/fast release of naproxen, indicating a change in the surface/interior concentration of naproxen within the cellulose acetate fibers. A similar change with polarity was also reported with PCL/chitosan nanofibers, where under negative polarity, fibers exhibited a higher migration of chitosan to the fiber surface[162]. The difference in behavior can likely be attributed to the differences in polymer charge and electrospinning setup.

From the results obtained, the change in M13 surface concentration most closely agrees with an electrostatic mechanism. Particularly for pH 1.5, the large change in M13 surface concentration cannot be explained with dielectrophoretic forces as the force depends on the polarizability of the molecule, and not on sign of the particle or electric field. Instead, the observed polarity affecting M13 surface concentration is consistent with a columbic attraction at one polarity and columbic repulsion under another. When the surface charges change from pH 6 to pH 1.5, the polarities were causing columbic attraction/repulsion switch, consistent with electrostatic interactions. The larger difference seen with pH 1.5, - & + versus pH 6, - &+ may be due to the large surface

charge of M13 at pH 1.5. With a larger charge, it is reasonable to assume the migration forces would increase, resulting in increased or decreased M13 surface concentration.

To further investigate the forces during electrospinning, COMSOL simulations of the E-field and forces experienced were carried out assuming an ideal NFES setup[163,164]. Figure 4-10a shows a simulation of the voltage under positive polarity. This corresponds to the forces experienced by M13 at pH 1.5, +. The needle at 1900V slowly changes to -100 V at the collector as expected. To determine the migration forces acting on M13, equation 4-2 was used to calculate the direction acting on the particle. To determine the direction and relative magnitude, the only relevant terms are the electric field vector and the charge of the particles. Figures 4-10b show that the forces point towards the collector at the bottom. However, at the Taylor cone and in the straight jet afterward, the forces exhibit slight changes in the x-direction force vectors towards and away from the center of the jet. Figure 4-10c plots just the x-direction force vectors associated with columbic forces. The arrowheads are proportional. Near the Taylor cone, forces migrate the particle towards the center of the fiber. As the particle travels down the length of the jet, the forces instead start to migrate the particle towards the jet surface. This migration force continues down the length of the jet until the collector. These results may explain the reason for M13 migration towards the surface, with the forces at the end of the Taylor cone and at the straight jet dominating M13 migration. Figure 4-10d plots just the x-direction forces for the same positive charged particle, electrospun under negative polarity. As expected, the sign of the forces switches directions, consistent with equation 4-2 and the results obtained for electrospinning of PVA/M13 pH 1.5, -.

While further work is needed to reach the limit of electric induced phase separation as reported by Mu[147], these results demonstrate the potential to increase electrospun surface device performance by carefully tuning the surface charge and electric field polarity.

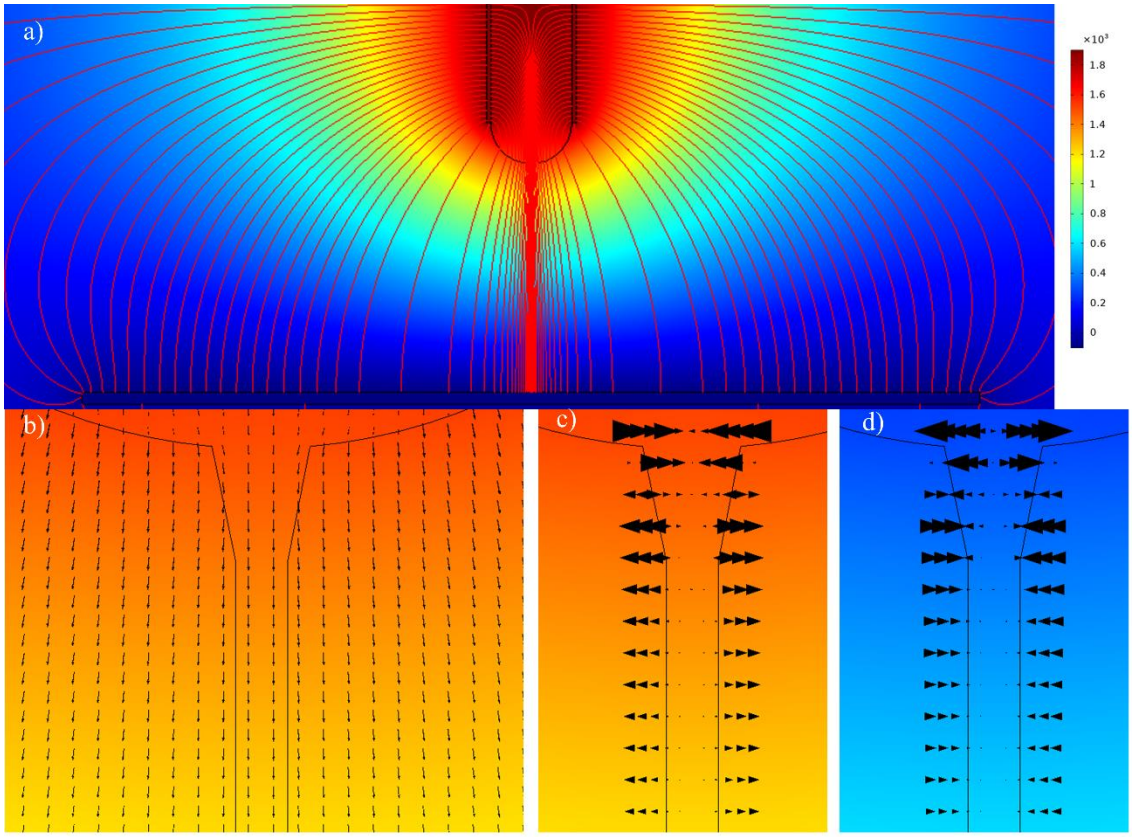

Figure 4-10: Various COMSOL simulations for NFES setup. a) simulation of the NFES setup and the electric field lines (red). Electrospinning was simulated as positive polarity as evident by the 1900V applied to the needle and -100V applied to the stage. b) zoom in at the Taylor cone during NFES, the arrows represent the columbic forces acting on a positive particle (e.g., M13 pH 1.5). c) Simplified data from simulation 4-10b where only the forces on the x-direction are plotted. Arrows represent the migration force acting on positive particle. d) Simplified data from a NFES simulation under negative polarity. Arrows represent the migration force acting on a positive particle

4.3.4 Control of M13 surface concentration for WGM biosensing

NFES PVA/M13 fibers fabricated with different M13 surface charges and electric field polarity exhibited different surface affinity to streptavidin under SEM, indicating different M13 surface concentrations. To evaluate electrospinning parameters on potential device performance, the NFES fiber were assessed for their performance as WGM label-free biosensing. pH 1.5 fibers, corresponding to positively charged M13, were utilized to the measure the difference in WGM response. Rhodamine 6G (R6G) was incorporated into the electrospinning process, and the resulting pH 1.5- and pH 1.5+ fibers were crosslinked using a previously described protocol[74,153]. A far-field excitation system was used to focus a 532 nm CW laser through an objective. Fibers were placed in a PBS bath, and the resulting R6G fluorescence was collected. A representative spectrum and fiber are shown in Figure 4-11. The resulting fluorescence demonstrated several peaks not associated with R6G fluorescence or Raman. These periodic peaks indicate WGM resonances forming within the cross-section of the PVA/M13 fibers. Interestingly, a pattern of groups of shorter wavelength peaks decorated the spectrum. These peaks are attributed to spiral or conical modes forming within the fiber[124,165,166]. Interestingly the modes are more uniform in intensity than previous observations[74]. The highest wavelength peak was analyzed for each group to simplify the analysis. It should be noted, the groups display the same TE/TM paired groups of peaks previously measured in PVA and PVA/M13 fibers[74,153], with higher intensity TE peaks. For that reason, the TE modes were the focus of this analysis. Free spectral range was measured to be 3.784 ± 0.047 nm. Using the same iterative Mie-theory

approximation approach as Chapter 3 and 4, the n_{host} was assumed to be 1.3338 corresponding to PBS. Mode assignments are shown in Figure 4-10a. The calculated radius was 21.3 μm with a resonator refractive index of 1.463, in agreement with both optical and ellipsometry measurements.

For preliminary WGM biosensing experiments, the WGM shift was measured in the presence of streptavidin. For comparable biosensor results, the PVA/M13 fibers utilized were selected to be within 18 and 20 μm in diameter, with Q values between 3000 and 5000. Both pH 1.5, + and pH 1.5, - fibers were incubated in 1mg/ml BSA for 24 hours to block nonspecific binding. BSA is a commonly used blocking agent for biosensors, with compatibility with phage-based bioreceptors and WGM optical resonators[13,14,87,129]. Prior to the addition of streptavidin, the resonance of the fiber was recorded for a minimum of 1 hour at 3-minute intervals. The resonance displayed no

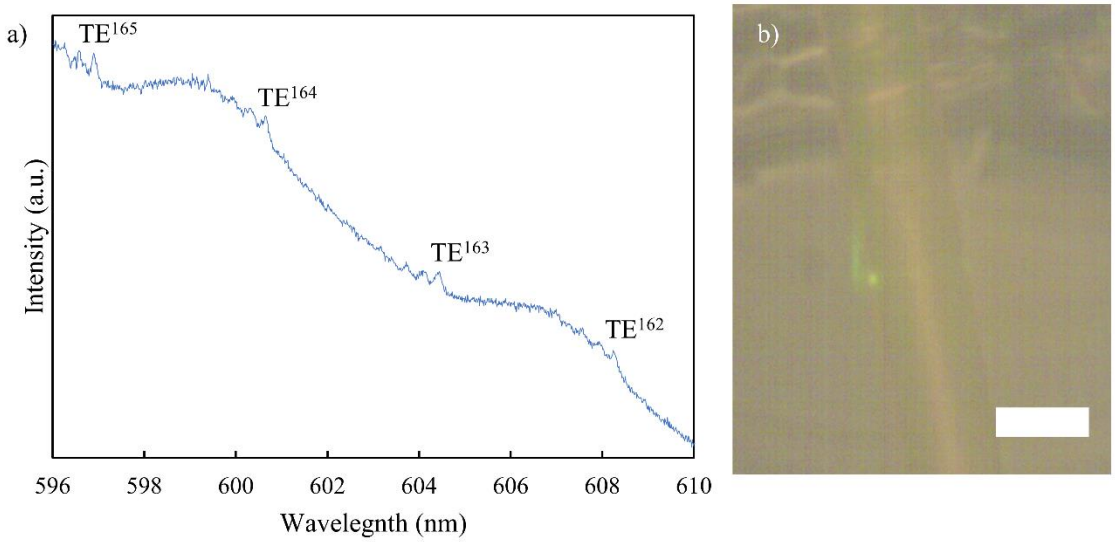

Figure 4-11: a) Representative fluorescence spectrum of a crosslinked PVA/M13 pH 1.5+ fiber in PBS. The spectrum was taken with a 50x long working distance objective under 532 nm CW illumination. b) Optical image of fiber in PBS. Measured fiber diameter was 19.8μm. Scale Bar: 20μm.

trends in the BSA/PBS bath, indicating a water-stable fiber, with no observable heating or bleaching effects. Following this initial measurement, the concentration of streptavidin was increased to 1310 nM. The increased streptavidin concentration caused a rapid redshift in peak positions (Figure 4-12a). Biomolecules typically have a higher polarizability than the buffer such as PBS. As biomolecules such as streptavidin bind to the surface, the local refractive index increases causing a red shift. Notably, the pH 1.5, + exhibited a red shift of 0.036 nm (Figure 4-12b). Compared to pH 1.5, - red shift of 0.018 nm, the increase in response is equivalent to a 106% increase in WGM shift response. The difference is consistent with the higher M13 surface concentration observed for electrospun pH 1.5, + fibers. Despite these promising results, the pH 1.5, + were observed to blue shift at extended times, ending up even more blue-shifted than the initial spectrum. While it is unclear the exact mechanism of this blue shift, it is likely due to experimental error caused by vibration jostling of the sample. Future studies will continue to focus on assessing the impact electrospinning conditions have on sensing performance by repeating the experiment at higher and lower concentrations of streptavidin. These preliminary studies demonstrate the potential to easily increase surface concentrations during blend electrospinning by considering the surface charge of the blend and polarity of the electrospinning field. This simple way of increasing surface concentration has the potential to drastically improve surface device performance in electrospun devices such as sensors[47,167], bio-scaffolds[134] or surface wettability[162].

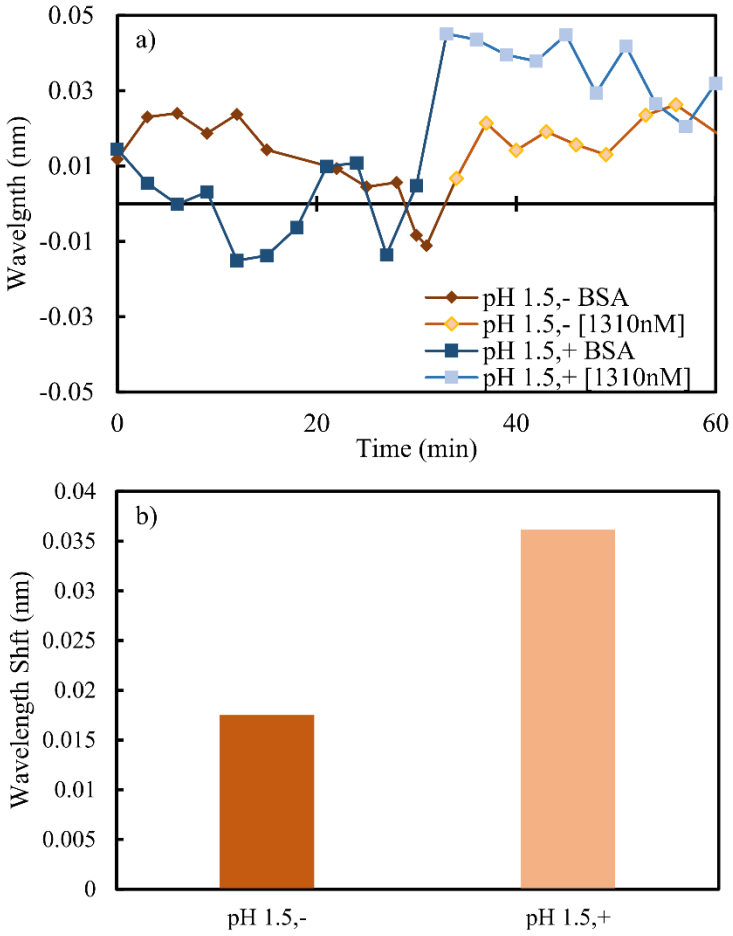

Figure 4-12: a) Representative resonance peak wavelength over time for PVA/M13 pH 1.5, - and pH 1.5, + in BSA and after addition of streptavidin solutions. b) The measured shift before and after the addition of streptavidin.

4.4 Conclusion

Electrostatic control during blend NFES of PVA/M13 filamentous bacteriophage is a simple way to fabricate enriched M13 surface fibers. Careful consideration of the surface charge and electrospinning polarity can drastically influence M13 migration. Fabricated solutions of PVA/M13 demonstrated surface enrichment consistent with electrostatics in streptavidin Au nanoparticle studies. For use as WGM biosensors, pH 1.5, + versus pH 1.5, - fibers exhibited an 106% increase in WGM response attributed to increased M13 concentrations. While preliminary, these results warrant further investigation of this simple technique to enhance device performance. Current work has focused on increasing the surface concentration of M13. However, the migration forces should work in the opposite direction, causing M13 to be more distributed near the fiber's core, useful for M13 virus release applications. These results highlight the importance of selecting complementary surface charge and polarities during electrospinning

Chapter 5 Conclusion and Future Work

5.1.Conclusion

In this dissertation, we have developed a process of near-field electrospinning (NFES) bio composite polyvinyl alcohol (PVA) / M13 filamentous virus fibers for biosensing applications. Initially, PVA fibers were electrospun over suspended trenches to optically isolate portions of the fiber. A 3-step glutaraldehyde (GA) crosslinking procedure was developed, which enabled water-stable fibers. We observed the minimal swelling under optical microscopy and dye release experiments. In submerged aqueous environments, despite the lowered refractive index contrast, the fibers were still able to support WGM resonances within the circular cross-section. Over 25 minutes, the resonances were observed to be invariant, indicating good physical stability and minimal bleaching and heating effects. These all enabled the fibers to be utilized for water-ethanol sensing experiments. Fibers were placed in pure water baths before the ethanol %(W/W) concentration was increased slowly. With each addition, the resonances red-shifted, indicating a change in the resonance condition. As crosslinked PVA is known to display hydrogel characteristics, an additional analysis using Mie-theory approximation was used to investigate the WGM parameters. The results indicated that the sensing shift was dominated by a change in the bulk refractive index. A minor <1% shrink in fiber diameter was calculated, indicating hydrogel behavior. This led to a minor blue shift compared to the large redshift measured. The PVA fibers operated mostly as bulk refractive index sensors and critically demonstrated transducing capability.

Next, PVA solutions were mixed with a genetically modified M13 virus with affinity towards streptavidin. Upon mixing, the solutions were noted to turn translucent when compared to PVA. A similar NFES process was utilized to fabricate PVA/M13 fibers. The confocal fluorescence and dye tagged M13 characterized the M13 within the fiber structures. They were noted to form into agglomerates with alignment along the fiber axis. The agglomerates were attributed to depletion force interactions while the alignment is attributed to shear forces from electrospinning flow. Despite non-uniformity in the M13 distribution within the fibers, XPS and Au-streptavidin nanoparticle (NP) binding studies demonstrated that the M13 was present on the surface and still available for binding even after GA crosslinking process. To support WGM resonances, R6G was incorporated into the fiber during electrospinning. The fluorescence of the PVA/M13/R6G fibers demonstrated distinct periodic peaks that corresponded to WGM resonances. Resonant wavelength shifts were tracked with the addition of streptavidin analyte. Specific binding of streptavidin to the PVA/M13 resonator was observed with a sensitivity of 0.008 nm/nM and a LoD of 3 nM, demonstrating M13 specificity to the targe analyte. Despite bioreceptor aggregation and relatively low analyte surface coverage (21%), the results demonstrate the potential for single step electrospun WGM biosensors.

To further enhance the M13 surface concentration of the biosensor, the electrostatic interactions with M13 during the NFES process was explored in depth. Utilizing the surface charge of M13 at different pH and the columbic attraction/repulsion associated with electric field polarities, four different PVA/M13 electrospinning

conditions were explored. PVA/M13 solutions at pH 6 (surface charge: negative) and pH 1.5 (surface charge: positive) were first characterized. Initial solutions were translucent that turned transparent as the pH changed, indicating a change in M13 agglomerate size. Under different polarities, electrospun fibers displayed no significant fiber diameter trends. However, the pH 1.5 fibers were notably smaller. Using confocal fluorescence and dye tagged M13, the agglomerates within the pH 1.5 fibers were confirmed to be significantly smaller and more well dispersed. Utilizing Au-streptavidin NP binding studies, both pH 6 and pH 1.5 fibers demonstrated an electrostatic preferential migration of M13 towards the surface. pH 6, - fibers bound more Au-streptavidin NP. When the surface charge was reversed, pH 1.5, + fiber bound more Au-streptavidin NP, consistent with electrostatics. To support WGM resonances, R6G was again incorporated into the pH 1.5 electrospinning process. Both polarities of pH 1.5 fibers demonstrated fluorescence with distinct, periodic peaks that correspond to WGM resonances. The modes were utilized for preliminary biosensing of streptavidin. pH 1.5, + versus pH 1.5, - exhibited an 106% increase in WGM peak shift, attributed to increased M13 surface concentration binding to streptavidin.

These results demonstrate the potential for electrospun WGM polymer fiber sensors as a scalable, low-cost sensing platform. The wedding of the M13, a combinatorial phage display mainstay, with a rapid, inexpensive optical cavity manufacturing approach, provides a versatile optical sensing platform with the potential to detect a broad range of analytes.

5.2.Future Work

5.2.1 Influence of M13 migration on WGM biosensing

As shown in Section 4.3.4, pH 1.5, -/+ fibers demonstrated a difference in WGM response to streptavidin. Despite the poor stability of the signal, the promising preliminary results indicate the increase in M13 surface concentration led to an increase in streptavidin binding, which in turn lead to an increase in WGM peak shift. For a more definitive quantification on device reliability and sensitivity, further studies with more device and with higher and lower concentrations of streptavidin.

5.2.2 Hydrogel WGM Biosensors

Throughout this dissertation, the focus on WGM sensing and biosensing has been on the interaction of the evanescent wave with analyte bound to the fiber surface. However, as only a portion of the electromagnetic field is contained inside the evanescent wave, a large portion of the resonance within the cavity is not utilized. Depending on the surrounding environment and the evanescent wave might only contain 4.0% of the WGM field for a silica sphere in water[33]. While decreasing the size of the resonator will lower the Q-factor and increase the evanescence wave fraction thus increasing sensitivity, the lowered Q-factor will increase the peak noise. Similarly, an increase in size will increase Q-factor but reduce sensitivity[168]. One approach to deal with the trade-off between Q-factor and sensitivity is to utilize the electromagnetic field within the resonator instead, referred to as the guide mode. This can be accomplished by diffusing the analyte into the resonator. The approach has two advantages: the electromagnetic field within the

resonator can now interact with the analyte, and the bioreceptor can bind to the analyte in the 3D volume within the resonator rather than the 2D surface, increasing analyte loading.

Some initial work was done to understand the theoretical amount of the electromagnetic field in a WGM resonator. To understand the electromagnetic field (E-field) inside and outside the resonator, it is common to calculate the E-field through the use of the boundary condition of the WGM resonance[20,169]:

$$\frac{[n_{host}kRh_l(n_{host}kR)]'}{h_l(n_{host}kR)} = N\frac{[n_{res}kRj_l(n_{res}kR)]'}{j_l(n_{res}kR)} \quad (5\text{-}1)$$

where n_{res} and n_{host} are the refractive index of the resonator and the host medium, $k = 2\pi/\lambda$ where λ is the resonance wavelength. j_l and h_l are the spherical Bessel and Hankel functions of the first kind. N = 1(TE) or $(n_{host}/n_{res})^2$ (TM). R is the resonator radius. Open-source MATLAB code from Balac[169] was modified to calculate the boundary conditions and the WGM and in 3D spherical coordinates. The code was modified to incorporate the n_{host} as well as using a spherical Hankel function instead of the more common Neumann function approximation implemented. An example of a 10 μm radius resonator with n_{res} = 1.5 and n_{host} =1.3 is shown in Figure 5-1a.

Another approach has been to describe the evanescent wave as an exponential decay with decay length (r_{ev}):

$$r_{ev} = \frac{1}{k\sqrt{{n_{res}}^2 - {n_{host}}^2}} \quad (5\text{-}2)$$

A volume integral approach has also been used to derive the fraction of the guided mode and evanescent wave for the TE WGM modes[33].

$$f = \frac{\lambda}{\pi R} \frac{{n_{host}}^2}{{n_{res}}^2 - {n_{host}}^2} \quad (5\text{-}3)$$

Notably, this volume integration assumes $r_{ev} << R$. The guided mode E-field was calculated with a Riemann sum of the 1D electric field described in Figure 5-1a and the volume integration of equation 5-3. A comparison is shown in Figure 5-1b. The Riemann sum method calculated a smaller percentage of the guided mode E-field inside the resonator. This difference arises from the boundary condition method relying on a Hankel function to describe the evanescent wave while the volume integral relies on assumptions of exponential decay and decay length.

Assuming that the theoretical increase in sensitivity is equivalent to the total amount of E-field versus the evanescent wave E-field:

$$\Delta S = \frac{E_{total}}{E_{evanscent}} \quad (5\text{-}3)$$

calculated increases in sensitivity are shown in Figure 5-1c. As expected, with more E-field within the resonator, the volume integral method predicts a larger increase in sensitivity.

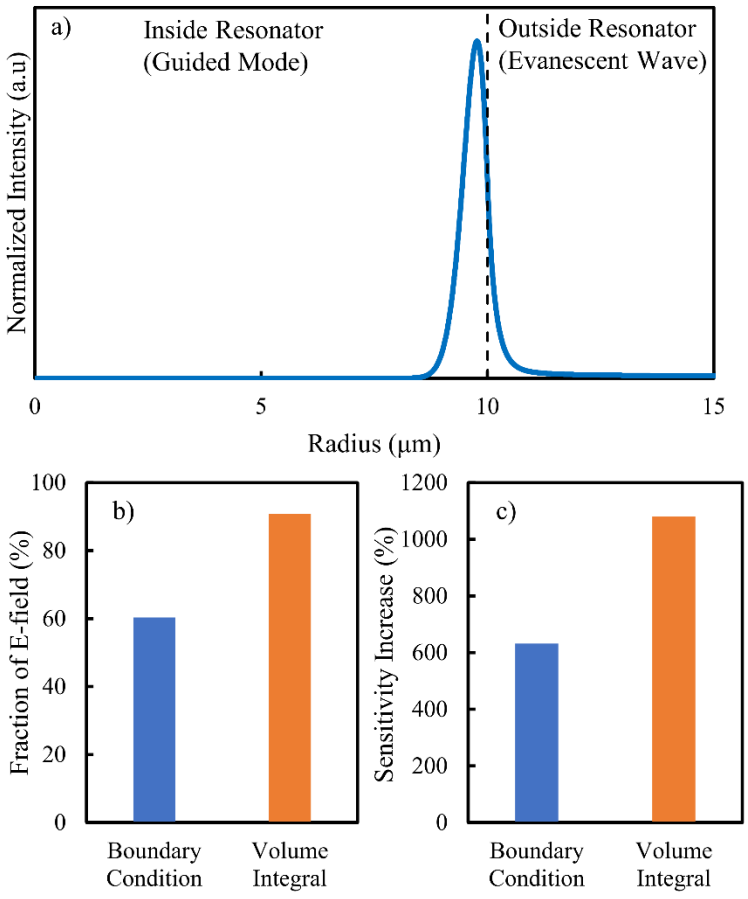

Figure 5-1: Electric field along the radius of the resonator derived from equation 5-1. b) fraction of E-field within the resonator c) Increase in sensitivity due to diffusion of analyte. Resonator radius = 10μm, n_{res} = 1.5, n_{host} = 1.3

To account for the discrepancy between the 2 different calculations, a comparison between the Hankel function and exponential decay model is shown in Figure 5-2 using 3 different conditions. The condition most like the PVA electrospun fibers in aqueous environments (and used in Figure 5-1) is shown in Figure 5-2a, where the radius of the resonator was assumed to be 10 μm, n_{res} = 1.5 and n_{host} = 1.3, coinciding with polymer and aqueous environment index of refractions. There is a significant difference in the decay behavior between the Hankel and exponential function. While the exponential decays close to zero within < 1 μm of the resonator surface, the Hankel function is still decaying. When the radius of the resonator is increased to 50 μm (Figure 5-2b), the differences become negligible, and a short decay (<1 μm) is noted in both cases. Finally, Figure 5-2c shows the calculations when the radius = 10 μm, n_{res} = 1.5 and n_{host} = 1.0

representing the resonator in air. While a difference in decay behavior is observed, in both calculations, the decay is again within < 1 μm. As shown in these results, the

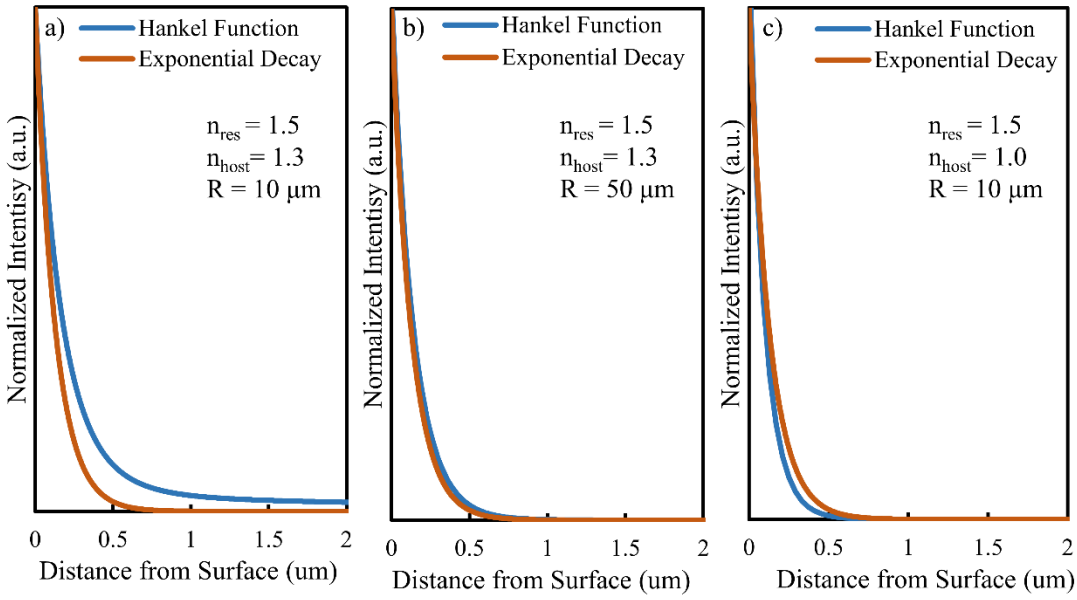

Figure 5-2: Calculated Hankel Functions and Exponential Decay of a WGM resonator using equations 5-1 and 5-2. The parameters used for a) n_{res} = 1.5, n_{host} = 1.3, R =10 μm b) n_{res} = 1.5, n_{host} = 1.3, R =50 μm, c) n_{res} = 1.5, n_{host} = 1.0, R =10 μm,

exponential decay is a good approximation for larger sized or larger refractive index contrast (n_{res} - n_{host}) environments. However, as the size of the resonator decreases and the refractive index contrast decreases (lower Q resonators), the approximations introduce errors. Similar observations were made by Himmelhaus regarding perturbation theory with 10 μm polystyrene spheres[19]. These calculations highlight an important theoretical problem when using smaller-sized WGM resonators in low refractive index contrast environments (e.g., water, aqueous buffer etc.), indicating issues with commonly used WGM equations. Going forward, new theoretical models may be needed to describe WGM sensing with diffusion with smaller, low Q resonators.

To achieve guided mode WGM sensing, approaches using liquid droplets, hydrogel layer spun on silica or oxide resonators, or pure hydrogel have been utilized. In liquid droplets resonators, WGM are excited within a droplet. Sensing is achieve by adding the analyte to the droplet[20,170]. However, the lack of a solid resonator can be impractical for real-world applications. A growing body of work has instead utilized hydrogel-based WGM resonators to utilize the electromagnetic field within the resonator. The analyte can diffuse into the solid hydrogel network. One approach has been to coat silica or oxide WGM resonator with a hydrogel layer. Examples include agarose onto a silica resonator[171] or poly(acrylic acid)/poly(ethylenimine)(PAA/PEI) on an oxide resonator[82]. It should be noted that these applications are focused on solvent vapor[83] or humidity sensing[172], where the stability of the hydrogel is not as important. However, aqueous hydrogel WGM sensing has yet to been reported. This unexplored approach has the potential to drastically increase biosensing sensitivity.

, Preliminary studies as described in Chapter 2 demonstrated that PVA fibers under different GA crosslinking conditions exhibit different swelling characteristics. It has been well documented that swelling behavior is linked to the mesh size, which in turn is related to the degree of crosslinking[62,66]. By tailoring the GA crosslinking degree, the mesh size of the PVA fibers can be controlled. An added benefit of controlling the mesh size is that biomolecule diffusion into the PVA hydrogel could also be controlled [173–175]. Preventing larger than the target biomolecule from diffusing could improve specificity by only allowing a select size of biomolecules to interact with the bioreceptor. Initial conditions to be explored are changing the concentration of HCl catalyst (1-6 M),

GA concentration (25%-75%), and the time spent crosslinking. Additionally, other crosslinking agents could be explored[61]. The M13 migration effect shown in Chapter 4 could also be used to migrate M13 towards the region of the strongest electromagnetic field, increasing the detection of binding events. Future studies of the diffusion capacity of PVA could be measured by fluorescently tagging analytes such as streptavidin and measuring the diffusion coefficient with confocal fluorescence microscopy. The impact of different mesh size PVA hydrogel fibers and its impact on the sensitivity WGM biosensor could be determined through biosensing experiments.

References

1. Bhalla, N.; Jolly, P.; Formisano, N.; Estrela, P. Introduction to biosensors. *Essays Biochem.* **2016**, *60*, 1–8, doi:10.1042/EBC20150001.

2. Kim, E.; Baaske, M.D.; Vollmer, F. Towards next-generation label-free biosensors: recent advances in whispering gallery mode sensors. *Lab Chip* **2017**, *17*, 1190–1205, doi:10.1039/c6lc01595f.

3. Chen, C.; Wang, J. Optical biosensors: An exhaustive and comprehensive review. *Analyst* **2020**, *145*, 1605–1628, doi:10.1039/c9an01998g.

4. Karoonuthaisiri, N.; Charlermroj, R.; Morton, M.J.; Oplatowska-Stachowiak, M.; Grant, I.R.; Elliott, C.T. Development of a M13 bacteriophage-based SPR detection using Salmonella as a case study. *Sensors Actuators, B Chem.* **2014**, *190*, 214–220, doi:10.1016/j.snb.2013.08.068.

5. Olyaee, S.; Bahabady, A.M. Design and optimization of diamond-shaped biosensor using photonic crystal nano-ring resonator. *Optik (Stuttg).* **2015**, *126*, 2560–2564, doi:10.1016/j.ijleo.2015.06.037.

6. Dantham, V.R.; Holler, S.; Barbre, C.; Keng, D.; Kolchenko, V.; Arnold, S. Label-free detection of single protein using a nanoplasmonic-photonic hybrid microcavity. *Nano Lett.* **2013**, *13*, 3347–3351, doi:10.1021/nl401633y.

7. Su, J. Label-Free biological and chemical sensing using whispering gallery mode optical resonators: Past, present, and future. *Sensors (Switzerland)* **2017**, *17*, 1–18, doi:10.3390/s17030540.

8. Groff, K.; Brown, J.; Clippinger, A.J. Modern affinity reagents: Recombinant antibodies and aptamers. *Biotechnol. Adv.* **2015**, *33*, 1787–1798, doi:10.1016/j.biotechadv.2015.10.004.

9. Bazin, I.; Tria, S.A.; Hayat, A.; Marty, J.L. New biorecognition molecules in biosensors for the detection of toxins. *Biosens. Bioelectron.* **2017**, *87*, 285–298, doi:10.1016/j.bios.2016.06.083.

10. Machera, S.J.; Niedziółka-Jönsson, J.; Szot-Karpińska, K. Phage-based sensors in medicine: A review. *Chemosensors* **2020**, *8*, doi:10.3390/CHEMOSENSORS8030061.

11. Han, L.; Liu, P.; Petrenko, V.A.; Liu, A.H. A label-free electrochemical impedance cytosensor based on specific peptide-fused phage selected from landscape phage library. *Sci. Rep.* **2016**, *6*, 1–10, doi:10.1038/srep22199.

12. Petrenko, V.A.; Smith, G.P. Phages from landscape libraries as substitute antibodies. *Protein Eng. Des. Sel.* **2000**, *13*, 589–592, doi:10.1093/protein/13.8.589.

13. Nanduri, V.; Balasubramanian, S.; Sista, S.; Vodyanoy, V.J.; Simonian, A.L. Highly sensitive phage-based biosensor for the detection of β-galactosidase. *Anal. Chim. Acta* **2007**, *589*, 166–172, doi:10.1016/j.aca.2007.02.071.

14. Zhu, H.; White, I.M.; Suter, J.D.; Fan, X. Phage-based label-free biomolecule detection in an opto-fluidic ring resonator. *Biosens. Bioelectron.* **2008**, *24*, 461–466, doi:10.1016/j.bios.2008.04.028.

15. Zourob, M. *Recognition receptors in biosensors*; 2010; ISBN 9781441909183.

16. Zhang, M.; Zhao, X.; Zhang, G.; Wei, G.; Su, Z. Electrospinning design of functional nanostructures for biosensor applications. *J. Mater. Chem. B* **2017**, *5*, 1699–1711, doi:10.1039/c6tb03121h.

17. Aliheidari, N.; Aliahmad, N.; Agarwal, M.; Dalir, H. Electrospun nanofibers for label-free sensor applications. *Sensors (Switzerland)* **2019**, *19*, doi:10.3390/s19163587.

18. He, X.X.; Zheng, J.; Yu, G.F.; You, M.H.; Yu, M.; Ning, X.; Long, Y.Z. Near-Field Electrospinning: Progress and Applications. *J. Phys. Chem. C* **2017**, *121*, 8663–8678, doi:10.1021/acs.jpcc.6b12783.

19. Himmelhaus, M.; Krishnamoorthy, S.; Francois, A. Optical sensors based on whispering gallery modes in fluorescent microbeads: Response to specific interactions. *Sensors* **2010**, *10*, 6257–6274, doi:10.3390/s100606257.

20. Foreman, M.R.; Avino, S.; Zullo, R.; Loock, H.P.; Vollmer, F.; Gagliardi, G. Enhanced nanoparticle detection with liquid droplet resonators. *Eur. Phys. J. Spec. Top.* **2014**, *223*, 1971–1988, doi:10.1140/epjst/e2014-02240-9.

21. Foreman, M.R.; Swaim, J.D.; Vollmer, F. Whispering gallery mode sensors. *Adv. Opt. Photonics* **2015**, *7*, 168, doi:10.1364/AOP.7.000168.

22. Lam, C.C.; Leung, P.T.; Young, K. Explicit asymptotic formulas for the positions, widths, and strengths of resonances in Mie scattering. *J. Opt. Soc. Am. B* **1992**, *9*, 1585, doi:10.1364/josab.9.001585.

23. Khozeymeh, F.; Razaghi, M. Cylindrical optical resonators: Fundamental properties and bio-sensing characteristics. *J. Opt. (United Kingdom)* **2018**, *20*, doi:10.1088/2040-8986/aab052.

24. Peng, B.; Yang, L.; Jiang, X.; Cocking, A.; Huang, S.H.; Özdemir, Ş.K.; Janisch, C.; Liu, Z. Surface-enhanced Raman scattering on dielectric microspheres with whispering gallery mode resonance. *Photonics Res.* **2018**, *6*, 346, doi:10.1364/prj.6.000346.

25. Lu, J.; Xu, C.; Li, F.; Yang, Z.; Peng, Y.; Li, X.; Que, M.; Pan, C.; Wang, Z.L. Piezoelectric Effect Tuning on ZnO Microwire Whispering-Gallery Mode Lasing. *ACS Nano* **2018**, *12*, 11899–11906, doi:10.1021/acsnano.8b06500.

26. Wang, H.; Liao, M.; Xiao, H.; Zhang, Z.; Yang, J.; Yang, J.; Tian, Y. All-Optical Tunable Whispering Gallery Modes in a Polymer Bottle Micro-Resonator. *IEEE Photonics Technol. Lett.* **2021**, *33*, 97–100, doi:10.1109/LPT.2020.3045466.

27. Lee, A.; Mills, T.; Xu, Y. Nanoscale welding aerosol sensing based on whispering gallery modes in a cylindrical silica resonator. *Opt. Express* **2015**, *23*, 7351, doi:10.1364/oe.23.007351.

28. Li, Y.; Zhang, H.; Liu, B.; Lin, W.; Yan, D.; Yang, C.; Wu, J. Laser-tuned whispering gallery modes in a silica-based microsphere resonator integrated with ethyl-orange-doped polyvinyl alcohol coating. *Sensors Actuators, B Chem.* **2017**, *238*, 98–104, doi:10.1016/j.snb.2016.07.044.

29. Weller, A.; Liu, F.C.; Dahint, R.; Himmelhaus, M. Whispering gallery mode biosensors in the low-Q limit. *Appl. Phys. B Lasers Opt.* **2008**, *90*, 561–567, doi:10.1007/s00340-007-2893-2.

30. Arnold, S.; Khoshsima, M.; Teraoka, I.; Holler, S.; Vollmer, F. Shift of whispering-gallery modes in microspheres by protein adsorption. *Opt. Lett.* **2003**, *28*, 272, doi:10.1364/ol.28.000272.

31. Armani, A.M.; Kulkarni, R.P.; Fraser, S.E.; Flagan, R.C.; Vahala, K.J. Label-free, single-molecule detection with optical microcavities. *Science (80-.).* **2007**, *317*, 783–787, doi:10.1126/science.1145002.

32. Kang, Y.Q.; François, A.; Riesen, N.; Monro, T.M. Mode-Splitting for Refractive Index Sensing in Fluorescent Whispering Gallery Mode Microspheres with Broken Symmetry. **2018**, 1–9, doi:10.3390/s18092987.

33. Gagliardi, G.; Loock, H.P. *Cavity-Enhanced Spectroscopy and Sensing*; 2014; Vol. 179; ISBN 9783642400025.

34. Reynolds, T.; Henderson, M.R.; François, A.; Riesen, N.; Hall, J.M.M.; Afshar, S. V.; Nicholls, S.J.; Monro, T.M. Optimization of whispering gallery resonator design for biosensing applications. *Opt. Express* **2015**, *23*, 17067, doi:10.1364/oe.23.017067.

35. Su, J.; Goldberg, A.F.G.; Stoltz, B.M. Label-free detection of single nanoparticles and biological molecules using microtoroid optical resonators. *Light Sci. Appl.* **2016**, *5*, 2–7, doi:10.1038/lsa.2016.1.

36. Cai, L.; Pan, J.; Hu, S. Overview of the coupling methods used in whispering gallery mode resonator systems for sensing. *Opt. Lasers Eng.* **2020**, *127*, doi:10.1016/j.optlaseng.2019.105968.

37. Riesen, N.; Reynolds, T.; François, A.; Henderson, M.R.; Monro, T.M. Q-factor limits for far-field detection of whispering gallery modes in active microspheres. *Opt. Express* **2015**, *23*, 28896, doi:10.1364/oe.23.028896.

38. Kim, I.; Moon, J.S.; Oh, J.W. Recent advances in M13 bacteriophage-based optical sensing applications. *Nano Converg.* **2016**, *3*, doi:10.1186/s40580-016-0087-5.

39. Warner, C.M.; Barker, N.; Lee, S.W.; Perkins, E.J. M13 bacteriophage production for large-scale applications. *Bioprocess Biosyst. Eng.* **2014**, *37*, 2067–2072, doi:10.1007/s00449-014-1184-7.

40. Horikawa, S.; Bedi, D.; Li, S.; Shen, W.; Huang, S.; Chen, I.H.; Chai, Y.; Auad, M.L.; Bozack, M.J.; Barbaree, J.M.; et al. Effects of surface functionalization on the surface phage coverage and the subsequent performance of phage-immobilized magnetoelastic biosensors. *Biosens. Bioelectron.* **2011**, *26*, 2361–2367, doi:10.1016/j.bios.2010.10.012.

41. Ogata, A.F.; Edgar, J.M.; Majumdar, S.; Briggs, J.S.; Patterson, S. V.; Tan, M.X.; Kudlacek, S.T.; Schneider, C.A.; Weiss, G.A.; Penner, R.M. Virus-enabled biosensor for human serum albumin. *Anal. Chem.* **2017**, *89*, 1373–1381, doi:10.1021/acs.analchem.6b04840.

42. Bhardwaj, N.; Kundu, S.C. Electrospinning: A fascinating fiber fabrication technique. *Biotechnol. Adv.* **2010**, *28*, 325–347, doi:10.1016/j.biotechadv.2010.01.004.

43. Haider, A.; Haider, S.; Kang, I.K. A comprehensive review summarizing the effect of electrospinning parameters and potential applications of nanofibers in biomedical and biotechnology. *Arab. J. Chem.* **2015**, doi:10.1016/j.arabjc.2015.11.015.

44. Liu, Y.; Hao, M.; Chen, Z.; Liu, L.; Liu, Y.; Yang, W.; Ramakrishna, S. A review on recent advances in application of electrospun nanofiber materials as biosensors. *Curr. Opin. Biomed. Eng.* **2020**, *13*, 174–189, doi:10.1016/j.cobme.2020.02.001.

45. Krämmer, S.; Laye, F.; Friedrich, F.; Vannahme, C.; Smith, C.L.C.; Mendes, A.C.;

Chronakis, I.S.; Lahann, J.; Kristensen, A.; Kalt, H. Electrospun Polymer Fiber Lasers for Applications in Vapor Sensing. *Adv. Opt. Mater.* **2017**, *5*, 1–19, doi:10.1002/adom.201700248.

46. Shehata, N.; Samir, E.; Gaballah, S.; Hamed, A.; Elrasheedy, A. Embedded Ceria Nanoparticles in Crosslinked PVA Electrospun Nanofibers as Optical Sensors for Radicals. *Sensors* **2016**, *16*, 1371, doi:10.3390/s16091371.

47. Ponce-Alcántara, S.; Martín-Sánchez, D.; Pérez-Márquez, A.; Maudes, J.; Murillo, N.; García-Rupérez, J. Optical sensors based on polymeric nanofibers layers created by electrospinning. *Opt. Mater. Express* **2018**, *8*, 3163, doi:10.1364/ome.8.003163.

48. Ta, V.D.; Chen, R.; Sun, H. Controllable Polarization of Lasing Emission From a Polymer Microfiber Laser. *Sci. Rep.* **2019**, *9*, 1–6, doi:10.1038/s41598-019-53437-2.

49. Chen, X.; Xie, K.; Hu, T.; Zhang, X.; Yang, Y.; Ma, J.; Zhang, J.; Cheng, X.; Hu, Z. Whispering gallery mode microlaser based on a single polymer fiber fabricated by electrospinning. *J. Phys. D. Appl. Phys.* **2019**, *52*, 475104, doi:10.1088/1361-6463/ab39f1.

50. Di Camillo, D.; Fasano, V.; Ruggieri, F.; Santucci, S.; Lozzi, L.; Camposeo, A.; Pisignano, D. Near-field electrospinning of light-emitting conjugated polymer nanofibers. *Nanoscale* **2013**, *5*, 11637–11642, doi:10.1039/c3nr03094f.

51. Bisht, G.S.; Canton, G.; Mirsepassi, A.; Kulinsky, L.; Oh, S.; Dunn-Rankin, D.; Madou, M.J. Controlled continuous patterning of polymeric nanofibers on three-dimensional substrates using low-voltage near-field electrospinning. *Nano Lett.* **2011**, *11*, 1831–1837, doi:10.1021/nl2006164.

52. Islam, A.; Yasin, T.; Gull, N.; Khan, S.M.; Sabir, A.; Munawwar, M.A.; Shafiq, M.; Jamil, T.; Raza, M.H. Fabrication and performance characteristics of tough hydrogel scaffolds based on biocompatible polymers. *Int. J. Biol. Macromol.* **2016**, *92*, 1–10, doi:10.1016/j.ijbiomac.2016.07.010.

53. Yan, F.; Chen, H.; Zheng, L.; Chen, W.; Liu, Y.; Hu, Q. The controllable PVA-chitosan fiber prepared by the near-field electro spinning for tissue engineering. *Adv. J. Food Sci. Technol.* **2013**, *5*, 1073–1078, doi:10.19026/ajfst.5.3208.

54. Haberer, E.D.; Sharma, R.; Meier, C.; Stonas, A.R.; Nakamura, S.; Denbaars, S.P.; Hu, E.L. Free-standing, optically pumped, GaN/InGaN microdisk lasers fabricated by photoelectrochemical etching. *Appl. Phys. Lett.* **2004**, *85*, 5179–5181, doi:10.1063/1.1829167.

55. Cheeney, J.E. Whispering Gallery Mode Polymer Fiber Sensors Fabricated by Near-Field Electrospinning 2018.

56. Afzal, H.M.; Mitu, S.S.I.; Al-Harthi, M.A. Microwave radiations effect on electrical and mechanical properties of poly (vinyl alcohol) and PVA/graphene nanocomposites. *Surfaces and Interfaces* **2018**, *13*, 65–78, doi:10.1016/j.surfin.2018.07.006.

57. Koosha, M.; Aalipour, H.; Shirazi, M.J.S.; Jebali, A.; Chi, H.; Hamedi, S.; Wang, N.; Li, T.; Moravvej, H. Physically crosslinked chitosan/pva hydrogels containing honey and allantoin with long-term biocompatibility for skin wound repair: An in vitro and in vivo study. *J. Funct. Biomater.* **2021**, *12*, doi:10.3390/jfb12040061.

58. Kenawy, E.R.; Kamoun, E.A.; Mohy Eldin, M.S.; El-Meligy, M.A. Physically crosslinked poly(vinyl alcohol)-hydroxyethyl starch blend hydrogel membranes: Synthesis and characterization for biomedical applications. *Arab. J. Chem.* **2014**, *7*, 372–380, doi:10.1016/j.arabjc.2013.05.026.

59. Nurkeeva, Z.S.; Mun, G.A.; Dubolazov, A. V.; Khutoryanskiy, V. V. pH effects on the complexation, miscibility and radiation-induced crosslinking in poly(acrylic acid)-poly(vinyl alcohol) blends. *Macromol. Biosci.* **2005**, *5*, 424–432, doi:10.1002/mabi.200400200.

60. Wu, L.; Zang, J.; Lee, L.A.; Niu, Z.; Horvatha, G.C.; Braxtona, V.; Wibowo, A.C.; Bruckman, M.A.; Ghoshroy, S.; zur Loye, H.-C.; et al. Electrospinning fabrication, structural and mechanical characterization of rod-like virus-based composite nanofibers. *J. Mater. Chem.* **2011**, *21*, 8550, doi:10.1039/c1jm00078k.

61. Sonker, A.K.; Rathore, K.; Nagarale, R.K.; Verma, V. Crosslinking of Polyvinyl Alcohol (PVA) and Effect of Crosslinker Shape (Aliphatic and Aromatic) Thereof. *J. Polym. Environ.* **2018**, *26*, 1782–1794, doi:10.1007/s10924-017-1077-3.

62. Gauthier, M.A.; Luo, J.; Calvet, D.; Ni, C.; Zhu, X.X.; Garon, M.; Buschmann, M.D. Degree of crosslinking and mechanical properties of crosslinked poly(vinyl alcohol) beads for use in solid-phase organic synthesis. *Polymer (Guildf).* **2004**, *45*, 8201–8210, doi:10.1016/j.polymer.2004.09.055.

63. Kim, K.J.; Lee, S.B.; Han, N.W. Kinetics of crosslinking reaction of PVA membrane with glutaraldehyde. *Korean J. Chem. Eng.* **1994**, *11*, 41–47, doi:10.1007/BF02697513.

64. Chiang, C.-Y.C.Y.; Mello, C.M.; Gu, J.; Silva, E.C.C.M.; Van Vliet, K.J.; Belcher, A.M. Weaving Genetically Engineered Functionality into Mechanically Robust Virus Fibers. *Adv. Mater.* **2007**, *19*, 826–832, doi:10.1002/adma.200602262.

65. Moreno-Cortez, I.E.I.E.I.E.; Romero-Garc??a, J.; Gonz??lez-Gonz??lez, V.; Garc??a-Gutierrez, D.I.; Garza-Navarro, M.A.; Cruz-Silva, R. Encapsulation and immobilization of papain in electrospun nanofibrous membranes of PVA cross-linked with glutaraldehyde vapor. *Mater. Sci. Eng. C. Mater. Biol. Appl.* **2015**, *52*, 306–314, doi:10.1016/j.msec.2015.03.049.

66. Yang, L.; Yang, Q.; Lu, D.N. Effect of chemical crosslinking degree on mechanical properties of bacterial cellulose/poly(vinyl alcohol) composite membranes. *Monatshefte fur Chemie* **2014**, *145*, 91–95, doi:10.1007/s00706-013-0968-9.

67. Jung, S.M.; Qi, J.; Oh, D.; Belcher, A.; Kong, J. M13 Virus Aerogels as a Scaffold for Functional Inorganic Materials. *Adv. Funct. Mater.* **2017**, *27*, doi:10.1002/adfm.201603203.

68. Wu, L.; Yuan, X.; Sheng, J. Immobilization of cellulase in nanofibrous PVA membranes by electrospinning. *J. Memb. Sci.* **2005**, *250*, 167–173, doi:10.1016/j.memsci.2004.10.024.

69. Destaye, A.G.; Lin, C.K.; Lee, C.K. Glutaraldehyde vapor cross-linked nanofibrous PVA mat with in situ formed silver nanoparticles. *ACS Appl. Mater. Interfaces* **2013**, *5*, 4745–4752, doi:10.1021/am401730x.

70. Migneault, I.; Dartiguenave, C.; Bertrand, M.J.; Waldron, K.C. Glutaraldehyde: Behavior in aqueous solution, reaction with proteins, and application to enzyme crosslinking. *Biotechniques* **2004**, *37*, 790–802, doi:10.2144/3705A0790.

71. Figueiredo, K.C.S.; Alves, T.L.M.; Borges, C.P. Poly(vinyl alcohol) Films Crosslinked by Glutaraldehyde Under Mild Conditions. *J. Appl. Polym. Sci.* **2009**, *111*, 3074–3080, doi:10.1002/app.29263.

72. Basiuk, E. V.; Anis, A.; Bandyopadhyay, S.; Alvarez-Zauco, E.; Chan, S.L.I.; Basiuk, V.A. Poly(vinyl alcohol)/CNT composites: An effect of cross-linking with glutaraldehyde. *Superlattices Microstruct.* **2009**, *46*, 379–383, doi:10.1016/j.spmi.2008.10.007.

73. Shaikh, R.P.; Kumar, P.; Choonara, Y.E.; du Toit, L.C.; Pillay, V. Crosslinked electrospun PVA nanofibrous membranes: elucidation of their physicochemical, physicomechanical and molecular disposition. *Biofabrication* **2012**, *4*, 025002, doi:10.1088/1758-5082/4/2/025002.

74. Cheeney, J.E.; Hsieh, S.T.; Myung, N. V.; Haberer, E.D. Whispering gallery mode emission from dye-doped polymer fiber cross-sections fabricated by near-field electrospinning. *Nanoscale* **2020**, *12*, 9873–9883, doi:10.1039/d0nr00147c.

75. Scott, T.A. Refractive index of ethanol-water mixtures and density and refractive index of ethanol-water-ethyl ether mixtures. *J. Phys. Chem.* **1946**, *50*, 406–412, doi:10.1021/j150449a003.

76. Charlebois, M.; Paquet, A.; Verret, L.S.; Boissinot, K.; Boissinot, M.; Bergeron, M.G.; Allen, C.N. Toward Automatic Label-Free Whispering Gallery Modes Biodetection with a Quantum Dot-Coated Microsphere Population. *Nanoscale Res. Lett.* **2010**, *5*, 524–532, doi:10.1007/s11671-010-9541-1.

77. Ta, V.D.; Chen, R.; Sun, H. Coupled polymer microfiber lasers for single mode operation and enhanced refractive index sensing. *Adv. Opt. Mater.* **2014**, *2*, 220–225, doi:10.1002/adom.201300433.

78. Ta, V.D.; Chen, R.; Ma, L.; Jun Ying, Y.; Sun, H.D. Whispering gallery mode microlasers and refractive index sensing based on single polymer fiber. *Laser Photonics Rev.* **2013**, *7*, 133–139, doi:10.1002/lpor.201200074.

79. Vollmer, F.; Arnold, S. Whispering-gallery-mode biosensing: Label-free detection down to single molecules. *Nat. Methods* **2008**, *5*, 591–596, doi:10.1038/nmeth.1221.

80. Anand, V.R.; Mathew, S.; Linslal, C.L.; Radhakrishnan, P.; Kailasnath, M. Microring embedded hollow polymer optical fiber for refractive index sensing. *J. Lumin.* **2019**, *209*, 69–73, doi:10.1016/j.jlumin.2019.01.001.

81. Foreman, M.R.; Vollmer, F. Optical tracking of anomalous diffusion kinetics in polymer microspheres. *Phys. Rev. Lett.* **2015**, *114*, 118001, doi:10.1103/PhysRevLett.114.118001.

82. Zhang, J.; Zhong, J.; Fang, Y.F.; Wang, J.; Huang, G.S.; Cui, X.G.; Mei, Y.F. Roll up polymer/oxide/polymer nanomembranes as a hybrid optical microcavity for humidity sensing. *Nanoscale* **2014**, *6*, 13646–13650, doi:10.1039/c4nr03473b.

83. Scholten, K.; Fan, X.; Zellers, E.T. A microfabricated optofluidic ring resonator for sensitive, high-speed detection of volatile organic compounds. *Lab Chip* **2014**, *14*, 3873–3880, doi:10.1039/c4lc00739e.

84. Kudo, S.; Otsuka, E.; Suzuki, A. Swelling behavior of chemically crosslinked PVA gels in mixed solvents. *J. Polym. Sci. Part B Polym. Phys.* **2010**, *48*, 1978–1986, doi:10.1002/polb.22076.

85. Kamemaru, K.; Usui, S.; Hirashima, Y.; Suzuki, A. Irreversible Swelling Behavior and Reversible Hysteresis in Chemically Crosslinked Poly(vinyl alcohol) Gels. *Gels* **2018**, *4*, 45, doi:10.3390/gels4020045.

86. Kim, K.J.; Lee, S.B.; Han, N.W. Effects of the degree of crosslinking on properties of poly(vinyl alcohol) membranes. *Polym. J.* **1993**, *25*, 1295–1302, doi:10.1295/polymj.25.1295.

87. Huckabay, H.A.; Wildgen, S.M.; Dunn, R.C. Label-free detection of ovarian cancer biomarkers using whispering gallery mode imaging. *Biosens. Bioelectron.* **2013**, *45*, 223–229, doi:10.1016/j.bios.2013.01.072.

88. Ghali, H.; Chibli, H.; Nadeau, J.L.; Bianucci, P.; Peter, Y.A. Real-time detection of Staphylococcus aureus using Whispering Gallery Mode optical microdisks. *Biosensors* **2016**, *6*, 1–9, doi:10.3390/bios6020020.

89. Duan, R.; Hao, X.; Li, Y.; Li, H. Detection of acetylcholinesterase and its inhibitors by liquid crystal biosensor based on whispering gallery mode. *Sensors Actuators, B Chem.* **2020**, *308*, 127672, doi:10.1016/j.snb.2020.127672.

90. Berneschi, S.; Bettazzi, F.; Giannetti, A.; Baldini, F.; Nunzi, G.; Pelli, S.; Palchetti, I. Trends in Analytical Chemistry Optical whispering gallery mode resonators for label-free detection of water contaminants. *Trends Anal. Chem.* **2020**, *126*, 115856, doi:10.1016/j.trac.2020.115856.

91. Pöllinger, M.; O'Shea, D.; Warken, F.; Rauschenbeutel, A. Ultrahigh-Q tunable whispering-gallery-mode microresonator. *Phys. Rev. Lett.* **2009**, *103*, 1–4, doi:10.1103/PhysRevLett.103.053901.

92. Navarro-Urrios, D.; Baselga, M.; Lupi, F.F.; Martín, L.L.; Pérez-Rodríguez, C.; Lavin, V.; Martín, I.R.; Garrido, B.; Capuj, N.E. Local characterization of rare-earth-doped single microspheres by combined microtransmission and microphotoluminescence techniques. *J. Opt. Soc. Am. B* **2012**, *29*, 3293–3298, doi:10.1364/josab.29.003293.

93. Imamura, S.; Watahiki, R.; Miura, R.; Shimada, T.; Kato, Y.K. Optical control of individual carbon nanotube light emitters by spectral double resonance in silicon microdisk resonators. *Appl. Phys. Lett.* **2013**, *102*, 161102, doi:10.1063/1.4802930.

94. Jones, B.D.; Oxborrow, M.; Astratov, V.N.; Hopkinson, M.; Tahraoui, A.; Skolnick, M.S.; Fox, A.M. Splitting and lasing of whispering gallery modes in quantum dot micropillars. *Opt. InfoBase Conf. Pap.* **2011**, *18*, 3302–3307, doi:10.1364/oe.18.022578.

95. McCall, S.L.; Levi, A.F.J.; Slusher, R.E.; Pearton, S.J.; Logan, R.A. Whispering-gallery mode microdisk lasers. *Appl. Phys. Lett.* **1992**, *60*, 289–291, doi:10.1063/1.106688.

96. Kipp, T.; Welsch, H.; Strelow, C.; Heyn, C.; Heitmann, D. Optical modes in

semiconductor microtube ring resonators. *Phys. Rev. Lett.* **2006**, *96*, 077403, doi:10.1103/PhysRevLett.96.077403.

97. Srinivasan, K.; Stintz, A.; Krishna, S.; Painter, O. Photoluminescence measurements of quantum-dot-containing semiconductor microdisk resonators using optical fiber taper waveguides. *Phys. Rev. B - Condens. Matter Mater. Phys.* **2005**, *72*, 205318, doi:10.1103/PhysRevB.72.205318.

98. Grossmann, T.; Schleede, S.; Hauser, M.; Christiansen, M.B.; Vannahme, C.; Eschenbaum, C.; Klinkhammer, S.; Beck, T.; Fuchs, J.; Nienhaus, G.U.; et al. Low-threshold conical microcavity dye lasers. *Appl. Phys. Lett.* **2010**, *97*, 1–4, doi:10.1063/1.3479532.

99. Armani, A.M.; Srinivasan, A.; Vahala, K.J. Soft lithographic fabrication of high Q polymer microcavity arrays. *Nano Lett.* **2007**, *7*, 1823–1826, doi:10.1021/nl0708359.

100. François, A.; Riesen, N.; Ji, H.; Afshar V., S.; Monro, T.M. Polymer based whispering gallery mode laser for biosensing applications. *Appl. Phys. Lett.* **2015**, *106*, 031104, doi:10.1063/1.4905931.

101. Brice, I.; Grundsteins, K.; Atvars, A.; Alnis, J.; Viter, R.; Ramanavicius, A. Whispering gallery mode resonator and glucose oxidase based glucose biosensor. *Sensors Actuators, B Chem.* **2020**, *318*, 128004, doi:10.1016/j.snb.2020.128004.

102. Nunzi Conti, G.; Berneschi, S.; Soria, S. Aptasensors Based on Whispering Gallery Mode Resonators. *Biosensors* **2016**, *6*, doi:10.3390/bios6030028.

103. Guo, Z.; Qin, Y.; Chen, P.; Hu, J.; Zhou, Y.; Zhao, X.; Liu, Z.; Fei, Y.; Jiang, X.; Wu, X. Hyperboloid-Drum Microdisk Laser Biosensors for Ultrasensitive Detection of Human IgG. *Small* **2020**, *16*, 1–9, doi:10.1002/smll.202000239.

104. Kim, Y.; Lee, H. On-chip label-free biosensing based on active whispering gallery mode resonators pumped by a light-emitting diode. *Opt. Express* **2019**, *27*, 34405, doi:10.1364/oe.27.034405.

105. Zhang, Y.; Zhou, T.; Han, B.; Zhang, A.; Zhao, Y. Optical bio-chemical sensors based on whispering gallery mode resonators. *Nanoscale* **2018**, *10*, 13832–13856, doi:10.1039/c8nr03709d.

106. Hunt, H.K.; Soteropulos, C.; Armani, A.M. Bioconjugation strategies for microtoroidal optical resonators. *Sensors (Switzerland)* **2010**, *10*, 9317–9336, doi:10.3390/s101009317.

107. Luchansky, M.S.; Bailey, R.C. High-Q optical sensors for chemical and biological

analysis. *Anal. Chem.* **2012**, *84*, 793–821, doi:10.1021/ac2029024.

108. Soteropulos, C.E.; Zurick, K.M.; Bernards, M.T.; Hunt, H.K. Tailoring the protein adsorption properties of whispering gallery mode optical biosensors. *Langmuir* **2012**, *28*, 15743–15750, doi:10.1021/la302041d.

109. Arnfinnsdottir, N.B.; Chapman, C.A.; Bailey, R.C.; Aksnes, A.; Stokke, B.T. Impact of silanization parameters and antibody immobilization strategy on binding capacity of photonic ring resonators. *Sensors (Switzerland)* **2020**, *20*, doi:10.3390/s20113163.

110. Ren, G.; Xu, X.; Liu, Q.; Cheng, J.; Yuan, X.; Wu, L.; Wan, Y. Electrospun poly(vinyl alcohol)/glucose oxidase biocomposite membranes for biosensor applications. *React. Funct. Polym.* **2006**, *66*, 1559–1564, doi:10.1016/j.reactfunctpolym.2006.05.005.

111. Huang, Y.; Chiang, C.Y.; Lee, S.K.; Gao, Y.; Hu, E.L.; De Yoreo, J.; Belcher, A.M. Programmable assembly of nanoarchitectures using genetically engineered viruses. *Nano Lett.* **2005**, *5*, 1429–1434, doi:10.1021/nl050795d.

112. Zaman, M.S.; Moon, C.H.; Bozhilov, K.N.; Haberer, E.D. Phage-directed synthesis of copper sulfide: Structural and optical characterization. *Nanotechnology* **2013**, *24*, doi:10.1088/0957-4484/24/32/325602.

113. Lee, S.W.; Belcher, A.M. Virus-based fabrication of micro- and nanofibers using electrospinning. *Nano Lett.* **2004**, *4*, 387–390, doi:10.1021/nl034911t.

114. Sugimoto, R.; Lee, J.H.; Lee, J.H.; Jin, H.E.; Yoo, S.Y.; Lee, S.W. Bacteriophage nanofiber fabrication using near field electrospinning. *RSC Adv.* **2019**, *9*, 39111–39118, doi:10.1039/c9ra07510k.

115. Li, T.; Zan, X.; Sun, Y.; Zuo, X.; Li, X.; Senesi, A.; Winans, R.E.; Wang, Q.; Lee, B. Self-assembly of rodlike virus to superlattices. *Langmuir* **2013**, *29*, 12777–12784, doi:10.1021/la402933q.

116. Salalha, W.; Kuhn, J.; Dror, Y.; Zussman, E. Encapsulation of bacteria and viruses in electrospun nanofibres. *Nanotechnology* **2006**, *17*, 4675–4681, doi:10.1088/0957-4484/17/18/025.

117. Sullivan, S.T.; Tang, C.; Kennedy, A.; Talwar, S.; Khan, S.A. Electrospinning and heat treatment of whey protein nanofibers. *Food Hydrocoll.* **2014**, *35*, 36–50, doi:10.1016/j.foodhyd.2013.07.023.

118. Chen, G.; Fang, D.; Wang, K.; Nie, J.; Ma, G. Core-shell structure PEO/CS nanofibers based on electric field induced phase separation via electrospinning and

its application. *J. Polym. Sci. Part A Polym. Chem.* **2015**, *53*, 2298–2311, doi:10.1002/pola.27702.

119. Tang, C.; Ozcam, A.E.; Stout, B.; Khan, S.A. Effect of pH on protein distribution in electrospun PVA/BSA composite nanofibers. *Biomacromolecules* **2012**, *13*, 1269–1278, doi:10.1021/bm2017146.

120. Niu, B.; Shi, X.; Ge, K.; Ruan, J.; Xu, Z.; Zhang, S.; Guo, D.; Zhai, T. An all-optical tunable polymer WGM laser pumped by a laser diode. *Nanoscale Adv.* **2022**, 2153–2158, doi:10.1039/d2na00025c.

121. Wondimu, S.F.; Hippler, M.; Hussal, C.; Hofmann, A.; Krämmer, S.; Lahann, J.; Kalt, H.; Freude, W.; Koos, C. Robust label-free biosensing using microdisk laser arrays with on-chip references. *Opt. Express* **2018**, *26*, 3161, doi:10.1364/oe.26.003161.

122. Ouyang, X.; Liu, T.; Zhang, Y.; He, J.; He, Z.; Zhang, A.P.; Tam, H.Y. Ultrasensitive optofluidic enzyme-linked immunosorbent assay by on-chip integrated polymer whispering-gallery-mode microlaser sensors. *Lab Chip* **2020**, *20*, 2438–2446, doi:10.1039/d0lc00240b.

123. Zamora, V.; Díez, A.; Andrés, M. V.; Gimeno, B. Cylindrical optical microcavities: Basic properties and sensor applications. *Photonics Nanostructures - Fundam. Appl.* **2011**, *9*, 149–158, doi:10.1016/j.photonics.2010.09.007.

124. Sumetsky, M. Localization of light on a cone: theoretical evidence and experimental demonstration for an optical fiber. *Opt. Lett.* **2011**, *36*, 145–147, doi:10.1364/ol.36.000145.

125. Sumetsky, M. Optical bottle microresonators. *Prog. Quantum Electron.* **2019**, *64*, 1–30, doi:10.1016/j.pquantelec.2019.04.001.

126. Luan, F.; Magi, E.; Gong, T.; Kabakova, I.; Eggleton, B.J. Photoinduced whispering gallery mode microcavity resonator in a chalcogenide microfiber. *Opt. Lett.* **2011**, *36*, 4761–4763, doi:10.1364/ol.36.004761.

127. Silverstone, J.W.; McFarlane, S.; Manchee, C.P.K.; Meldrum, A. Ultimate resolution for refractometric sensing with whispering gallery mode microcavities. *Opt. Express* **2012**, *20*, 8284, doi:10.1364/oe.20.008284.

128. Khozeymeh, F.; Razaghi, M. Sensitivity optimization in whispering gallery mode optical cylindrical biosensors. In Proceedings of the Journal of Physics: Conference Series; 2018; Vol. 956, pp. 0–6.

129. Shen, W.; Li, S.; Park, M.-K.; Zhang, Z.; Cheng, Z.; Petrenko, V.A.; Chin, B.A.

Blocking Agent Optimization for Nonspecific Binding on Phage Based Magnetoelastic Biosensors. *J. Electrochem. Soc.* **2012**, *159*, B818–B823, doi:10.1149/2.057210jes.

130. François, A.; Reynolds, T.; Monro, T.M. A fiber-tip label-free biological sensing platform: A practical approach toward in-vivo sensing. *Sensors (Switzerland)* **2015**, *15*, 1168–1181, doi:10.3390/s150101168.

131. Landry, J.P.; Sun, Y.S.; Guo, X.W.; Zhu, X.D. Protein reactions with surface-bound molecular targets detected by oblique-incidence reflectivity difference microscopes. *Appl. Opt.* **2008**, *47*, 3275–3288, doi:10.1364/AO.47.003275.

132. Halicka, K.; Cabaj, J. Electrospun nanofibers for sensing and biosensing applications—a review. *Int. J. Mol. Sci.* **2021**, *22*, 1–24, doi:10.3390/ijms22126357.

133. Brown, T.D.; Slotosch, A.; Thibaudeau, L.; Taubenberger, A.; Loessner, D.; Vaquette, C.; Dalton, P.D.; Hutmacher, D.W. Design and fabrication of tubular scaffolds via direct writing in a melt electrospinning mode. *Biointerphases* **2012**, *7*, 1–16, doi:10.1007/s13758-011-0013-7.

134. Montalbano, G.; Tomasina, C.; Fiorilli, S.; Camarero-Espinosa, S.; Vitale-Brovarone, C.; Moroni, L. Biomimetic scaffolds obtained by electrospinning of collagen-based materials: Strategies to hinder the protein denaturation. *Materials (Basel).* **2021**, *14*, doi:10.3390/ma14164360.

135. Alhosseini, S.N.; Moztarzadeh, F.; Mozafari, M.; Asgari, S.; Dodel, M.; Samadikuchaksaraei, A.; Kargozar, S.; Jalali, N. Synthesis and characterization of electrospun polyvinyl alcohol nanofibrous scaffolds modified by blending with chitosan for neural tissue engineering. *Int. J. Nanomedicine* **2012**, *7*, 25–34, doi:10.2147/IJN.S25376.

136. Wongkanya, R.; Chuysinuan, P.; Pengsuk, C.; Techasakul, S.; Lirdprapamongkol, K.; Svasti, J.; Nooeaid, P. Electrospinning of alginate/soy protein isolated nanofibers and their release characteristics for biomedical applications. *J. Sci. Adv. Mater. Devices* **2017**, *2*, 309–316, doi:10.1016/j.jsamd.2017.05.010.

137. Chew, S.Y.; Wen, J.; Yim, E.K.F.; Leong, K.W. Sustained release of proteins from electrospun biodegradable fibers. *Biomacromolecules* **2005**, *6*, 2017–2024, doi:10.1021/bm0501149.

138. Moreira, A.; Lawson, D.; Onyekuru, L.; Dziemidowicz, K.; Angkawinitwong, U.; Costa, P.F.; Radacsi, N.; Williams, G.R. Protein encapsulation by electrospinning and electrospraying. *J. Control. Release* **2021**, *329*, 1172–1197, doi:10.1016/j.jconrel.2020.10.046.

139. He, C.; Nie, W.; Feng, W. Engineering of biomimetic nanofibrous matrices for drug delivery and tissue engineering. *J. Mater. Chem. B* **2014**, *2*, 7828–7848, doi:10.1039/c4tb01464b.

140. Zhao, C.; Bai, J.; Gong, H.; Liu, S.; Wang, F. Tailorable Morphology of Core–Shell Nanofibers with Surface Wrinkles for Enhanced Gas-Sensing Properties. *ACS Appl. Nano Mater.* **2018**, *1*, 6357–6367, doi:10.1021/acsanm.8b01573.

141. Guo, M.; Wang, X.; Liu, Y.; Yu, H.; Dong, J.; Cui, Z.; Bai, Z.; Li, K.; Li, Q. Hierarchical Shish-Kebab Structures Functionalizing Nanofibers for Controlled Drug Release and Improved Antithrombogenicity. *Biomacromolecules* **2022**, *23*, 1337–1349, doi:10.1021/acs.biomac.1c01572.

142. Wang, X.; Yuan, Y.; Huang, X.; Yue, T. Controlled release of protein from core-shell nanofibers prepared by emulsion electrospinning based on green chemical. *J. Appl. Polym. Sci.* **2015**, *132*, 1–9, doi:10.1002/app.41811.

143. Frizzell, H.; Ohlsen, T.J.; Woodrow, K.A. Protein-loaded emulsion electrospun fibers optimized for bioactivity retention and pH-controlled release for peroral delivery of biologic therapeutics. *Int. J. Pharm.* **2017**, *533*, 99–110, doi:10.1016/j.ijpharm.2017.09.043.

144. Chen, L.; Liu, X.; Zheng, X.; Zhang, X.; Yang, J.; Tian, T.; Liao, Y. Dielectrophoretic separation of particles using microfluidic chip with composite three-dimensional electrode. *Micromachines* **2020**, *11*, doi:10.3390/mi11070700.

145. Kim, H.J.; Kim, J.; Yoo, Y.K.; Lee, J.H.; Park, J.H.; Hwang, K.S. Sensitivity improvement of an electrical sensor achieved by control of biomolecules based on the negative dielectrophoretic force. *Biosens. Bioelectron.* **2016**, *85*, 977–985, doi:10.1016/j.bios.2016.06.081.

146. Li, Z.; Kang, H.; Che, N.; Liu, Z.; Li, P.; Li, W.; Zhang, C.; Cao, C.; Liu, R.; Huang, Y. Effects of Electrode Reversal on the Distribution of Naproxen in the Electrospun Cellulose Acetate Nanofibers. *J. Nanomater.* **2014**, *2014*, 1–8, doi:10.1155/2014/360658.

147. Mu, X.; Liu, Y.; Fang, D.; Wang, Z.; Nie, J.; Ma, G. Electric field induced phase separation on electrospinning polyelectrolyte based core – shell nanofibers. *Carbohydr. Polym.* **2012**, *90*, 1582–1586, doi:10.1016/j.carbpol.2012.07.034.

148. Ura, D.P.; Rosell-Llompart, J.; Zaszczyńska, A.; Vasilyev, G.; Gradys, A.; Szewczyk, P.K.; Knapczyk-Korczak, J.; Avrahami, R.; Šišková, A.O.; Arinstein, A.; et al. The role of electrical polarity in electrospinning and on the mechanical and structural properties of as-spun fibers. *Materials (Basel).* **2020**, *13*, doi:10.3390/ma13184169.

149. Stachewicz, U.; Stone, C.A.; Willis, C.R.; Barber, A.H. Charge assisted tailoring of chemical functionality at electrospun nanofiber surfaces. *J. Mater. Chem.* **2012**, *22*, 22935–22941, doi:10.1039/c2jm33807f.

150. Su, R.; Zhong, G.; Fu, Q.; Zhang, L.; Fong, H.; Zhu, L. Polarity-induced ferroelectric crystalline phase in electrospun fibers of poly(vinylidene fluoride)/polyacrylonitrile blends. *J. Mater. Res.* **2012**, *27*, 1389–1398, doi:10.1557/jmr.2012.56.

151. Passaretti, P.; Sun, Y.; Dafforn, T.R.; Oppenheimer, P.G. Determination and characterisation of the surface charge properties of the bacteriophage M13 to assist bio-nanoengineering. *RSC Adv.* **2020**, *10*, 25385–25392, doi:10.1039/d0ra04086j.

152. Son, W.K.; Ho Youk, J.; Seung Lee, T.; Park, W.H. Effect of pH on electrospinning of poly(vinyl alcohol). *Mater. Lett.* **2005**, *59*, 1571–1575, doi:10.1016/j.matlet.2005.01.025.

153. Hsieh, S.T.; Cheeney, J.E.; Ding, X.; Myung, N. V; Haberer, E.D. Near-field electrospinning of polymer/phage whispering gallery mode microfiber resonators for label-free biosensing. *Sensors Actuators B Chem.* **2022**, *367*, 132062, doi:10.1016/j.snb.2022.132062.

154. Li, T.; Zan, X.; Winans, R.E.; Wang, Q.; Lee, B. Biomolecular assembly of thermoresponsive superlattices of the tobacco mosaic virus with large tunable interparticle distances. *Angew. Chemie - Int. Ed.* **2013**, *52*, 6638–6642, doi:10.1002/anie.201209299.

155. Beygi Khosrowshahi, Y.; Salem, A. Influence of Polyvinyl Alcohol and Carboxymethyl Cellulose on the Reliability of Extruded Ceramic Body: Application of Mixture Design Method in Fabricating Reliable Ceramic Raschig Rings. *Int. J. Appl. Ceram. Technol.* **2011**, *8*, 1334–1343, doi:10.1111/j.1744-7402.2010.02544.x.

156. Kilic, A.; Oruc, F.; Demir, A. Effects of Polarity on Electrospinning Process. *Text. Res. J.* **2008**, *78*, 532–539, doi:10.1177/0040517507081296.

157. ALİ, U.; ABBAS, A.; ASLAM, S.; NİU, H.; QADİR, M.B.; LİN, T.; ALEEM, A.U. Influence of Spinneret Polarity in Needleless Electrospinning. *TEKSTİL VE KONFEKSİYON* **2021**, *31*, 10–18, doi:10.32710/tekstilvekonfeksiyon.655302.

158. Bang, H.; Gopiraman, M.; Kim, B.S.; Kim, S.H.; Kim, I.S. Effects of pH on electrospun PVA/acid-treated MWNT composite nanofibers. *Colloids Surfaces A Physicochem. Eng. Asp.* **2012**, *409*, 112–117, doi:10.1016/j.colsurfa.2012.05.046.

159. Xing, X.; Li, Z.; Ngai, T. PH-controllable depletion attraction induced by microgel

particles. *Macromolecules* **2009**, *42*, 7271–7274, doi:10.1021/ma901130x.

160. Yadav, I.; Aswal, V.K.; Kohlbrecher, J. PH-Dependent depletion induced phase behavior of silica nanoparticles. *AIP Conf. Proc.* **2017**, *1832*, 3–5, doi:10.1063/1.4980217.

161. Tyson, B.M.; Abu Al-Rub, R.K.; Yazdanbakhsh, A.; Grasley, Z. A quantitative method for analyzing the dispersion and agglomeration of nano-particles in composite materials. *Compos. Part B Eng.* **2011**, *42*, 1395–1403, doi:10.1016/j.compositesb.2011.05.020.

162. Urbanek, O.; Sajkiewicz, P.; Pierini, F. The effect of polarity in the electrospinning process on PCL/chitosan nanofibres' structure, properties and efficiency of surface modification. *Polymer (Guildf).* **2017**, *124*, 168–175, doi:10.1016/j.polymer.2017.07.064.

163. You, X.; Ye, C.; Guo, P. Electric field manipulation for deposition control in near-field electrospinning. *J. Manuf. Process.* **2017**, *30*, 431–438, doi:10.1016/j.jmapro.2017.10.005.

164. Sun, X. Concurrent and Sequential Surface Modification of Electrospun Polymer Micro/Nano-Fibers, North Carolina State University, 2008.

165. Zamora, V.; Díez, A.; Andrés, M. V.; Gimeno, B. Interrogation of whispering-gallery modes resonances in cylindrical microcavities by backreflection detection. *Opt. Lett.* **2009**, *34*, 1039, doi:10.1364/ol.34.001039.

166. Sumetsky, M. Mode localization and the Q-factor of a cylindrical microresonator. *Opt. Lett.* **2010**, *35*, 2385, doi:10.1364/ol.35.002385.

167. Supraja, P.; Tripathy, S.; Krishna Vanjari, S.R.; Singh, V.; Singh, S.G. Label free, electrochemical detection of atrazine using electrospun Mn2O3 nanofibers: Towards ultrasensitive small molecule detection. *Sensors Actuators, B Chem.* **2019**, *285*, 317–325, doi:10.1016/j.snb.2019.01.060.

168. Jiang, X.; Qavi, A.J.; Huang, S.H.; Yang, L. Whispering-Gallery Sensors. *Matter* **2020**, *3*, 371–392, doi:10.1016/j.matt.2020.07.008.

169. Balac, S. WGMode: A Matlab toolbox for whispering gallery modes volume computation in spherical optical micro-resonators. *Comput. Phys. Commun.* **2019**, *243*, 121–134, doi:10.1016/j.cpc.2019.05.002.

170. Zeng, H.; Katagiri, D.; Ogino, T.; Nakajima, H.; Kato, S.; Uchiyama, K. Droplet Enhanced Fluorescence for Ultrasensitive Detection Using Inkjet. *Anal. Chem.* **2016**, *88*, 6135–6139, doi:10.1021/acs.analchem.6b01566.

171. Mallik, A.K.; Farrell, G.; Wu, Q.; Semenova, Y. Study of the influence of the agarose hydrogel layer thickness on sensitivity of the coated silica microsphere resonator to humidity. *Appl. Opt.* **2017**, *56*, 4065, doi:10.1364/AO.56.004065.

172. Eryürek, M.; Tasdemir, Z.; Karadag, Y.; Anand, S.; Kilinc, N.; Alaca, B.E.; Kiraz, A. Integrated humidity sensor based on SU-8 polymer microdisk microresonator. *Sensors Actuators, B Chem.* **2017**, *242*, 1115–1120, doi:10.1016/j.snb.2016.09.136.

173. Burczak, K.; Fujisato, T.; Hatada, M.; Ikada, Y. Protein permeation through poly(vinyl alcohol) hydrogel membranes. *Biomaterials* **1994**, *15*, 231–238, doi:10.1016/0142-9612(94)90072-8.

174. Senanayake, K.K.; Fakhrabadi, E.A.; Liberatore, M.W.; Mukhopadhyay, A. Diffusion of Nanoparticles in Entangled Poly(vinyl alcohol) Solutions and Gels. *Macromolecules* **2019**, *52*, 787–795, doi:10.1021/acs.macromol.8b01917.

175. Dai, W.S.; Barbari, T.A. Hydrogel membranes with mesh size asymmetry based on the gradient crosslinking of poly(vinyl alcohol). *J. Memb. Sci.* **1999**, *156*, 67–79, doi:10.1016/S0376-7388(98)00330-5.